ABSTRACT

Title of Dissertation: GLOBAL BARE GROUND GAIN BETWEEN 2000 AND 2012 AND THE RELATIONSHIP WITH SOCIOECONOMIC DEVELOPMENT

Qing Ying, Doctor of Philosophy, 2020

Dissertation directed by: Professor Matthew C. Hansen

Department of Geographical Sciences

Bare ground gain -- the complete removal of vegetation due to land use changes, represents an extreme land cover transition that completely alters the structure and functioning of ecosystems. The fast expansion of bare ground cover is directly associated with increasing population and urbanization, resulting in accelerated greenhouse gas emissions, intensified urban heat island phenomenon, and extensive habitat fragments and loss. While the economic return of settlement and infrastructure construction has improved human livelihoods, the negative impacts on the environment have disproportionally affected vulnerable population, creating inequality and tension in society. The area, distribution, drivers, and change rates of

global bare ground gain were not systematically quantified; neither was the relationship between such dynamics and socioeconomic development. This dissertation seeks methods for operational characterization of bare ground expansion, advances our understanding of the magnitudes, dynamics, and drivers of global bare ground gain between 2000 and 2012, and uncovers the implications of such change for macro-economic development monitoring, all through Landsat satellite observations. The approach that employs wall-to-wall maps of bare ground gain classified from Landsat imagery for probability sample selection is proved particularly effective for unbiased area estimation of global, continental, and national bare ground gain, as a small land cover and land use change theme. Anthropogenic land uses accounted for 95% of the global bare ground gain, largely consisting of commercial/residential built-up, infrastructure development, and resource extraction. China and the United States topped the total area increase in bare ground. Annual change rates of anthropogenic bare ground gain are found as a leading indicator of macro-economic change in the study period dominated by the 2007-2008 global financial crisis, through econometric analysis between annual gains in the bare ground of different land use outcomes and economic fluctuations in business cycles measured by detrended economic variables. Instead of intensive manual interpretation of land-use attributes of probability sample, an approach of integrating a pixel- and an object- based deep learning algorithms is proposed and tested feasible for automatic attribution of airports, a transportation land use with economic importance.

GLOBAL BARE GROUND GAIN BETWEEN 2000 AND 2012 AND THE RELATIONSHIP WITH SOCIOECONOMIC DEVELOPMENT

by

Qing Ying

Dissertation submitted to the Faculty of the Graduate School of the
University of Maryland, College Park, in partial fulfillment
of the requirements for the degree of
Doctor of Philosophy
2020

Advisory Committee:

Professor Matthew C. Hansen, Chair

Research Associate Professor Peter V. Potapov

Professor Laixiang Sun

Professor Scott Goetz

Professor Joseph Sullivan

Foreword

Chapter 2-4 contain jointly authored work in which Qing Ying is the primary author. Qing Ying leads conceptualization, methods development, data processing and analysis, and manuscript writing with contributions from the other co-authors named in each corresponding chapter.

Dedication

To my mom, for unconditional love and support; my dad, I know you were there, like a star in the sky, watching me through every night; my son, for inspiring a better me.

Acknowledgements

There are many people I want to acknowledge within and outside the department. I am deeply grateful to my advisor, Matt Hansen, who not only guided my research with insights and constant support but also helped me to build confidence and critical thinking in scientific research with great patience and encouragement. Your great enthusiasm for remotely sensed images and incredible experience and knowledge on the ground have always inspired my curiosity about people and our mother nature and explorable practices. Thank you for giving me great opportunities to work, learn, and grow as a researcher and scientist in the GLAD team.

I want to express my gratitude to Peter Potapov, Steve Stehman, and Laixiang Sun for all of your help and support. My work on the dissertation and papers would not smoothly proceed without your expertise and guidance. Peter, thank you for always being available to address my questions and provide practical help throughout my study. I am also thankful to Scott Goetz for helpful comments and constructive feedbacks in every committee meeting from a different time zone, to Joe Sullivan for generously supporting me as the Dean's Representative of my committee.

I am sincerely thankful to George Hurtt, who brought me into this department and taught me the knowledge of ecosystem processes and modeling. To Shunlin Liang, Chenquan Huang, Stephen Prince, Martha Geores, Guoqing Sun for providing pertinent suggestions from different perspectives during the early stage of my study.

My special thanks go to the past and current members of the GLAD group, with whom I would not feel embarrassed to share my tears and joys in my research and my life. I am very grateful for all the spiritual, emotional, and practical support from many of you. I overcame many technical difficulties and gained proficient skills thanks to the help of Lei Wang and Andres Serna. I also want to thank my dear

friends who were or still are in the department, for the precious friendship and joyful times that gave me strength in this journey.

To my mom, Jingfei Fu, no words can express my gratitude for your endless love and selfless sacrifices. My family, the source that keeps me strong and moving forward.

Table of Contents

List of Tables

List of Figures

Chapter 1 Introduction

Bare ground cover, or the inverse of vegetative cover, accounts for 26% of global land area (excluding Antarctica) (Friedl et al., 2010; Gong et al., 2013; Song et al., 2018) and features high spectral reflectance in visible and near infrared bands, and therefore high albedo in surface energy flux. Bare ground is readily mapped using optical remote sensing data with products that include per pixel categorical and percent cover characterizations (Hansen et al., 2011; Pu et al., 2008; Small, 2005). Many terms have emerged from different remote sensing studies to describe the components of bare ground cover, for instance, impervious cover, bare soil, built-up environment and barren land. The concept of imperviousness focuses on the non-evaporating and non-transpiring property of land surface such as rooftops, roads, and parking lots, whereas bare soil allows water to infiltrate into deep or evaporate into air (Arnold Jr and Gibbons, 1996; Xian and Homer, 2010; Yang et al., 2003). From presence or absence of human intervention, built-up environment describes bare ground modified by human activities, whereas barren/bare land is a natural landform of soil, sand or rock. Barren land is most extensive and appears as deserts, dry lands, lake/river/sea shores, or glacier mountain/land (Friedl et al., 2010; Yang et al., 2018). In contrast, impervious surface or built-up environments reflect the most extreme modification of the land surface by humans, and consist principally of road surface and settlements, respectively (Liu et al., 2020; Lu and Weng, 2006; Schneider et al., 2010).

Bare ground and its change over time impacts the earth system. For example, changes in surface reflectance and evapotranspiration due to development result in anomalous heating of densely developed areas, a phenomenon called the urban heat island effect (Kalnay and Cai, 2003; Peng et al., 2012). Urban heat islands are often associated with increased mortality during heat waves (Conti et al., 2005; Founda and Santamouris, 2017) and changes in regional weather patterns (Zhao et al., 2018). Bare ground gain is also associated with energy use and greenhouse gas (GHG) emissions due to increased fossil fuel use and cement production (IPCC, 2015; O'Neill et al., 2012; Wang et al., 2016; Xie et al., 2017). For example, global urban area accounted for 71% of energy-related carbon dioxide (CO_2) emissions in 2006 and 37% - 49% of global GHG emissions in 2000 (Dhakal, 2010; Marcotullio et al., 2013). Regarding biodiversity, the removal of vegetation accelerates biodiversity loss from habitat loss and fragmentation (Ibisch et al., 2016). Indirect impacts include changes in water and nutrient availability, increased air pollution and invasive species (Kennedy et al., 2011; McDonald et al., 2018; Säumel and Kowarik, 2010; Seinfeld, 1989). Most studies of bare ground dynamics are local to national, and few document rates of change. Advancing the spatial detail and extent of such studies, trends over time, and the various drivers and attributes of bare ground change is needed and merits academic, public and political attention.

The dynamic of bare ground cover change consists of bare ground gain and loss. For the purposes of this study, bare ground gain (BGG) is defined as the persistent appearance of bare ground following complete removal of vegetation cover. This

definition includes all permanent or semi-permanent vegetation loss but excludes ephemeral loss such as agricultural harvests or fallows and forest disturbances. Such a dynamic can be attributed to abrupt or gradual environmental deterioration or direct human activities, e.g., commercial/residential built-up, infrastructure development, or vegetation clearing for land development. Attributing the land cover and land use outcomes of bare ground gain is an important step in assessing the context of such change, specifically land-use outcomes and socioeconomic drivers. Many studies have focused on human-induced components of bare ground change because of their fast growth rates, significant environmental impacts, and complex implications to human society (European Environment Agency, 2018; Angel et al., 2011; Xian and Homer, 2010).

Beyond geospatial information of bare ground dynamics, uncovering the linkage between change rates and socioeconomic development at national to regional scales may pave a quantitative road for theoretical and experimental studies on advancing human livelihood. For example, the abundance of roof materials can help predict poverty, the intensity of nighttime lights can help measure urban and rural economies (Jean et al., 2016; Mellander et al., 2015). The drivers of global land cover and land use change (LCLUC) reflect the demands of growing populations and improved living standards all occurring with a matrix of changing demographic structures, new technologies, globalization, and human-induced climate change and other environmental impacts. Quantities and trends of specific land cover and land use change may reciprocally reflect population flows and market demand, supply and

anticipation of certain commodities and services. For instance, historical population distributions and movements from rural to urban areas result in new commercial/residential built-up on fringe of cities and new infrastructure to produce and transport goods. Better living environments and upgraded transportation systems attract more people to urban areas and facilitate economic growth in return. Specific questions that merit examination include how the velocity of bare ground gain relates with economic expansion and contraction and whether remotely sensed bare ground gain can serve as an indicator of economic development. Answers to these questions can further serve to advance near-real time monitoring of macroeconomic activity.

The presented dissertation developed practical approaches to address the above questions using Landsat imagery for generic mapping of bare ground gain, the attribution of bare ground gain into relevant land use outcomes and drivers, and the relationship of global bare ground dynamics with economic activity between 2000 and 2012.

1. Background

1.1.1 Mapping large-scale bare ground gain and drivers with satellite data: status and challenges

Reliable land cover change detection and monitoring largely depends on the consistency of earth observation data through time and space. Challenges affecting data consistency for land characterization include contamination by cloud and cloud shadow, topographic shading, surface anisotropy, and atmospheric scattering and

absorption. The availability of consistently processed time-series imagery, for example Landsat analysis ready data (ARD) (Potapov et al., 2020; Wang et al., 2018), allows for large scale characterization of land cover and land use extent and change. Given this fact, the objective of this section is to review methodologies and applications of bare ground change related studies rather than the preprocessing and quality assessment of satellite data for large-scale change detection and thematic characterization.

There are generally two approaches or modifications adopted in most national to global remote sensing practices of automatic land cover change detection and monitoring. One is to directly detect changed pixels or areas between time series or paired images. For example, the global forest change has been classified from Landsat based multi-temporal metrics and updated annually (Hansen et al., 2016; M. C. Hansen et al., 2013). The second one is to compare thematic characterizations at different time for changes, namely post-characterization comparison (or post-classification comparison). The problem with the latter method is the propagation of errors in the individual map products. The accuracy of the output change map is subject to those of input maps and tends to be lower than either of the input accuracies. However, time-series of percent cover maps offer an alternative for post-characterization change methods (Hansen et al. 2004). Here the fuzzy nature of percent cover ameliorates some of the problems of comparison discrete land cover maps and times-series products can also overcome individual map errors. For the purposes of this study, we call this approach indirect change detection. Both indirect

and direct change detection approaches are combined in Chapter 2 for global wall-to-wall mapping of bare ground gain.

Selection of classification algorithms should merit fast and reliable large-scale remote sensing applications, which also defines the design of training sample collection, the dimension of input data and the strategy of computational implementation. Typical algorithms include change vector analysis and abundant machine learning algorithms (support vector machines, decision trees, and neural networks etc.). The USGS National Land Cover Database (NLCD) impervious surface product is a representative example which uses change vectors and multiple thresholds to detect impervious surface change and update impervious surface cover at five year intervals (Xian and Homer, 2010; Yang et al., 2018). However, an ancillary land cover product was required to update NLCD imperviousness and only dynamics in urban areas were updated. Algorithms that use prior distribution knowledge of thresholding, such as change vector analysis, have limited performance in highly dynamic, disturbed, or heterogeneous landscapes, and normally operate over limited areal extents, i.e. a single Landsat scene. Support vector machines (SVM) have been applied to change detection in circumstances with limited training data, but the obtained results were significantly affected by kernel selection and parameter assignment (Mountrakis et al., 2011). Tree-based algorithms (classification tree, regression tree and random forest) have been widely employed in remotely sensed change detection due to good model performance, capability to handle high dimensional data and multicollinearity, and less user-defined parameters compared to

SVM (Belgiu and Drăgu, 2016; Friedl and Brodley, 1997; Pal, 2005). National level land cover change with Web-Enabled Landsat Data (WELD) and global forest change products are examples of tree-based algorithms applied to large-scale change detection and monitoring (Hansen et al., 2014; M. C. Hansen et al., 2013). However, the stability of maps resulted from tree-based models developed through various training sample (e.g., from different subsets of a large sample data) remains a challenge (Belgiu and Drăgu, 2016; Shao and Lunetta, 2012). Neural networks were examined in a set of local experiments on change detection (Liu and Lathrop, 2002; Rogan et al., 2008). He (et al., 2019) explored the ability of fully convolutional network to map global urban area at 1km resolution. Neural networks offer promise, but have many parameter settings that require advanced knowledge for optimal implementation.

Recent developments in artificial intelligence makes deep neural networks a stand-alone category, namely deep learning. Deep convolutional neural network (CNN) has been substantially developed and demonstrated to be one of the state-of-the-art deep learning algorithms in the field of computer vision and artificial intelligence (Helber et al., 2019). One of the advantages of deep CNN is cross-scale context feature generalization through convolutional layers and pooling layers that can be automatically optimized through a backpropagation algorithm. The context features can be one dimensional for temporal context or two dimensional for spatial context. This advantage manifests a potential of deep CNN in the detection and attribution of landscape objects (i.e., airports, roads, intensive agriculture fields), which could be

more difficult to achieve via traditional per-pixel algorithms. The idea of deep learning is that the machine learning performance grows when the training data size, computational power and model complexity grow, whereas traditional machine learning algorithms may have performance limitations in these cases. Hence, one challenge for applying deep learning in land resource management is the collection of a large amount of training data. Landsat-based application of CNN to thematic land cover and change detection at large-scale requires more investigation. In Chapter 4, I will investigate how to detect an attributed bare ground theme, national scale airports, an important component of transportation system, using deep CNN.

With the progress of continuous satellite image acquisitions, analysis ready data and machine learning algorithms, there is an ongoing paradigm shift from endpoint change detection to time series analysis, which enhances the ability of earth observation from land or condition change detection to surface dynamic monitoring (Gómez et al., 2016; Woodcock et al., 2019). The frequency of updating varies from monthly, seasonally, annually or whenever a change is detected in a near-real time alert system (Hansen et al., 2016; Pekel et al., 2016). Statistical trend analysis uses simple linear model fitting and has been applied to coarse resolution imagery (i.e. AVHRR, MODIS) to quantify trends (Song et al., 2018). More sophisticated fitting models are required for precise detection on the timing and magnitude of change using Landsat imagery (Atkinson et al., 2012; Song et al., 2016). A further step to tackle random noise in single-date records and spatial variability is to design temporal statistics that are sensitive to target change and use them in machine learning

algorithms (Potapov et al., 2015). This idea will be applied to bare ground gain mapping in Chapter 2. While many present products regarding bare ground generated annual maps (of human settlements or imperviousness) and inferred the expansion via inter-annual comparison (Gong et al., 2020), future direction is to detect inter-annual changes by time series analysis.

Given human-induced bare ground only accounts for a tiny portion of global land area, many studies apply a mask generated from vegetation cover indices or night time light luminosity before mapping human settlement or impervious surface (Gong et al., 2020; Wang et al., 2017). However, this process either likely underestimates suburban area due to mixed vegetated-impervious pixels or leaves some linear transportation or isolated structure features out. A more operational approach, which will be applied in Chapter 2, is to add more training on class boundaries and build models that distinguish vegetation, water and bare ground cover and dynamics at the global scale.

Integration of multi-source geospatial data is an emerging direction in land resource monitoring. Combination of optical and radar, day and night satellite data enriches the structural information or energy consumption context for attributing human-induced bare ground. Frolking et al. (2013) combined backscatter power from SeaWinds microwave scatterometer and nighttime light to examine changes in built-up volume from 1999 to 2009 in big cities selected globally. Esch et al. (2017) employed TanDEM-X and TerraSAR-X radar images and developed the highest resolution map till present of global urban footprint. Volunteered geospatial data and

socially sensed activity data provide additional behavior information of people tagged to presenting build-up, which can be used to improve the attribution of populated bare ground area (Fu et al., 2019).

1.1.2 Map-stratified sampling: an efficient framework to estimate unbiased areas and attributions of bare ground gain

State-of-the-art wall-to-wall maps of land cover and use change reliably delineate spatially exhaustive and temporally consistent dynamics of land surface physical appearance (M. C. Hansen et al., 2013; Olofsson et al., 2014). However, errors attributed to data quality, mapping process and analyst biases are inevitable, and hence hinder the confidence of change area calculated from map-pixel counting. Olofsson et al. (2014) recommended good practice protocols to estimate unbiased change areas from a probability sample of reference data that is independent of training data and provides more precise reference information than the maps being evaluated (Stehman, 2013). Yet many studies on global scale expansion of urban areas or impervious surface lacked this crucial component when they reported areas of interests counted directly from classified maps, resulting in biased numbers without quantification of uncertainty (Gong et al., 2020; He et al., 2019; Liu et al., 2018).

The three steps of “good practices”, sampling design, response design and analysis, should all follow probability sampling theory. In the first step, a sampling unit can be a pixel or a polygon depending on study objectives. Randomization should be incorporated in the sample selection to enable an inclusion probability of each

sampling unit. The inclusion probability prescribes the likelihood of a given unit being selected (Stehman, 2000). The randomization method can be simple random, stratified random, or systematic (Stehman, 2009). Systematic sampling is simpler for reference data collected from field visits and when the reference data is simultaneously used for all land classes (Stehman, 2009), as implemented in the global land cover map based on Landsat data (Gong et al., 2013). Many national forest inventories also adopt systematic sampling design (Olofsson et al., 2014). When reference data will be collected from satellite or aerial images, simple random sampling is preferred for unbiased variance estimation. When sampling efficiency and estimation uncertainty are both considered, stratified random sampling is often the best option (Broich et al., 200X; Tyukavina et al., 2013). For example, Sleeter et al. (2013) employed stratified sample to estimate land cover change in the conterminous United States between 1973 and 2000. Specifically, constructing strata by map classes of prioritized objectives will reduce standard errors of estimates of the target classes. The sample size required to meet a desired uncertainty will be many times smaller than systematic or simple random, especially when the map class takes a small proportion of the whole study area. The idea is that an accurate map can efficiently help the allocation of samples to targeted themes. If the study area of interest covers various and distinctive regions, such as biomes or climatic zones, additional stratification by regions will further reduce standard errors of region-specific estimates (Olofsson et al., 2014). The core idea, which will be applied throughout the dissertation, is using stratified random sampling with strata being

formed from reliable maps to produce scientifically rigorous and transparent estimates of accuracy and area.

When field collection of reference data is inevitable, and the cost is high for data collection, cluster sampling is recommended. Clusters can be stratified by different densities of priority objectives (e.g., forest cover loss) from a coarse resolution map, and reliable higher resolution maps of sampled clusters can serve as reference for area estimation (Hansen et al., 2010). Field collection of full coverage of reference data per sampled cluster can be expensive. A two-stage stratified clustering sampling approach, which combines cluster sampling with stratified random sampling of classified pixels within a cluster, can substantially reduce the cost, but also add complexity to the sampling design, response design and analysis (Feng et al., 2016; Song et al., 2017).

Good practices suggest assigning attributes to reference samples, such as change area, change driver, and change date (Olofsson et al., 2014). Attribution of sample can be incorporated into analysis for area estimation of each attribute. For example, carbon densities of forest loss sample within a stratum represent the probability distribution of carbon reduction in forest stock of certain stratum, and carbon loss attributed to different drivers of forest loss in an area of interest can be quantified (Tyukavina et al., 2017, 2015). While Chapter 4 will explore an automatic method to map drivers of bare ground gain, Chapter 2 and 3 will employ map-stratified sampling approaches for temporal estimation of bare ground gain drivers.

1.1.3 State and challenges of remotely sensed indicators of macro-economic development

Tracking economic change, whether via financial indicators or remotely sensed proxies, is critical to fostering economic health, warning of potential risks and addressing needs for improved governance, investment and livelihoods. Conventional statistics of global and regional economies are aggregations of national statistics that measure overall economic activity (Commission, 2009; Piketty et al., 2018). Implementation of national accounts systems (SNA) is expensive and typically has up to a one-year delay (Bandholz and Funke, 2003):

"National accounts data provide information covering both different types of economic activities and the different sectors of the economy. It is possible to monitor the movements of major economic flows such as production, household consumption, government consumption, capital formation, exports, imports, etc., in both value and volume terms. Moreover, information is provided about certain key balancing items and ratios which can only be defined and measured within an accounting framework, for example, the budget surplus or deficit, the share of income that is saved or invested by individual sectors of the economy or the economy as a whole, the trade balance, etc. The SNA also provides the background against which movements of short-term indicators, such as monthly indices of industrial production, consumer or producer prices can be interpreted and evaluated. The monitoring of the behavior of the economy may be significantly improved if at least some of the main aggregates of the SNA are compiled quarterly as well as annually, although many of the accounts,

tables or balance sheets of the SNA are not usually compiled more frequently than once a year." (Commission, 2009)

Existing proxies derived from nighttime satellite data have been examined for predicting economic outcomes. The Defense Meteorological Satellite Program (DMSP) Operational Linescan System (OLS) observed land area lit by visible-near infrared emissions. Elvidge et al. (1997) found that anthropogenic lit area was spatially correlated to gross domestic product (GDP) and electric power consumption. Using sophisticated statistical models, Chen and Nordhaus (2011) found luminosity, a measure of light intensity emanating from nighttime light radiance of a geographical area, was informational for countries with no reliable demographic or economic censuses. However, neither calibrated nor stable lights could be used as a reliable proxy for output in low-density regions because the low-density lights were hardly distinguishable from the background lights. For countries and regions with high-quality economic data, the value added by the luminosity as a proxy was small because luminosity data had relatively higher measurement errors than that of standard economic data. Henderson et al. (2012) further confirmed that changes in nighttime lights as a measure of economic growth over long term have roughly equal value as low-quality national accounts. Nevertheless, the sensitivity of nighttime lights to short-term economic fluctuations is not clear.

Recently, new resources from satellite images, cellphone metadata and social network emerged for indicating economic activities spatially in African developing countries (Blumenstock et al., 2015; Eagle et al., 2010; Jean et al., 2016). However,

the predictability of those methods at temporal scale, especially predicting economic booms or recessions of an economy, remains a challenge. For example, landscape features extracted from high-resolution satellite images were effective in predicting consumption or assets in African areas where people live under international poverty line (Jean et al., 2016), but its ability to predict changes in economic outcomes over time at global or regional scale was not evaluated.

Landsat features global acquisitions and near-weekly revisit rates. Reliable indicators derived from Landsat observation may substantially enhance the spatio-temporal details of economic activities and considerably reduce the cost of monitoring. It is posited here that Landsat-based estimates of human-induced bare ground gain could be a remotely sensed indicator of economic development. As a change variable, bare ground gain reflects significant investments in activities that reflect the demands of a growing population and economy for housing, energy, commerce, and services (Wang et al., 2019). For example, the area of resource extraction driven by demand within global markets may reflect domestic and global investment and activity in mining sector (Barbier, 2000; Bridge, 2004). The increase in built-up area was used to infer urban growth and to aid modeling and predicting the spatial expansion of urban land (Angel et al., 2011; Seto et al., 2012; Seto and Kaufmann, 2003). Bare ground gain is a physical land cover change that is generically detectable, which enables its application for all countries and economies of different sizes. Chapter 3 will explore the relationship between bare ground gain

dynamics and economic time series data and test the hypothesis of bare ground gain being a new indicator of macro-economic activities.

1.2 Research questions and objectives

This research is driven by three questions: 1) Can global bare ground change be accurately mapped and used to quantify global spatio-temporal dynamics of bare ground gain? 2) Can quantified time-series estimates of bare ground gain and associated drivers serve as a leading economic indicator? 3) Can the attribution of land uses associated with bare ground gain be characterized using deep learning methods?

To address these questions, I develop an approach to quantify spatial and temporal patterns of global bare ground gain, which combines the state-of-the-art advantage of remote sensing and map-stratified sampling techniques for efficient and unbiased area estimation and uncertainty assessment. The approach is then extended to attribute drivers of bare ground gain, including resource extraction, infrastructure development, commercial/residential built-up, transitional bare ground gain, greenhouses and natural dynamics.

For question 2, temporal dynamics of bare ground gain and economic data are employed to assess if bare ground may be used as an indicator of economic activity data. Annual change rates of bare ground gain and associated uncertainties within the 95% confident intervals are estimated globally and regionally to delineate temporal trends in bare ground gain, which are then combined with economic variables in

econometric models to test the predictability of bare ground gain on macro-economic development.

Drivers of bare ground gain consist of components in different shapes, texture, spectral reflectance and configuration of spatial features. For example, roads are featured by a continuous linear shape, oil wells present discrete rectangular patches, residential suburbs exhibit assembled granules of houses and vegetation, and central business district skyscrapers manifest a mix of impervious surface and shadow. Unlike per pixel land cover classification approaches, object-based methods are a possible way to effectively characterize drivers of bare ground gain. Airports, as one example, are an important component of transportation infrastructure, and have a unique spatial pattern and shape consisting of runways and terminals. As such, they are an appropriate test target for mapping a specific bare ground land use. To answer question 3, an approach using faster region-based convolutional neural networks (Faster R-CNN) (Ren et al., 2017) is implemented to detect national-scale airport locations using Landsat imagery for the first time.

1.3 Dissertation structure

The dissertation contains five chapters. The diagram in Figure 1-1 illustrates the structure of three research chapters. Chapter 1 introduces the context and rationales of studying bare ground gain, reviews methods and challenges in existing research, and identifies questions and objectives to be addressed in this dissertation.

Chapter 2 estimates global bare ground gain areas and uncertainties from a stratified random sample with strata consisting of classified maps of bare ground gain derived using time-series Landsat data. A probability-based sample is then selected and interpreted with gain/no-gain status and for gain, driver information interpreted in generating unbiased estimates of bare ground gain area at global, regional and national scales. Attributions of bare ground gain to six categories of drivers are labeled to each gain sample, the counts of which represent the proportions of related drivers in respective strata.

Chapter 3 utilizes the approach and data developed in Chapter 2 and extends to temporal change rates of bare ground gain. Temporal trend of economic development in the same period is characterized by the time series of selected economic variables from economic output, trade and energy data. Econometric panel data analysis is employed to quantitatively investigate the predictability of bare ground gain on changes in macro-economy.

Chapter 4 implements deep learning algorithms to identify airport locations in the conterminous U.S. with Landsat data. This study is meant to demonstrate the potential for replacing image interpreted labels of outcomes/drivers of bare ground gain with an algorithmic approach. The study is a demonstration of that potential. Given its full realization, all bare ground gain samples would be automatically labeled as one of the six categories of drivers.

Chapter 5 summarizes findings and contributions from research in Chapter 2-4, discusses strengths and limitations of present studies, and provides outlook for future research.

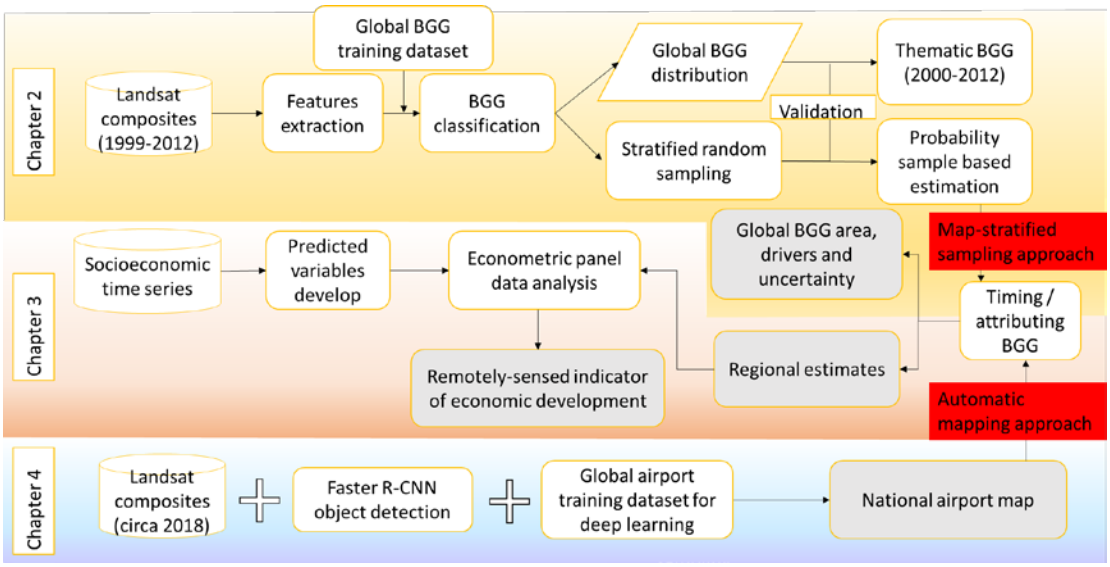

Figure 1-1 Structure of dissertation body

Chapter 2 Global bare ground gain from 2000 to 2012 using Landsat imagery[1]

2.1 Abstract

Bare ground gain, or vegetative cover loss, is an important component of global land cover change resulting from economic drivers such as urbanization and resource extraction. In this study, we characterized global bare ground gain from Landsat time series. The maps were then used to stratify the globe in creating a sample-based estimate of global bare ground gain extent, land cover/land use outcomes, and associated uncertainties from 2000 to 2012. An estimated total of 93,896 km^2 (±9317 km^2 for 95% confidence interval) of bare ground gain occurred over the study period. Human-induced bare ground gain accounted for 95% of the total and consisted of the following components: 39% commercial and residential development, 23% resource extraction, 21% infrastructure development, 11% transitional, and 1% greenhouses. East Asia and the Pacific accounted for nearly half of all global bare ground gain area (45%), with China alone accounting for 35% of global gain. The United States was second to China, accounting for 17% of total bare ground gain. Land cover/land use outcomes of bare ground gain varied between regions and countries, reflecting

[1] The presented material was previously published in Ying, Q., Hansen, M.C., Potapov, P. V., Tyukavina, A., Wang, L., Stehman, S. V., Moore, R., Hancher, M., 2017. Global bare ground gain from 2000 to 2012 using Landsat imagery. Remote Sens. Environ. 194, 161–176.

different stages of development and the possible use of bare ground gain as an indicator of economic activity.

2.2 Introduction

Land cover dynamics have been recognized as a key component of global environment change (Foley et al., 2005) and an important driver to a wide range of ecological, hydrological and climatic processes (Vitousek et al., 1997). Examples include deforestation, urbanization, and agricultural expansion, among others. Each land dynamic has a unique set of socio-economic-political drivers and resulting impacts on the earth system. The complete removal of vegetation due to land use changes such as the expansion of human settlements, open pit mining and infrastructure development represents an extreme land cover transition. This dynamic, which we term bare ground gain (Hansen et al., 2014), includes all vegetation cover loss. Though the conversion of vegetation cover to bare ground cover accounts for a small proportion of global land area, it merits attention for the following reasons. First, bare ground cover is a fast-growing land cover type associated with increasing population growth and urbanization. More than half of the world's 7 billion people live in urban areas with an additional 1.3 million urbanites per week (IPCC, 2015). The expected increase in urban area in the first three decades of the 21st century is projected to be greater than the cumulative urban expansion of all human history; urban area is growing on average twice as fast as urban population (IPCC, 2015). Second, bare ground gain completely alters the structure and functioning of ecosystems (Alberti, 2005; Foley et al., 2005;

Vitousek et al., 1997) due to the permanent or semi-permanent removal of vegetation, resulting in lower land carbon storage (Seto et al., 2012), reduced landscape evapotranspiration (Moran et al., 1996; Shukla et al., 1990), and increased surface albedo (Bonan et al., 1992); these effects impact ecosystem functions such as biogeochemical cycling of carbon and water, energy exchange, and biodiversity (Grimm et al., 2008; Kalnay and Cai, 2003). Lastly, bare ground gain merits attention because bare ground cover exhibits complicated spatio-temporal dynamics related to variations in driving forces (Ellis and Ramankutty, 2008; Lambin et al., 2003). For example, economic, demographic and institutional factors and their interactions not only drive local expansion of residential clusters, transportation infrastructure and industrial development (Seto et al., 2012), but also influence land-use change elsewhere (DeFries et al., 2010; Geist and Lambin, 2002). An improved understanding of bare ground gain and associated drivers at a global scale can inform future climate change mitigation actions and human adaptation strategies (IPCC, 2015).

Remotely sensed airborne/satellite data have long been used for bare ground-related land cover themes (Friedl et al., 2002; Gong et al., 2013; Hansen et al., 2003, 2011; Homer et al., 2004; Loveland et al., 2000) and bare ground gain (Hansen et al., 2014) monitoring at various spatial scales. However, definitions related to bare ground cover vary, e.g., continuous versus discrete (Hansen et al., 2003, 2011; Zhan et al., 2002), permeable versus impervious surface (Gong et al., 2013; Homer et al., 2004; Xian and Homer, 2010), natural exposed soil, rock or sand versus anthropogenic built-up environments (Friedl et al., 2002; Loveland et al., 2000). Hansen et al. (2014) featured

bare ground gain in strictly cover terms (i.e., the change from vegetation to non-vegetated state) whereas other studies (Schneider, 2012; Sexton et al., 2013; B. Wang et al., 2010; Wang et al., 2012; Xian and Homer, 2010) characterized impervious surface (non-evaporating, non-transpiring imperviousness) or contiguous patches of human built-up area as an indicator of urban land use extent. Stable night light data from DMSP-OLS (the U.S. Air Force Defense Meteorological Satellite Program-Operational Linescan System sensors) and VIIRS (Visible Infrared Imaging Radiometer Suite) have been used to map the extent and growth of lighted areas associated with urban areas with limitations related to per capita energy use and satellite intercalibration (Small et al., 2005; Zhang and Seto, 2011). Land uses such as open pit mining or quarries fall outside of most natural bare land, impermeable surface or built-up land cover classification legends. In our definition, bare ground cover includes natural and anthropogenic non-vegetated land surfaces. Hence, we characterize bare ground gain as complete land conversion from vegetative cover to non-vegetative cover.

Following previous research by Hansen et al. (2003,2011,2014), bare ground gain is defined as a process of land cover change featuring complete or semi-permanent (at least 3 years) clearing of vegetative cover (i.e., a pixel experiences an increase in bare ground cover of over 50% or experiences a transition to 80% or greater bare ground cover) by either human or natural-induced disturbances. This land cover dynamic has the advantage of being defined without regard to land use or attributes such as imperviousness, allowing for a more efficient algorithmic implementation. As a result,

a generic spectral signature of vegetated to non-vegetated state can be characterized and extended over large areas; herein, we employ 30m spatial resolution Landsat data to map bare ground cover and bare ground gain at the global scale.

Human-induced bare ground gain is due to residential, commercial, industrial, and transportation development as well as excavation and infrastructure related to resource extraction. Naturally-induced bare ground gain results in the exposure of rubble, lava, sand bars and other features caused by, for example, landslides, volcanic eruptions, and river meanders. All human and naturally-induced bare ground gain land changes are distinct from agricultural or forestry land use practices that include ephemeral bare ground cover states. While an agricultural fallow or intensive tree harvest may in some cases result in an extended period of bare ground exposure, these cases are not included in the permanent or semi-permanent transformation of vegetated land covers to bare ground dominated land covers. We identified six bare ground gain land cover/land use outcomes, five of which are human-induced: resource extraction, infrastructure development, commercial/residential built-up, transitional bare gain and greenhouses. Natural bare ground gain dynamics were considered as a single dynamic. See Methodology section 3.2 for the formal list of land cover/land use outcomes.

Recent developments in optical remote sensing hold tremendous promise for systematic monitoring of global bare ground cover and gain. Hansen et al. (2003) employed a regression tree model to produce the first global continuous fields of percent bare ground cover from Moderate Resolution Imaging Spectroradiometer (MODIS) data. The open access to the USGS Landsat data archive (Woodcock et al.,

2008) enabled further improved thematic representation of bare ground cover and gain at Landsat-scale over the conterminous United States (CONUS) through Web-Enabled Landsat Data (WELD) (Hansen et al., 2014). Challenges to using Landsat data over large areas include unequal observation coverage due to cloud cover, scan-line corrector off (SLC-off) gaps, and variation in the number of Landsat acquisitions (Kovalskyy and Roy, 2013). Results for CONUS (Hansen et al., 2014) yielded a binary description (gain/no gain) of bare ground gain with user's and producer's accuracies of 62% and 75%, respectively, when adjacent errors were excluded. Common errors in bare ground gain for land use change mapping include commission errors over croplands with extended fallows and omission errors for developed areas within semi-arid landscapes (Hansen et al., 2014).

The study presented here characterizes bare ground gain using Landsat time-series inputs and employs the resulting maps to stratify the global land surface into areas of likely bare ground gain. A sample of over 5000 pixels was selected to assess map accuracy, estimate area of bare ground gain, and estimate the proportion of area gain attributable to different bare ground gain dynamics. Probability-based sampling methods are regularly used in forest inventories and in remote sensing applications for assessing map accuracy and estimating area (Olofsson et al., 2014). Due to inherent errors in land cover change maps derived from remotely sensed images, change areas obtained from pixel counting are likely biased (Olofsson et al., 2013). Instead, unbiased estimates of area of land cover change area may be produced using the sample and reference classification of change (Stehman, 2013). The map provides a way to target

the sampling to a class of primary interest, in this case bare ground gain, via strata that provide sampling efficiencies greater than achieved by simple random or systematic approaches (Broich et al., 2009). For example, cities, towns and settlements account for < 1% of global land area (Schneider et al., 2010). Given the relative rarity of such land uses compared to the overall land surface, accurate area estimation is a challenge. Here, we are interested not only in mapping the class, but its increase over time, which is an even rarer land theme. To do so, we employ a change map of sufficient quality to construct strata that allow intensifying the sample into potential change areas. The mapped change strata serve to target the theme of interest and greatly reduce the standard error in providing unbiased estimates of change.

Another advantage of a sample based approach is the ability to determine additional contextual information such as land cover state prior to change, land use drivers and the timing of changes for the sampled pixels (Tyukavina et al., 2015). In the study of Tyukavina et al. (2015), forest cover loss was assessed, with all sample pixels interpreted for forest type (natural or managed), allowing for development of a more complete narrative of forest cover loss. We build on this approach in quantifying global bare ground gain dynamics. Specifically, we estimate the area of land converted to a non-vegetated state and attribute this dynamic to a set of bare ground gain land cover/land use outcomes.

2.2 Data

We employed Landsat mosaics from the research of global forest dynamics of Hansen et al. (2013) as inputs for mapping. In their study, 654,178 growing season Landsat 7 Enhanced Thematic Mapper Plus (ETM+) scenes from a total of 1.3 million stored in Google Earth Engine cloud platform were analyzed to form a global seamless composite dataset available annually from 1999 to 2012. Annual seamless composite images consist of Landsat 7 ETM+ per band median reflectance values of all cloud/shadow free growing season observations. Growing seasons were defined using MODIS phenology data and all Landsat observations processed therein. Cloud, shadow and water were screened for every pixel using a series of quality assessment models. Viable land observations were normalized to top of canopy reflectance for spectral ETM+ Red (0.631- 0.692 µm), Near-Infrared (NIR 0.772- 0.898 µm) and two Shortwave Infrared bands (SWIR 1.547- 1.749 µm and 2.064- 2.345 µm) (Potapov et al., 2012, 2015).

Two additional normalized difference band ratios were derived for their ability to facilitate the characterization of land conversion from vegetation cover to bare ground cover. Annual growing season minimum greenness (Normalized Difference Vegetation Index) values were computed as was a normalized difference built-up index (NDBI) (SWIR 1.6 µm - NIR)/(SWIR 1.6 µm + NIR) (Zha et al., 2003) using the median growing season data.

2.3 Methodology

2.3.1 Global bare ground gain characterization

A host of land cover change methods exist (Coppin et al., 2004; Singh, 1989). In this study, we characterize bare ground gain both directly as a class (see section 3.1.1) and indirectly using post-characterization comparison of annual percent bare ground cover layers (see section 3.1.2). The work flow of global bare ground gain characterization using the direct and indirect methods is illustrated in Figure 2-1. Annual Landsat mosaics were inputs for both direct bare ground gain mapping (Figure 2-1 left column) and indirect bare ground mapping (Figure 2-1 right column). Classification trees were used for directly mapping bare ground gain from 2000 to 2012. For the indirect mapping of bare ground gain from 2000 to 2012, we used regression trees to map annually bare ground cover from 1999 through 2012 and then developed rules for determining from these annual maps whether bare ground gain had occurred.

Training data for directly mapping bare ground gain were delineated as gain/no gain labels by interpreting stacks of Landsat images supplemented by high resolution images from Google Earth ™ (section 3.1.1.2). Additional ancillary data to add to the bare ground gain training in the USA included imperviousness change data from the National Land Cover Dataset (NLCD) (Jin et al., 2013; Xian et al., 2011) and bare ground gain data from the WELD dataset (Hansen et al., 2014). Training data were related to a set of multi-temporal metrics (see metric explanation in section 3.1.1.1), or

statistical derivatives of the annual Landsat composite images, using a classification tree. Classification tree models were applied in an active learning mode, with global bare ground gain products iteratively created until a final, acceptable result was achieved based on expert interpretation (section 3.1.1.3). The final result was a classification of pixels having experienced bare ground gain from 2000 to 2012.

Annual percent bare ground cover layers were created using a regression tree model, equivalent to the MODIS Vegetation Continuous Field (VCF) and Landsat-based WELD products (Hansen et al., 2003, 2011). For these antecedent studies, time-series data sets were related to fractional cover training data using regression trees in order to estimate per pixel percent bare ground. Both products were used as training data in this study per the approach of Hansen et al. (2014). Post-characterization rules of bare ground increase $\geq 50\%$ over a consecutive three year period were employed to classify bare ground gain from 2000 to 2012 using the series of annual bare ground cover maps (section 3.1.2).

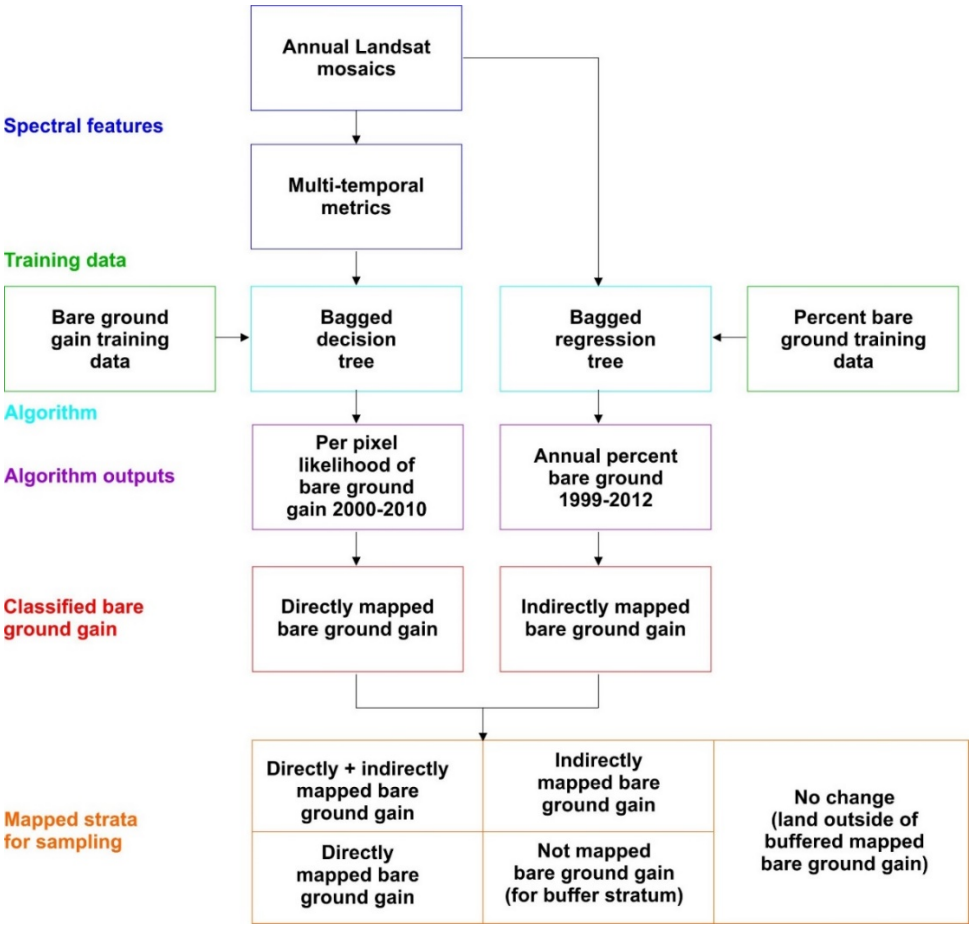

Figure 2-1 Work flow of global bare ground gain characterization. Annual Landsat mosaics are inputs. Two bare ground gain characterization methods are shown: direct bare ground mapping and indirect bare ground gain mapping. Colored boxes identify training data, algorithm and output maps applied to each mapping method. Orange boxes at bottom show the structure of mapped strata for validation and sample-based area estimation. Note that mapping is not used for area estimation, but as strata for sample-based area estimation.

2.3.1.1 Direct bare ground gain mapping

2.3.1.1.1 Multi-temporal metrics extraction

The spectral profiles of bare ground gain pixels vary greatly because of the complicated spatio-temporal characteristics of bare ground extent and change. For example, the spectral profiles of conversions differ by the timing, duration, magnitude, and reference start and end states (Figure 2-2). From the annual composites and indices, we computed multi-temporal metrics meant to capture interannual spectral variations suitable for characterizing bare ground gain. The method of deriving metrics from satellite time series has been used in land cover change studies of forest loss and bare ground gain (Hansen et al., 2008). Five groups of per band metrics were created: (1) earliest and latest cloud-free observation composites and median value of 3 earliest/latest observations; these metrics represent interval endpoints and their respective differences (earliest – latest; median 3 earliest – median 3 latest) are a generic indicator of change; (2) statistical measures of minimum/maximum annual values and the median value of 3 highest/lowest observations from the multi-year profiles; these metrics represent extreme values within the annual inputs; their differences (max - min, median 3 max - median 3 min) are indicators of change magnitudes; (3) average of all years of annual inputs; (4) slopes of linear regression models of annual input values versus year; (5) maximum change for both increase and decrease segments and corresponding endpoints in respective annual profiles. A total of 21 metrics were created per band and ratio and annual bare ground cover inputs, resulting in a set of 147 feature metrics (Table 2-1).

2.3.1.1.2 Global training dataset of bare ground gain

The most definitive way to obtain reference information for training data to classify bare ground gain would be to collect field data over time, an impractical option for global studies. Google Earth data offer high-resolution historical images that cover roughly 20% of the Earth's landmass and more than a third of the human population (Potere, 2008) with coverage improving over time. A wide variety of plug-ins and tools built upon Google Earth facilitate global land change research (Fritz et al., 2009). Because of the efficiency in visualizing the trajectories of historical change of areas of interest, Google Earth has been exploited in a wide range of land cover change studies (Hansen et al., 2011). In this study, Google Earth was employed in both training and validation, with Landsat annual composites used for both activities.

A global training data set for bare ground gain classification was developed through visual interpretation and on-screen delineation of gain and no gain classes. A three feature false color composite consisting of the median value of 3 earliest, latest and maximum observations in percent bare ground cover was used in training data delineation. Start and end date images of Landsat false color composites and Google Earth time slider imagery were also used to facilitate interpretation.

A particular focus of training data derivation is precise labeling of boundary pixels which is important for improving the accurate characterization of mixed pixels (Hansen, 2012; Hansen et al., 2014). In active learning mode, training data were delineated and iterated until little or no improvement in successive versions was observed. Metropolitan areas such as Washington D.C., Dallas, Manchester, Moscow,

Istanbul, Lagos, Dubai, Shanghai, Beijing, Manila and Melbourne were trained in order to represent a wide range of urbanization dynamics. Oil and gas drilling and mining sites were sampled across the globe, from China to Russia and the USA and Canada to Peru and Australia. In addition to adding bare ground gain training data, commission errors were targeted, largely in fallowed agriculture lands. Training data were regionally complemented by adding gain and no gain pixels outside our delineated polygons where WELD bare ground gain layer and NLCD percent developed imperviousness change layer agreed (>10% imperviousness increase regarded as NLCD gain, others as NLCD no gain) for the purpose of enlarging no gain training. Exclusion of ephemeral changes, even sometimes lasting more than one year, such as post-clearing forest patches, agricultural fallows, and seasonal changes of shallow water, was sought in the delineation of training data. Pixels with noise patterns associated with inter-annual bare ground cover variations, such as high latitude snow/ice cover, were also added to the no bare ground gain class. The effort to include pixels of likely false positive bare ground gain in the training data is critical to improving the user's accuracy of the final product. The global training data set for bare ground gain classification totaled 27,471,758 Landsat pixels, of which 188,860 were gain pixels and 27,282,898 no gain pixels.

2.3.1.1.3 Classification tree model for bare ground gain detection

Decision trees have been widely used in classifications of large area land cover extent and change (Hansen et al., 2000, 2014; Potapov et al., 2015; Schneider et al., 2010; Weber et al., 2009). Tree models have been shown to perform better in urban

area land cover change detection compared to support vector machines (SVM) (Schneider, 2012). Decision trees are a supervised classification algorithm that recursively partitions a training data set into more homogeneous subsets with regard to class membership until certain conditions are met (Breiman et al., 1984). A bagging technique was employed to reduce overfitting in individual tree models (Breiman, 1996). Considering the number of tree models and the structure of training data set, we used equal sampling rate (20%/20%) of delineated training for gain/no gain classes and unequal rate (10%/0.1%) for complementary training data obtained from existing products. Seven bagged trees (Figure 2-1 left blue box) were built via repeatedly sampling the training data (Potapov et al., 2015) and then applied to predict per pixel bare ground gain probability (Figure 2-1 left purple box). A pixel was labeled as bare ground gain when the per pixel median value of all tree models was > 50% (Figure 2-1 left red box).

Table 2-1 Summary of multi-temporal metrics extracted from Landsat 7 temporal profiles

Multi-temporal metrics extraction	Names
7 Features	Four spectral bands: median growing season Red, NIR, SWIR 1.6 µm, SWIR 2.2 µm Two indices bands: minimum growing season NDVI, median growing season NDBI Percent bare ground cover
21 Multi-temporal metrics per band	Six temporal metrics: earliest, latest, median 3 earliest, median 3 latest, earliest - latest, median 3 earliest - median 3 latest Six time-integrated metrics: maximum, minimum, median of 3 maximum, median of 3 minimum, maximum - minimum, median of 3 maximum - median of 3 minimum Mean of all years Slopes of annual input values versus year Six maximum bare ground gain increase / decrease metrics: start point, end point and magnitude of maximum increase and decrease from annual profiles
Total	147 feature metrics

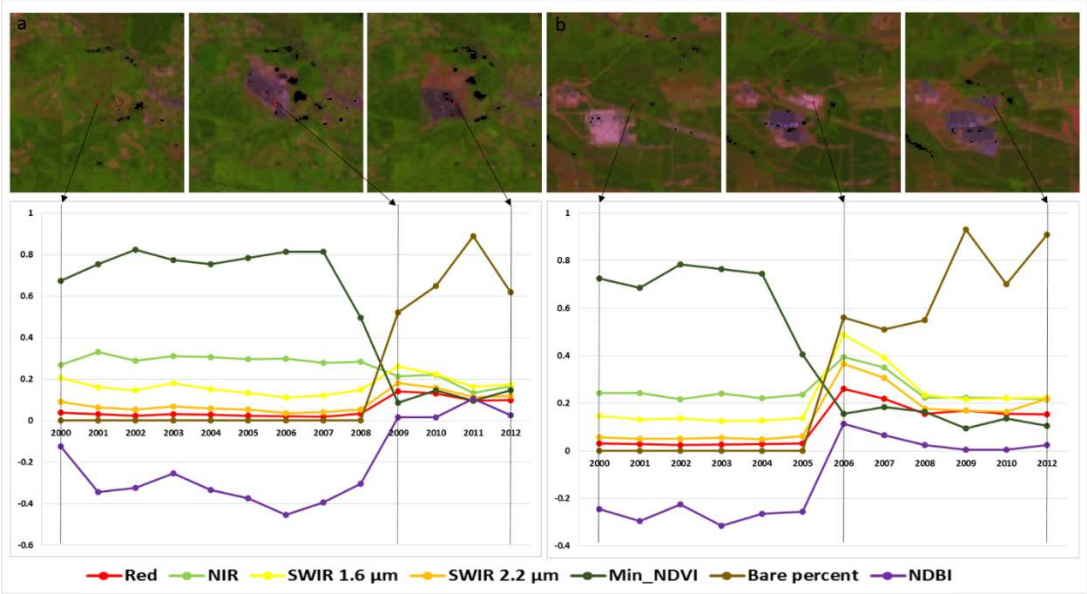

Figure 2-2 Band profiles of bare ground gain pixels from (a) a coal mining site in Alabama, USA, centered at 33 ^{0}53'20"N, 87 ^{0}32'36"W and (b) a power plant in North Carolina, USA, centered at 34 ^{0}50'32"N, 79 ^{0}44'8"W, above which are Landsat false color composites of SWIR (1.6 µm), NIR and RED bands corresponding to the start, change and end year.

2.3.1.2 Indirect bare ground gain mapping

The indirectly mapped bare ground gain was produced based on the concept of post-characterization mapping using the consecutive annual bare ground cover layers as inputs. A pixel was defined as bare ground gain if it had experienced an increase in bare ground cover of at least 50% within a consecutive three-year period. Specifically, as shown in Eq. (1), we first extracted a time sequence of bare ground cover ($\widehat{x_t}$) that was stable within a consecutive three-year period for a pixel from its annual percent bare ground cover time series (x_t). Then we mapped the pixel as bare ground gain if the maximum increase of the time sequence $\widehat{x_t}$ was equal to or larger than 50% as

shown in Eq. (2). To meet the consecutive three year constraint, we used percent bare ground cover data starting from 1999 for calculating stable bare ground cover in 2000. We only used year t-1 and t percent bare ground cover to define stable bare ground cover in 2012 as we did not have year 2013 data at the time of the study.

$$\hat{x_t} = median(x_{t-1}, x_t, x_{t+1}), if \max(x_{t-1}, x_t, x_{t+1}) - \min(x_{t-1}, x_t, x_{t+1}) \leq 30\% \quad (1)$$

$$Pixel\ i\ is\ classified\ as\ bare\ ground\ gain, if\ \Delta\hat{x} \geq 50\% \quad (2)$$

2.3.2 Sampling design for accuracy assessment and area estimation

We implemented a stratified random sampling design for the purpose of providing area estimates of bare ground gain and for assessing the accuracy of the bare ground gain map. Land cover change typically represents a small fraction of the land surface at decadal time scales, meaning that any such assessment requires special attention to the change class. Khorram (1999) pointed out the difficulty in assessing land cover change map accuracy due to the difficulty in quantifying false negatives. Such errors of land change omission are found within a relatively huge stratum of mapped non-change. Considering that built-up land as a land category consists of only 0.5% of the land surface (Schneider et al., 2009), accurately mapping its change within a global context is a challenge. The mapped bare ground layers enable the creation of a set of strata designed to target likely areas of bare ground gain and associated errors.

The strata used in the sampling design were defined by a cross-classification of five climate domains with five map-based feature classes. The five climate domains were

tropical, subtropical, temperate, boreal and polar according to the eco-climate zones of the Food and Agriculture Organization (Simons et al., 2001; downloaded from FAO Map Data Global Ecological Zones). The five feature classes within each domain were defined by different combinations of the classifications produced by the direct and indirect bare ground gain products (Figure 2-1 bottom orange boxes). The first map feature consisted of pixels mapped as gain in both the directly and indirectly mapped products ("jointly mapped" bare ground gain as shown in red in Figure 2-3 strata inset). This layer represented the highest confidence feature class for bare ground gain. The "directly mapped" feature class was created using pixels identified as bare ground gain by only the direct mapping algorithm (as shown in yellow in Figure 2-3 strata inset), and the "indirectly mapped" feature class was created using pixels identified as bare ground gain only by the post-characterization comparison (as shown in blue in Figure 2-3 strata inset). A fourth "buffer" feature class was defined by all pixels within 90m of any pixel included in any of the first three map feature classes (as shown in dark gray in Figure 2-3 strata inset). This buffer class was designed to increase the likelihood of sampling bare ground gain omission errors, which presumably would be more likely to occur in areas proximate to mapped bare ground gain. A fifth "mapped no gain" feature class consisted of all the terrestrial pixels not identified by the aforementioned four feature classes (as shown in white in Figure 2-3 strata inset). The five climate domains combined with the five map features resulted in a total of 25 strata, and the area covered by these 25 strata is the population to which inferences from the sample data apply (Table 2-2). Figure 2-3 shows an example of the strata structure.

Figure 2-3 Example of stratification for Brawley, California (a 10 km by 6.5 km extent centered at 32°59'5"N, 115°30'33"W), within the subtropical domain. Strata are shown on the right image where red is jointly mapped gain (Stratum 6), yellow is directly mapped (Stratum 7), blue is indirectly mapped (Stratum 8), and dark gray is the 90m buffer (Stratum 9); white is mapped no gain (Stratum 10).

Globally, 5750 sample pixels (Figure 2-4) were selected using the stratified random design (Table 2-2) following "good practice" guidance on the use of probability-based sampling for area estimation (Olofsson et al., 2014). A sample is represented by a Landsat 30-m spatial resolution pixel. We first selected 4250 sample pixels with 4000 in bare ground gain strata and buffer strata and 250 in no gain strata. The allocation of the 4250 sample size per climate domain was approximately proportional to bare ground gain area of each domain: tropical, subtropical, and temperate domains were each initially allocated 1050 sample pixels and the boreal and polar domains were each allocated 550 pixels. Within each climate domain, we selected equal number of sample pixels from each of the four gain strata and 50 sample pixels from the no gain stratum. Initial results from the 4250 sample points revealed that the majority of bare ground gain estimation uncertainty was contributed from the buffer strata within the tropical, subtropical and temperate climate domains. Consequently, to reduce the standard error of the area estimate we added 500 sample pixels to each buffer stratum of the tropical, subtropical and temperate climate domains.

Reference information was derived via visual interpretation of thumbnail annual false color composites of SWIR (1.6 μm), NIR and RED for 3km by 3km (101 x 101 Landsat pixels) block centered on the sample pixel location. The thumbnails provide landscape context to facilitate interpretation of the sampled pixel. Sampled pixel boundaries were also projected onto Google Earth to facilitate interpretation for locations with very high spatial resolution imagery. When interpretation ambiguity due to poor geolocational agreement between Landsat pixels and Google Earth imagery occurred, priority was given to the interpretation of the Landsat time-series. The primary task was to assign if bare ground gain occurred or not. For reference sample pixels labeled as bare ground gain, the change year, antecedent land cover/use and attributes of bare ground gain drivers were interpreted and recorded.

Based on the USGS (United States Geological Survey) Anderson land classification scheme (Anderson, 1976), we define six classes of bare ground gain land cover and land use outcomes that constitute the dominant drivers of bare ground gain:

(1) Resource extraction: the removal of vegetation to gain access to mineral or energy commodities, including exploration and extraction activities for iron ore, limestone, gold, copper, zinc and other minerals, and coal, petroleum, natural gas and other fossil fuels;

(2) Infrastructure development: the construction of transportation and energy infrastructure including highways, railways, airports, container terminals, ferries, dams, power stations, pipelines, and manufacturing plants;

(3) Commercial/residential built-up: structures related to human occupation, such as residential homes and office buildings and including associated features like driveways and parking lots;

(4) Transitional bare gain: areas which are in transition from one land use activity to another. For example, the conversion of agricultural land to residential land use may exist in a bare ground cover state for an extended period and in fact not reach completion, for example the cancellation of a construction project due to changes in market conditions or financing. Spoil dumps and landfills which are also transitional in nature are also considered in this category;

(5) Greenhouses: a special category characterized by impervious roofing materials made of glass, polycarbonate or plastic panels used in the perennial production of fresh vegetables and fruits. This category is selected because greenhouses have similar or same spectral reflectance as other bare ground expansion areas;

(6) Natural bare ground gain: all naturally caused long term exposure of bare soil, sand and rock (for example by river meanders), dry salt flats, earthquake craters, and volcanic debris.

Table 2-2 Allocation of sample size to strata formed by the cross-classification of climate domains with map feature classes.

Stratum ID	Climate domains	Sample size	Map features	Sample size	Stratum area (km²)
1			Jointly mapped	250	1,897
2			Directly mapped	250	16,000
3	Tropical	1550	Indirectly mapped	250	15,425
4			Buffer	750	304,769
5			Mapped no gain	50	57,240,695
6			Jointly mapped	250	3,703
7			Directly mapped	250	17,471
8	Subtropical	1550	Indirectly mapped	250	27,975
9			Buffer	750	412,966
10			Mapped no gain	50	22,284,674
11			Jointly mapped	250	5,011
12	Temperate	1550	Directly mapped	250	19,359
13			Indirectly mapped	250	28,319

14			Buffer	750	455,944
15			Mapped no gain	50	27,624,553
16			Jointly mapped	125	664
17			Directly mapped	125	3,279
18	Boreal	550	Indirectly mapped	125	1,110
19			Buffer	125	60,380
20			Mapped no gain	50	18,923,617
21			Jointly mapped	125	26
22			Directly mapped	125	360
23	Polar	550	Indirectly mapped	125	771
24			Buffer	125	24,765
25			Mapped no gain	50	7,248,975

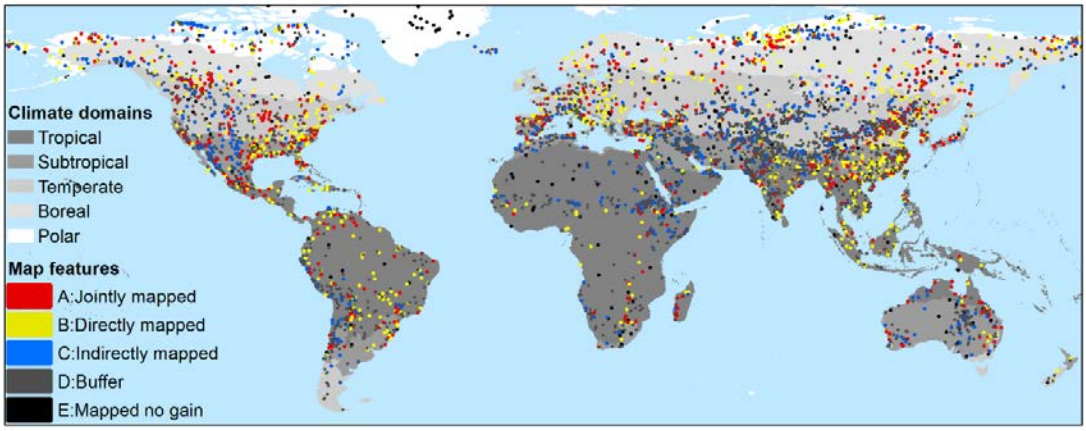

Figure 2-4 Stratified random sample with 25 strata defined from the cross classification of five climate domains with five map feature classes.

2.3.3 Accuracy assessment, area estimation and uncertainty quantification

We employ the method of Olofsson et al. (2013) that utilizes the error matrix obtained from validation to produce a stratified estimator of bare ground gain area based on the reference classification of bare ground gain. Bare ground gain area was estimated for each of the 25 strata within a region of interest, and the stratum totals were then summed to obtain the total estimate for a designated region such as global, continental or country areas. The bare ground gain area in stratum h is estimated as

$$\hat{G}_h = A_h p_h \quad (3)$$

where A_h is the total area in stratum h, $p_h = n'_h/n_h$ is the sample proportion of pixels interpreted as bare ground gain in stratum h, n'_h is the number of sample pixels interpreted as bare ground gain, and n_h is the number of sample pixels allocated to

stratum h. Then the total bare ground gain area is estimated by summing the area estimates over all 25 strata:

$$\hat{G} = \sum_{h=1}^{25} \hat{G}_h \quad (4)$$

We quantify the uncertainty of the area estimates in the context of design-based inference framework in which the uncertainty associated with the estimator is defined as the variability of the estimates over the set of all possible samples that could have been obtained for the chosen sampling design and population sampled. The standard error for bare ground gain area estimate is

$$S(\hat{G}) = \sqrt{\sum_{h=1}^{25} A_h^2 \frac{p_h(1-p_h)}{n_h - 1}} \quad (5)$$

A 95% confidence interval for bare ground gain area is

$$\hat{G} \pm 1.96 \times S(\hat{G}) \quad (6)$$

For map accuracy assessment, we use the estimation equations of Stehman (2014) because the strata are different from the map classes. Detailed descriptions of the formulas for user's, producer's and overall accuracy are presented in the Appendix.

Although we employed climate domains as strata in the sampling design, we are also able to report area estimates for other geographic regions if there is sufficient sample size within the region to assure a relatively low standard error. For example, we report results for continents/sub-continents and countries where sampling densities were sufficient to produce a reasonable standard error (e.g. China, the United States of America, Brazil, Canada, Russia, India, Mexico, Spain, Turkey, Australia). The hierarchy of continents/sub-continents is based on the geographic groupings of World Bank (Figure 2-5) that include all countries and economies with populations of ≥

30,000 (World Bank, 2016a). The World Bank has defined geographic regions for a wide range of development indicators and we use them to disaggregate area estimates of bare ground gain and associated land cover/land use outcomes.

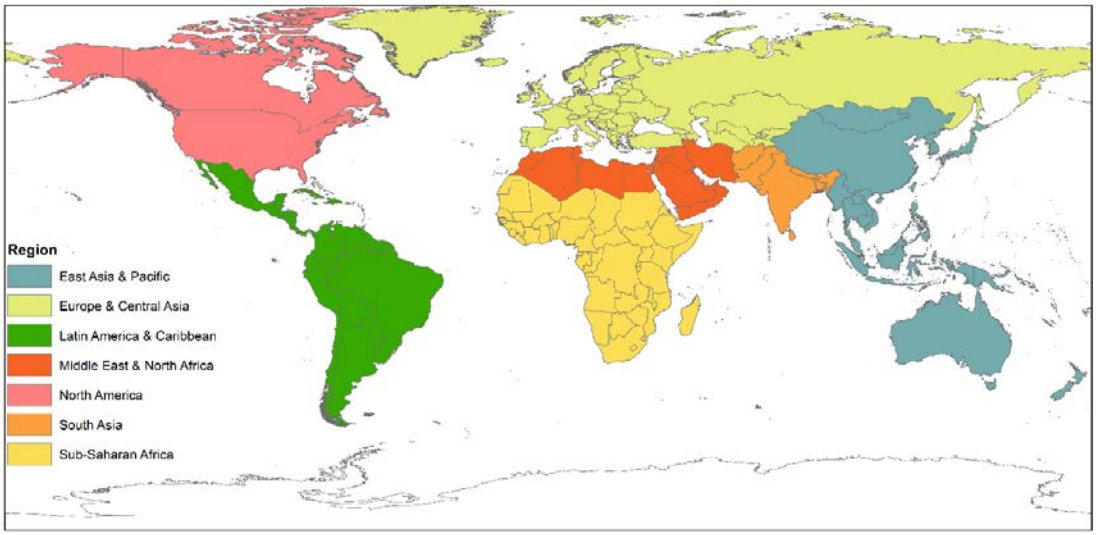

Figure 2-5 Boundaries of geographic regions from the World Bank for regional bare ground gain area reporting. The sample size located in each region is: East Asia and Pacific 1444, Europe and Central Asia 1416, North America 987, Latin America and the Caribbean 608, South Asia 486 and Sub-Saharan Africa 411, Middle East and North Africa 377. There are 21 sample pixels falling outside of the boundaries that we excluded from area estimation.

2.4 Results

2.4.1 Global bare ground gain characterization and stratification results

The area comprising the population from which the sample was selected is global terrestrial area between 80º N to 60º S. The mapped bare ground gain and associated buffer area covered 1,400,193 km^2 or approximately 1% of global land area. The mapped global bare ground gain area for 2000-2012 from the direct classification map totaled 67,771 km^2 (0.05% of global land area). Two example bare ground gain

landscapes of resource extraction and urbanization from the direct classification map are illustrated in Figure 2-6. Indirect mapped area totaled 85,172 km^2 (0.06% of global land area). To visualize the global distribution of bare ground gain, we assigned the sample-based stratum mean bare ground gain to each pixel in each stratum and then aggregated the result to a 0.05º spatial resolution (Figure 2-7a). Bare ground gain patterns are largely related to urban expansion, for example the metropolitan agglomerations of Houston-Dallas-San Antonio in Texas (Figure 2-7b) and the Beijing-Tianjin-Tangshan corridor in the North China Plain (Figure 2-7c). Infrastructure development is also readily visible in the bare ground gain maps. For example, expanding human settlements are connected by the growing transportation networks in Northern China (Figure 2-7c). Likewise, the construction of Dulles International airport in northern Virginia has driven concentrated development of satellite cities in the Washington, D.C. metro area (Figure 2-7b) (Song et al., 2016). Resource extraction is present in Figure 2-7b, including the East Texas oil field, the second-largest oil field in the U.S. outside of Alaska, and mountaintop removal mining in the Appalachian Plateau of West Virginia and Kentucky. These land cover/land use outcomes of bare ground gain were attributed to sample points during the validation procedure (Figure 2-8) to quantify the proportions of human-induced and natural bare ground gain.

The direct and indirect bare ground gain maps corresponded well with visually interpreted bare ground gain. We disaggregated errors by evaluating map accuracy for different combinations of map strata evaluated as the bare ground gain class (Table 2-3). For pixels identified as bare ground gain in both direct and indirect bare ground gain maps (namely jointly mapped pixels), commission error was just over 10% and

omission error was nearly 90%. Adding the directly mapped bare ground gain to the jointly mapped area increases commission error to 33% and reduced omission error to 50%. Following Hansen et al. (2014), we define adjacent errors as any omission or commission errors that were found within a 1-pixel distance from directly mapped bare ground gain. Adjacent errors are more likely related to geolocation and/or mixed pixel issues than errors that are isolated from correctly mapped change (Hansen et al., 2014). When adjacent errors were excluded, in other words the adjacent errors were not counted as error, the user's accuracy increased to 92% and producer's increased to 66%. In our directly mapped bare ground gain, 54% of omission errors were within one pixel of a labeled gain pixel and an additional 18% of omission errors were within two pixels of a labeled gain pixel. The addition of indirectly mapped bare ground gain further increased commission error to 62% but reduced omission error to 44%. Because we did not find any gain sample pixels from the mapped no gain strata, the inclusion of the buffer as mapped bare ground gain increased commission error to 93% but had no omission error, verifying our original purpose to employ the buffer strata for targeting false negatives. These results show the expected tradeoff between commission and omission errors as the area of mapped bare ground gain increases.

The accuracy estimates of both direct and indirect bare ground gain maps also varied by climate domains (Table 2-4). As expected, the overall accuracy was high for all climate domains because of the very small proportions of bare ground gain area. The general pattern of accuracy over the climate domains was that user's and producer's accuracies of bare ground gain were lower in the polar and tropical domains with higher accuracies in the subtropical, temperate and boreal domains. Adding directly mapped

bare ground gain to the jointly mapped gain gained the largest increase in producer's accuracy of bare ground gain class in boreal domain, but introduced the most reduction in user's accuracy in polar domain.

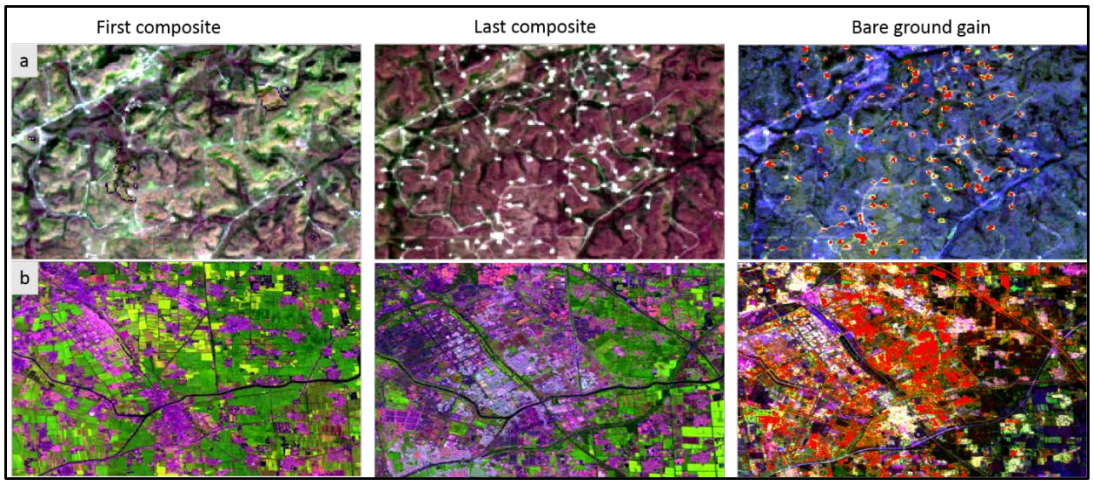

Figure 2-6 Landsat composites and directly classified bare ground gain: (a) Petroleum drilling in rural Texas centered at 30°24'33"N, 101°02'46"W; (b) Urbanization in Beijing, China centered at 39°48'01"N, 116°33'07"E. The first and last composites are Landsat false color composites of SWIR (1.6 µm), NIR and RED bands. Bare ground gain is shown in red on images of right panel with background displayed in the false color composite of median_max, median_latest and median_earliest in percent bare ground cover as RGB.

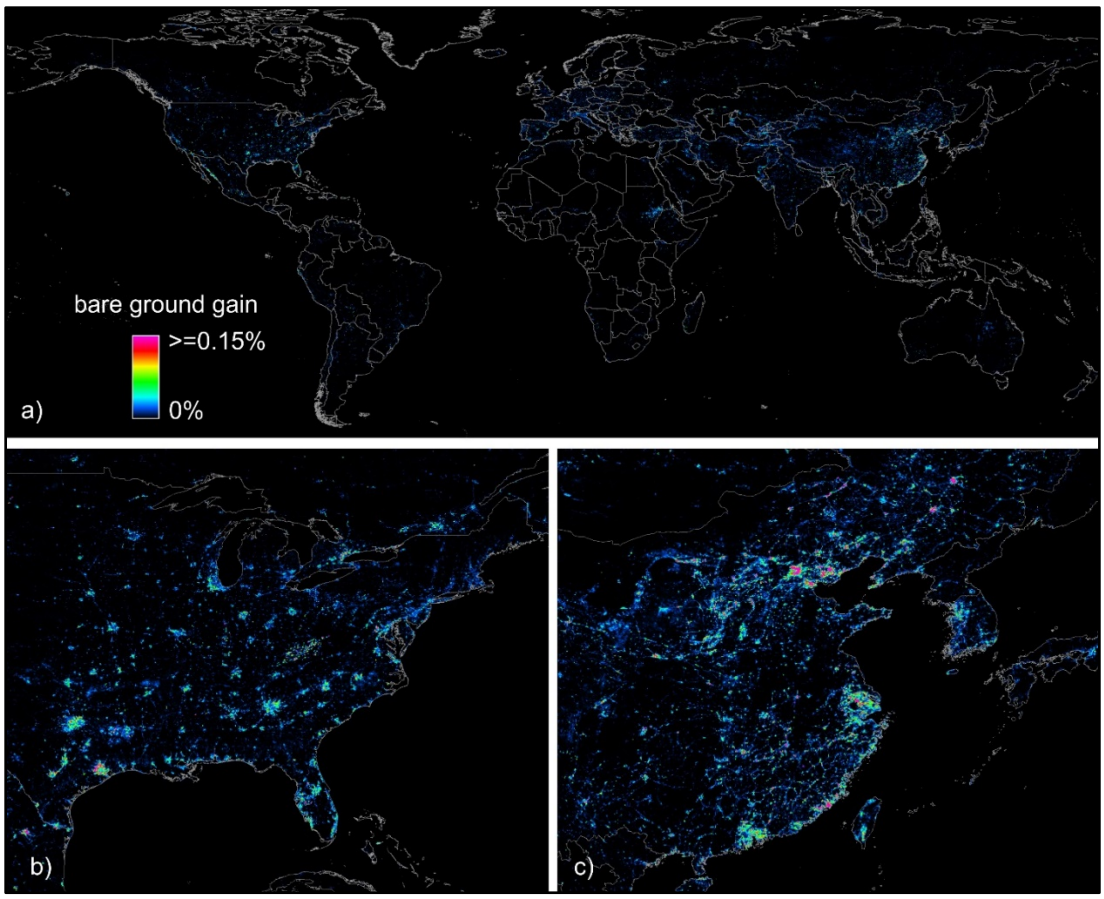

Figure 2-7 Percent bare ground gain aggregated from Landsat strata to 0.05º resolution in lat/lon geographic projection.

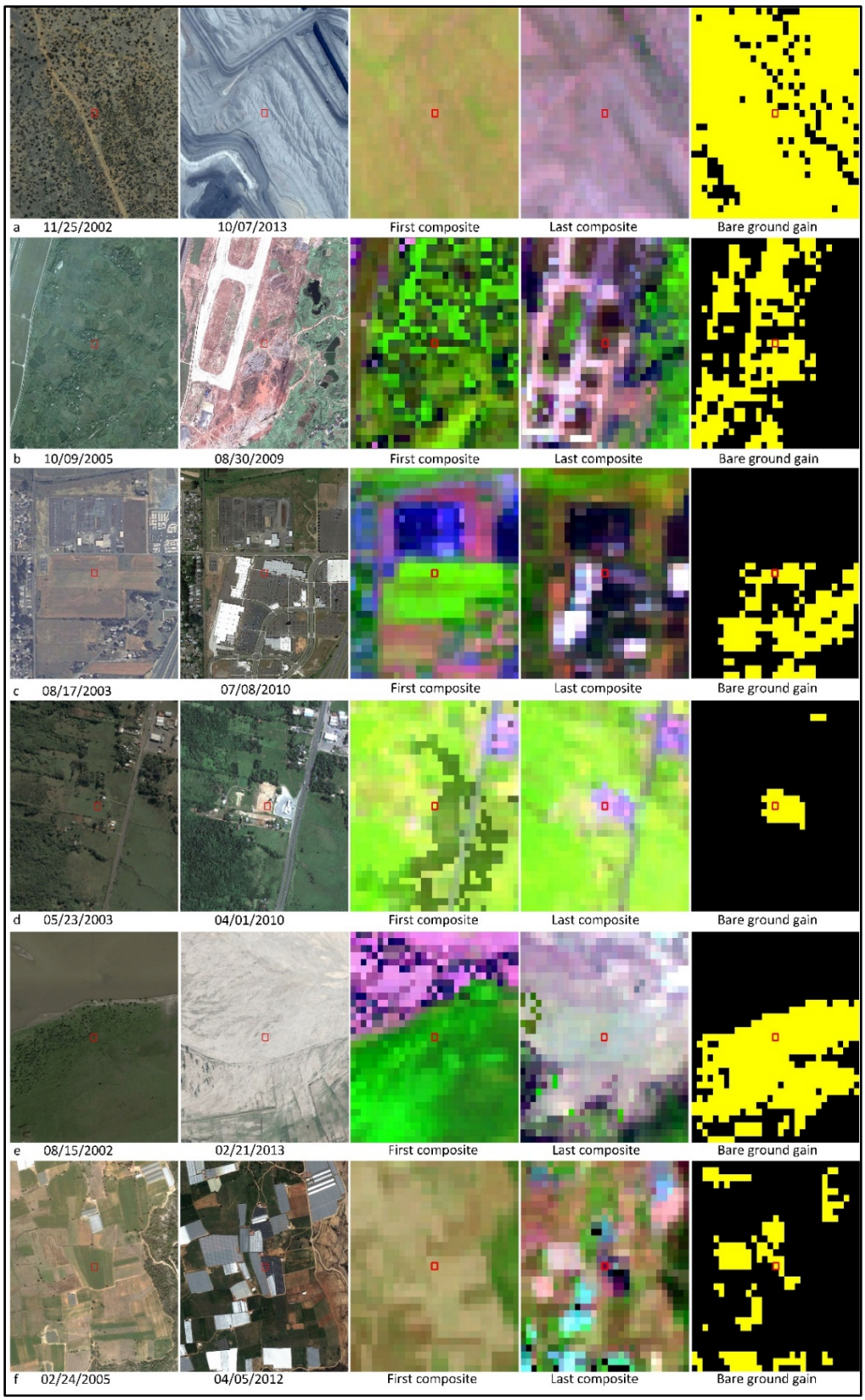
a 11/25/2002 10/07/2013 First composite Last composite Bare ground gain
b 10/09/2005 08/30/2009 First composite Last composite Bare ground gain
c 08/17/2003 07/08/2010 First composite Last composite Bare ground gain
d 05/23/2003 04/01/2010 First composite Last composite Bare ground gain
e 08/15/2002 02/21/2013 First composite Last composite Bare ground gain
f 02/24/2005 04/05/2012 First composite Last composite Bare ground gain

Figure 2-8 Examples of characterized bare ground gain land cover/land use outcomes in a 930m × 930m (31 × 31 Landsat pixels) block centered at sample points as shown in red square: (a) Resource extraction, coal mine in Queensland, Australia centered at 21°29'29"S 148°23'12"E; (b) Infrastructure development, airport runway in Chongqing, China centered at 29°42'29"N 106°38'35"E; (c) Commercial/residential built-up, shopping plaza in Oregon, U.S. centered at 45°0'46"N 122°59'54"W; (d) Transitional bare ground gain, bare field next to a building in Rio Grande do Sul, Brazil centered at 29°51'7"S 50°14'53"W; (e) Natural bare ground gain, river meander in Assam, India centered at 27°46'45"N 95°39'11"E; (f) Greenhouses in Antalya, Turkey centered at 37°0'16"N 30°50'49"E. Images from left to right column are: 1), 2) reference Google Earth time one and time two imagery; 3),4) Landsat start and end date composites of SWIR (1.6 µm), NIR and RED bands as RGB; 5) Direct bare ground gain classification results with gain in yellow and no gain in black.

Table 2-3 Accuracy and uncertainty (± margin of error for 95% confidence interval) estimates of the bare ground gain and no gain classes for different combinations of map features. Each row represents one of the objective bare ground gain maps and the accuracy estimates represent the global result combining the sample data for all five climate domains.

Map Feature	User's		Producer's		Overall
	Gain	No gain	Gain	No gain	
Jointly mapped	87.7 (±2.4)	99.9 (±0.01)	10.8 (±1.1)	100.0 (±0.00)	99.9 (±0.01)
Jointly mapped + Directly mapped	66.9 (±2.7)	99.9 (±0.01)	48.5 (±4.8)	99.9 (±0.00)	99.9 (±0.01)
Jointly mapped + Directly mapped + Indirectly mapped	37.5 (±1.7)	99.9 (±0.01)	56.3 (±5.5)	99.9 (±0.00)	99.9 (±0.01)
Jointly mapped + Directly mapped + Indirectly mapped + Buffer	6.6 (±0.6)	100.0 (±0.00)	100.0 (±0.0)	99.1 (±0.01)	99.1 (±0.01)

Table 2-4 Accuracy and uncertainty (± margin of error for 95% confidence interval) estimates of the bare ground gain and no gain classes disaggregated by climate domains for different combinations of map features.

Map Feature	Climate domains	User's		Producer's		Overall
		Gain	No gain	Gain	No gain	
Jointly mapped	Tropical	82.4 (±4.7)	99.9 (±0.01)	6.9 (±1.4)	100.0 (±0.00)	99.9 (±0.01)
	Subtropical	88.4 (±4.0)	99.8 (±0.03)	9.6 (±1.7)	100.0 (±0.00)	99.8 (±0.03)
	Temperate	87.6 (±4.1)	99.9 (±0.02)	13.4 (±2.4)	100.0 (±0.00)	99.9 (±0.02)
	Boreal	95.2 (±3.8)	99.9 (±0.01)	15.9 (±5.9)	100.0 (±0.00)	99.9 (±0.01)

	Polar	84.0 (±6.5)	99.9 (±0.01)	2.6 (±2.5)	100.0 (±0.00)	99.9 (±0.01)
Jointly mapped + Directly mapped	Tropical	57.2 (±5.6)	99.9 (±0.01)	45.1 (±8.6)	99.9 (±0.00)	99.9 (±0.01)
	Subtropical	73.3 (±4.7)	99.9 (±0.03)	44.9 (±7.8)	99.9 (±0.00)	99.8 (±0.03)
	Temperate	69.1 (±4.8)	99.9 (±0.02)	52.2 (±8.9)	99.9 (±0.00)	99.9 (±0.02)
	Boreal	66.3 (±7.2)	99.9 (±0.01)	66.8 (±24.2)	99.9 (±0.00)	99.9 (±0.01)
	Polar	28.2 (±7.1)	99.9 (±0.01)	13.7 (±13.2)	100.0 (±0.00)	99.9 (±0.01)
Jointly mapped + Directly mapped + Indirectly mapped	Tropical	34.7 (±3.4)	99.9 (±0.01)	51.2 (±9.6)	99.9 (±0.00)	99.9 (±0.01)
	Subtropical	37.1 (±2.9)	99.9 (±0.03)	53.1 (±9.1)	99.8 (±0.01)	99.7 (±0.03)
	Temperate	38.0 (±3.0)	99.9 (±0.02)	61.0 (±10.2)	99.8 (±0.01)	99.8 (±0.02)
	Boreal	56.6 (±5.9)	100.0 (±0.01)	73.9 (±26.7)	99.9 (±0.00)	99.9 (±0.01)
	Polar	10.1 (±2.9)	99.9 (±0.01)	16.4 (±15.9)	100.0 (±0.00)	99.9 (±0.01)
Jointly mapped + Directly mapped + Indirectly mapped + Buffer	Tropical	6.7 (±1.3)	100.0 (±0.00)	100.0 (±0.0)	99.4 (±0.01)	99.4 (±0.01)
	Subtropical	7.4 (±1.3)	100.0 (±0.00)	100.0 (±0.0)	98.0 (±0.03)	98.1 (±0.03)
	Temperate	6.4 (±1.1)	100.0 (±0.00)	100.0 (±0.0)	98.3 (±0.02)	98.3 (±0.02)
	Boreal	5.7 (±2.1)	100.0 (±0.00)	100.0 (±0.0)	99.6 (±0.01)	99.6 (±0.01)
	Polar	2.8 (±2.6)	100.0 (±0.00)	100.0 (±0.0)	99.6 (±0.01)	99.6 (±0.01)

2.4.2 Bare ground gain area estimates and uncertainties

Global bare ground gain area based on the stratified random sample was estimated to be 93,896±9,317 km^2 (95% confidence interval) during the study period, which is about the area of the country of Portugal or the U.S. state of Indiana. Global bare ground gain area was attributed to six land cover / land use outcomes: 39% commercial-residential built-up, 23% resource extraction, 21% infrastructure development, 11% transitional, 1% greenhouses and 5% natural gain. The subtropical climate domain contained 36% of global bare ground gain area, temperate 35%, tropical 24%, boreal 4% and polar 1%.

The estimated area of global bare ground gain was disaggregated by region and country. Regional estimates of bare ground gain area between 2000 and 2012 and associated uncertainty are shown in Figure 2-9a. Among the seven geographic regions, East Asia and Pacific had nearly half of global bare ground gain area (45%), whereas the land area in this region only accounts for 19% of global land area. North America accounts for about 20% of global bare ground gain area within 14% of global land area. The proportion of bare ground gain area in Europe and Central Asia, Latin America and the Caribbean, South Asia, Sub-Saharan Africa and Middle East and North Africa is 15%, 11%, 4%, 3% and 2%, respectively. This disproportionate distribution is caused by different socioeconomic development rates among regions. Per capita bare ground gain area by region reveals distinct development patterns. For example, per capita bare ground gain area is highest in North America with 54.8 m^2 and lowest in South Asia with 2.3 m^2. The top ten countries with the largest estimates of bare ground gain area

(Figure 2-9b) account for 74% of global bare ground gain area. China experienced the largest increase in bare ground for the study period, accounting for 35% of global bare ground gain; the U.S. was second with a share of 17%. China and the U.S. differed most markedly in their respective investment in infrastructure (Figure 2-9b). Bare ground gain from infrastructure development totaled 11,063±4,073 km^2 and 2,268±1,425 km^2, for China and the U.S., respectively (the ± values represent the 95% confidence interval).

Proportional compositions of attributed bare ground gain drivers also vary between regions and countries (Figure 2-10). The East Asia and Pacific region has the largest total area of bare ground gain from resource extraction due to extensive mining in China and Australia, whereas Sub-Saharan Africa has the highest proportion of bare ground gain due to resource extraction. Commercial/residential built-up and infrastructure development in East Asia and Pacific are largely related to China and its rapid urbanization rate during the study period. North America and the Middle East and North Africa also exhibit high shares of commercial/residential built-up. Much of the Middle East's growth is found in the oil rich Gulf States. South Asia has the greatest share of natural bare ground gain, mainly due to river meanders within Himalayan watersheds.

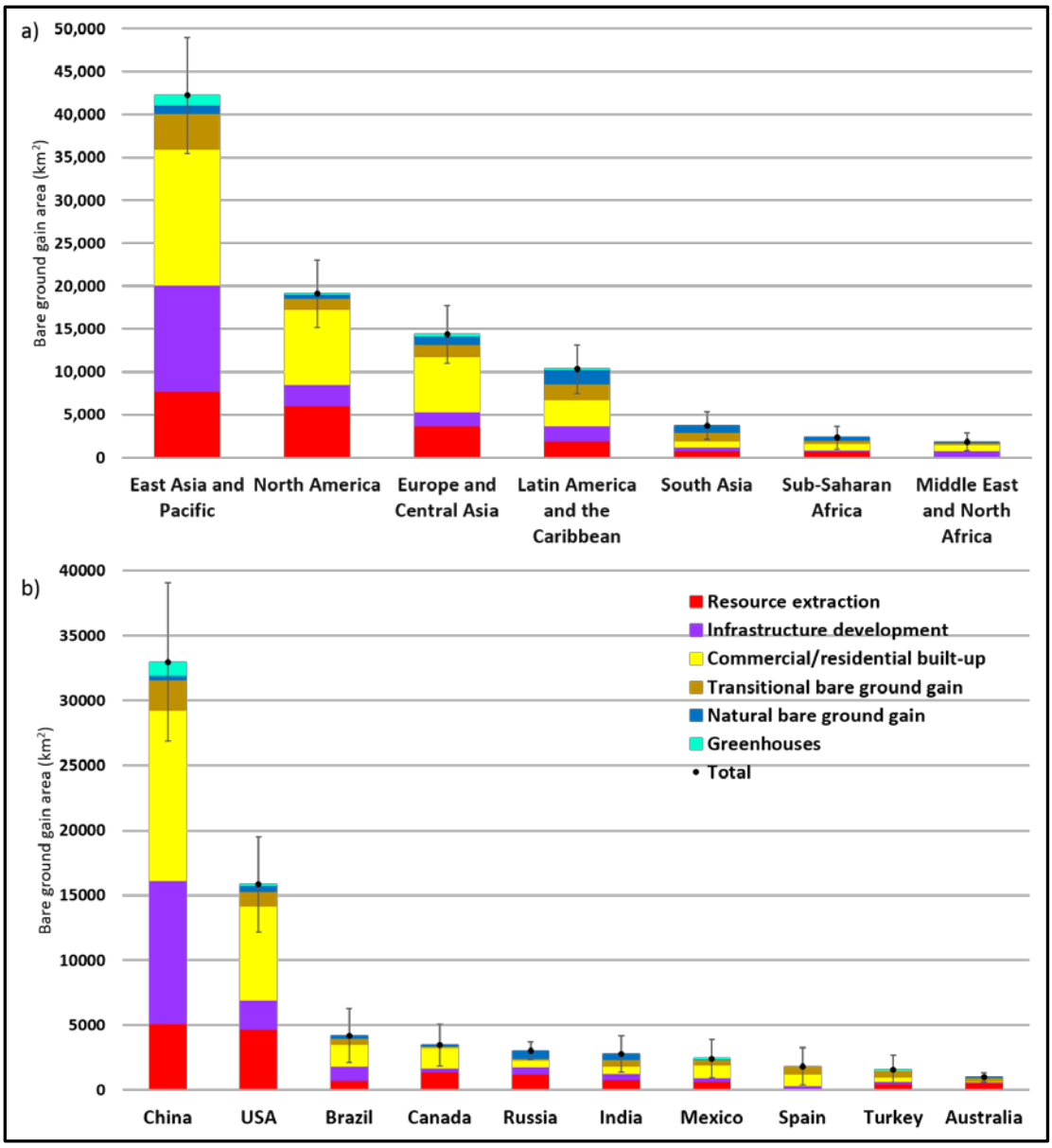

Figure 2-9 Bare ground gain area estimates for 2000-2012 (95% confidence intervals represented by error bars) and composition of land cover/land use outcomes of bare ground gain: a) regional estimates; b) estimates of top ten countries with the largest directly mapped bare ground gain area.

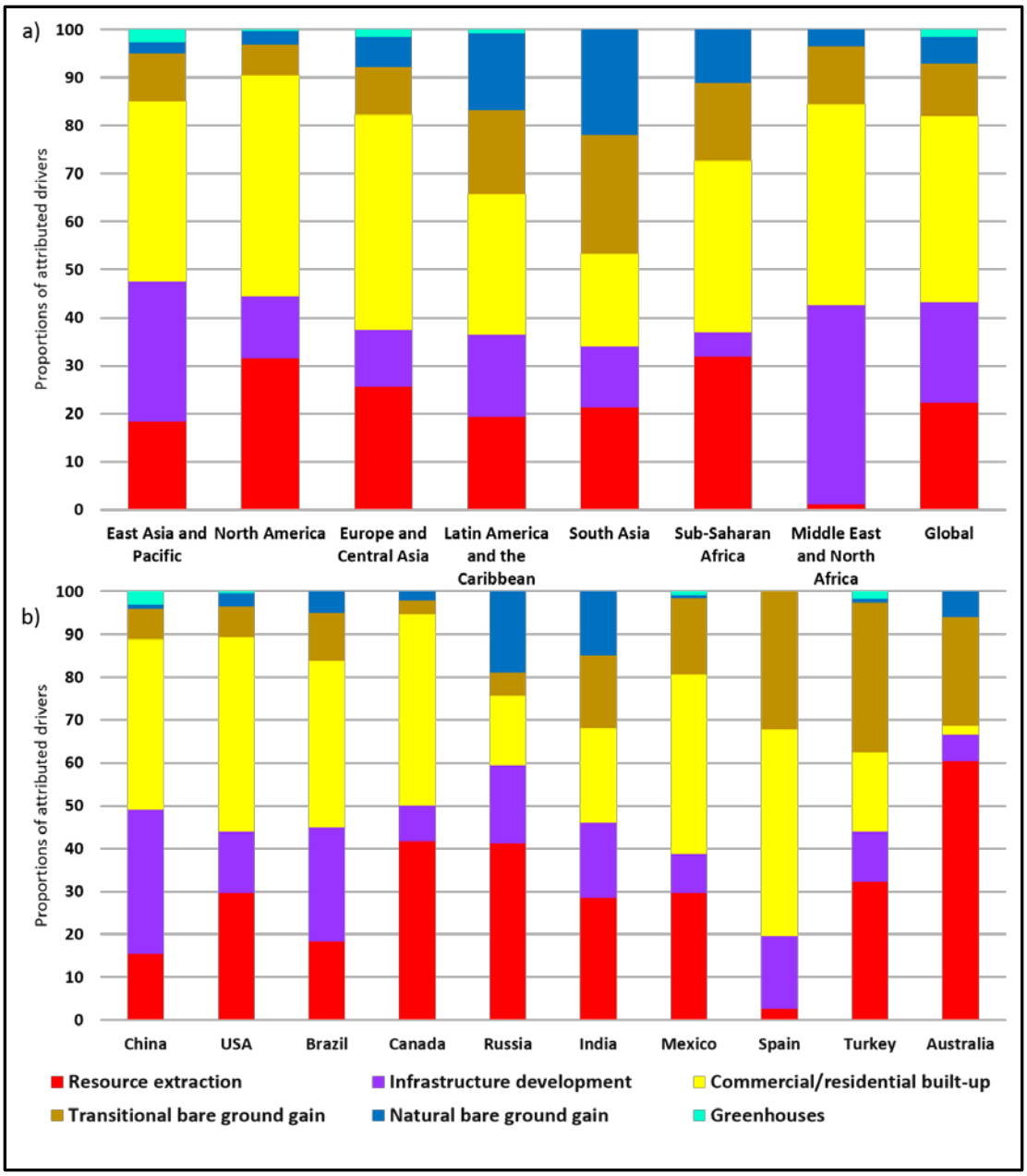

Figure 2-10 Proportions of estimated bare ground gain area to land cover/land use outcomes: a) by region and b) by country.

2.5 Discussion and conclusion

Our research delivers the first estimates and uncertainties of global bare ground gain area using Landsat imagery. Bare ground gain represents a very small fraction of the overall global land cover and land use extent and change, making it a difficult theme to quantify. To illustrate this idea and the resulting challenge to area estimation, we can reference tree cover loss for comparison. Tree cover of >25% canopy and 5m tall trees covers nearly 30% of the global land surface (M C Hansen et al., 2013). Tree cover change as mapped by Landsat occurs within 0.13% of global land area annually (M C Hansen et al., 2013). It is obvious that in order to establish precise rates of tree cover change, an accurate stratification is required to target this comparatively rare annual dynamic. For bare ground, the challenge is even greater. For example, urban areas account for < 1% of global land area (Schneider et al., 2010) and their growth over time is vanishingly small compared to tree cover. To accurately estimate the extent of this land dynamic, a mapping capability is required to successfully target this rare land dynamic, something enabled by Landsat data.

Compared to a previous study of Landsat-derived bare ground gain for the continental U.S. (Hansen et al., 2014), mapped bare ground gain of our global study had a relatively higher user's accuracy (67% compared to 42% for the previous continental study) and comparable producer's accuracy (48% compared to 49% for the previous study) even though our study was implemented at a larger scale (global vs country level). For both of these studies, the maps proved inadequate when a "pixel counting" approach to calculating area of bare ground gain was used. However, the use of the map as an indicator of landscapes experiencing bare ground gain facilitated

unbiased sample-based area estimates of bare ground gain. We calculated the gain in precision of the bare ground gain area estimates attributable to the stratified sampling design (Cochran, 1977, section 5A.11) as quantified by the ratio of the standard error expected under simple random sampling to the standard error of stratified random sampling design implemented in our study (both designs have the same sample size). The larger the ratio of standard errors the greater the benefit of the stratification by mapping bare ground gains. The calculation of the standard error ratios in our study is based on the estimated proportion of bare ground gain in each of the 25 strata (combinations of climate domain and map feature class) as these proportions determine the standard deviation for each stratum. Because we found no bare ground gain in the "mapped no gain" strata, we assumed that these strata had 0.01% of bare ground gain because otherwise these five "no gain" strata would have contributed no variance to the overall area estimate. The standard error ratios were 11.5 globally, 14.0 for the tropical domain, 8.7 for subtropical, 9.8 for temperate, 7.7 for boreal, and 12.7 for polar domain. In other words, over eleven times the number of sample pixels selected using the Landsat stratification would have been needed to produce a global bare ground gain estimate with a similar uncertainty using simple random sampling. The sampling approach also enabled the assignment of contextual attributes (e.g. land cover / land use outcomes of bare ground gain) per sample pixel, enriching the overall land cover and land use change narrative. Tyukavina et al. (2015) performed a similar analysis in assigning natural versus managed forest cover loss to samples of pan-tropical forest disturbance. Sample interpretation enables obtaining considerable thematic value-added information not captured by the map.

The preferred outcome and long-term objective is to produce land cover change maps that are highly accurate. In this study, the directly classified map outperformed the post-characterization map in terms of accuracy of the bare ground gain class (67% vs 20% for user's and 48% vs 18% for producer's), suggesting that our bare ground gain classification approach has the potential to produce more accurate characterization of land change. Mapping bare ground gain indirectly using the percent bare ground cover time series proved less reliable. Serra et al. (2003) and Olofsson et al. (2013) have demonstrated that post-characterization approaches have limitations in characterizing land cover change. To improve the mapping performance of both approaches, a more sophisticated feature space is needed as well as additional training data focused on regions that performed poorly in terms of map accuracy in this study.

The approach of estimating area from a sample based on visually interpreted bare ground gain offers a cost-effective alternative free of the bias attributable to classification map error. The primary limitation of the sampling approach is that it is far less effective at providing a spatially explicit representation of bare ground gain. While each pixel can be assigned the mean gain of its associated stratum, this would not likely result in a map that was effective for reporting sub-regional area estimates. Consequently, larger sample sizes and possibly more regional/national strata would be required to produce more spatially disaggregated area estimates with adequate precision. The effort to manually interpret a very large sample is the main limitation of sample-based land change estimation when a large area with many sub-regions is of interest.

A larger sample would also better inform possible limitations to the overall method. For example, it could be expected that bare ground gain in semi-arid and arid environments with considerable antecedent fractional bare ground cover might exhibit higher omission error rates. While bare ground gain in arid regions such as urbanization in Dubai, UAE, and semi-arid regions such as mining in Wyoming, USA, were mapped, there may be other dynamics omitted. However, we did not find this to be the case as we did not have any commission errors within sample pixels of our no change strata. A larger sample might have revealed such limitations.

The themes measured by bare ground gain represent investment in energy, housing, and transportation, among other activities. As such, bare ground gain could be used as a possible indicator of economic activity. However, there are many challenges associated with this possibility and further investigation would be required to establish credibility. For example, energy extraction is not uniform in footprint and may even occur offshore. Patterns of urbanization are similarly not uniform in space with factors including planning and zoning, settlement population density, and geographic constraints such as water bodies and terrain that can alter area of change for a given investment. Infrastructure investments are similarly not equally manifested on the land surface. The test of the utility of such an approach will be to relate it to existing economic data despite these mapping caveats.

Results indicate global and regional bare ground gain for areas experiencing rapid economic and demographic change. Seto et al. (2012) recognized urban population and Gross Domestic Product (GDP) as key determinants of urban expansion and developed a model to forecast global urban expansion to 2030. Our results support this narrative

except for Africa and South Asia, two regions with rapid population growth, but comparatively little documented bare ground gain. Among the top ten countries with the largest bare ground gain estimates, China had a similar GDP growth rate with the U.S. before 2007. China also had the highest rate of urban population growth. India, on the other hand, had high urban population increase, but much slower GDP growth (World Bank, 2016b). This indicates the complex relationships of urban population and GDP change on human-induced bare ground gain. In-depth investigation of bare ground gain area and analysis of socioeconomic drivers on regional and country scales is important for scientists, planners and policy makers to understand the drivers and resultant rates of this most intensive of land cover conversions.

Chapter 3 Satellite-detected gain in built-up area as a leading economic indicator[2]

3.1 Abstract

Leading indicators of future economic activity include measures such as new housing starts, managers purchasing index, money supply, and bond yields. Such macroeconomic and financial indicators hold predictive power in signaling recessionary periods. However, many indicators are constrained by the fact that data are often published with some delay and are subject to constant revision (Bandholz and Funke, 2003; Huang et al., 2018; Orphanides, 2003). In this research, we propose a leading indicator derived from satellite imagery, the expansion of anthropogenic bare ground. Satellite-detected gain in built-up area, a major land cover and land use (LCLU) outcome of anthropogenic bare ground gain (ABGG), provides an inexpensive, consistent, and near-real-time indicator of global and regional macroeconomic change. Our panel data analysis across four major regions of the world from 2001 to 2012 shows that the logarithm of total ABGG, mostly owing to its major LCLU outcome, the expansion of built-up land in either year *t*, *t* -1 or *t* -2, significantly correlated with the year *t* logarithm of Gross Domestic Product (GDP, de-trended by Hodrick-Prescott Filter). Global ABGG between 2001 and 2012 averaged 7,875 km^2y^{-1}, with a peak gain of 11,875 (± 2014 km^2 at the 95% confidence interval (CI)) in 2006,

[2] The presented material was previously published in Ying, Q., Hansen, M.C., Sun, L., Wang, L., Steininger, M., 2019. Satellite-detected gain in built-up area as a leading economic indicator. Environ. Res. Lett. 14, 114015.

prior to the 2007-2008 global financial crisis. The curve of global ABGG or its major LCLU outcome of built-up area in year *t* - 1 accords well with that of the de-trended logarithm of the global GDP in year *t*. Given the 40-year archive of free satellite data, a growing satellite constellation, advances in machine learning, and scalable methods, this study suggests that analyses of ABGG as a whole or its LCLU outcomes can provide valuable information in near-real time for socioeconomic research, development planning, and economic forecasting.

3.2 Introduction

The 2007-2008 global financial crisis is considered the worst since the Great Depression of the 1930s and had dramatic impacts on global and regional economies and societies. Economists and policy makers seek indicators of overall economic health to help diagnose and forecast expected performance, with a goal to mitigate against volatility and to avoid shocks such as the crisis of 2007-2008. However, such efforts are limited as macroeconomic and financial variables are often reported with delays and constantly revised (Bandholz and Funke, 2003; Huang et al., 2018; Orphanides, 2003). Recently, new data resources from satellite images (Bennett and Smith, 2017; Jean et al., 2016), cellphone metadata (Blumenstock et al., 2015) and social media (Li et al., 2013; Liu et al., 2015) have emerged as indicators of economic activity. For example, proposed proxies for GDP, such as lit area (Elvidge et al., 1997) and luminosity (Chen and Nordhaus, 2011), have been derived from satellite data on nighttime light (Henderson et al., 2012). However, the ability of new big data sources to predict changes in economic outcomes at global or regional scale is a work in

progress. Based on the presented research, we propose a leading indicator derived from freely available satellite imagery: the expansion of built-up area, a major LCLU outcome of anthropogenic bare ground gain.

Anthropogenic bare ground gain is a dynamic of land-cover and land-use change (LCLUC) that principally results from economic activities. Estimates of anthropogenic bare ground gain, based on the characterization of publicly available satellite imagery, can potentially serve as a low-cost, near-real time source for proxies of economic change from national to global scales. We define bare ground gain as a process of land-cover change featuring the removal and continued absence of vegetative cover for at least three years by either human or natural disturbances (Ying et al., 2017). In our previous research (Ying et al., 2017), globally and for each of seven regions over the 2001-2012 period, we partitioned bare ground gain into six components, defined by their LCLU outcomes: resource extraction; infrastructure development; commercial/residential built-up area; transitional bare ground gain, defined as new bare ground gain that had not yet been clearly put to some use; greenhouses; and one component for all natural gain (see (Ying et al., 2017) for detailed explanation). The five components of anthropogenic bare ground gain accounted for 95% of total bare ground gain over the study period. Examples of anthropogenic bare ground gain include expansion of urban areas, construction of new roads, mining, installation of oil wells, among other dynamics.

For the present study we estimated temporal trends of bare ground gain and its LCLU outcomes at the global scale (Figure 3-1a) and for seven regions (Figure 3-1b-e, Figure 3-7) where time series of economic indicators are aggregated by the World Bank,

including East Asia and the Pacific, North America, Europe and Central Asia, Latin America and the Caribbean, South Asia, Sub-Saharan Africa, and Middle East and North Africa. We conducted panel data analysis of the four regions that account for over 90% of anthropogenic bare ground gain and have relatively low uncertainties: East Asia and the Pacific, North America, Europe and Central Asia, Latin America and the Caribbean. This analysis shows that the logarithm of anthropogenic bare ground gain in either year *t*, *t* -1 or *t* - 2 is significantly correlated to the de-trended (by Hodrick-Prescott Filter) logarithm of GDP in year *t*, whereas such gains in year *t* or *t*-1 are significantly correlated to the de-trended logarithms of merchandise imports and exports, or energy consumption in year *t*. Globally, the annual anthropogenic bare ground gain between 2001 and 2012 was 7,875 km^2 on average with a peak gain of 11,875 (± 2014 km^2 for 95% CI) occurred in 2006 prior to the 2007-2008 global financial crisis. The curve of global anthropogenic bare ground gain in year *t* - 1 accords well with that of the de-trended logarithm of the global GDP in year *t*. This predictive attribute of remotely sensed anthropogenic bare ground gain makes it an important LCLUC theme that can effectively support socioeconomic analysts and policy makers to develop financial plans and to allocate resources towards stable growth.

3.2 Method and data

3.2.1 Estimation of annual bare ground gain and attribution of LCLU outcomes

Unbiased estimates of areas of annual bare ground gain were produced from a set of probability-based samples (Ying et al., 2017). Specifically, global land area was

stratified by a set of global seamless bare ground gain layers that were produced through automatic classification methods using Landsat 7 Enhanced Thematic Mapper Plus (ETM+) growing season composites between 2000 and 2012. Global annual composites were produced from 654,178 growing season Landsat scenes with per pixel detection of cloud, shadow, snow/ice, water or qualified observation (M C Hansen et al., 2013). Ying et al. (2017) calculated multi-temporal metrics out of the time series of annual composites that were then used to build tree models for classification of bare ground gain. Due to errors inherent with the produced layers of bare ground gain, we did not calculate the areas of bare ground gain from counting the pixels of labelled gain by classification models to avoid biased report of areas of bare ground gain. Instead, we employed those layers as a stratifier to help us efficiently distribute a set of sample for unbiased area estimation in bare ground gain. A total of 5, 750 sample pixels were selected globally in a stratified random design (25 strata) and then interpreted whether bare ground gain occurred or not (1635 gain pixels vs 4115 no-gain pixels) with time-series of Landsat images, 32-day Normalized Difference Vegetation Index (NDVI) time sequences from Google Earth Engine (Gorelick et al., 2017) and high-resolution images on Google Earth (Figure 3-5). For gain sample points, we decided the change year when NDVI dropped by over 50% and kept low for at least three years following our definition of bare ground gain. We attributed the LCLU outcomes of gain samples through combined information given by the characteristics of spectrum and configuration of Landsat and high-resolution images and even local photos from Google Earth. Recording the change year and attributing the LCLU outcomes of sample pixels that were labeled as

bare ground gain enabled us to estimate annual change areas and disaggregate all changes to six components of direct bare ground gain drivers including resource extraction, infrastructure development, commercial/residential built-up area, transitional bare gain, greenhouses and natural bare ground gain (Tyukavina et al., 2018; Ying et al., 2017; Zalles et al., 2019). We estimated the bare ground gain area attributable to the LCLU outcome i in year t in stratum h:

$$\hat{G}_{i,t,h} = A_h p_{i,t,h} \quad (1)$$

where A_h is the total area in stratum h, $p_{i,t,h} = n'_{i,t,h}/n_h$ is the sample proportion of pixels interpreted as bare ground gain of LCLU outcome i in year t in stratum h, $n'_{i,t,h}$ is the number of sample pixels interpreted as bare ground gain of LCLU outcome i in year t, and n_h is the number of sample pixels allocated to stratum h. Then the bare ground gain area of LCLU outcome i in year t is obtained by summing the area estimates over all strata:

$$\hat{G}_{i,t} = \sum_{h=1}^{25} \hat{G}_{i,t,h} \quad (2)$$

Area estimates and uncertainty quantification of bare ground gain were performed at global and regional level. To reduce the variation of annual bare ground gain estimates from interpretation bias of change year due to noise and missing data in NDVI time sequences and historic high-resolution images, sample counts of the average of year t and 1-year neighbors (t-1 and t+1). Land cover change maps derived from remote sensed imagery are subject to omission and commission errors (Olofsson et al., 2014). However, probability-base samples using maps as strata to target specific LCLU dynamics yield unbiased estimates of change areas (Stehman,

2013). The approach of utilizing classified land cover change maps to target sampling of a rare class of interest compared to the overall land surface, in this case bare ground gain, raised the sampling efficiency by eleven times and greatly reduced the standard error in our change estimates (Ying et al., 2017).

Producing highly accurate maps of bare ground gain is the key to increase sampling efficiency and reduce estimation uncertainty. For a historical data set, we employed the definition of three-year absence of vegetation in remote sensing classification of bare ground gain to eliminate commission errors from agricultural fallow being falsely classified as bare ground gain. Though the annual composite used for detection of bare ground gain was selected from growing season Landsat images, it is possible that for a consecutive three year, reflectance of pre-planting agricultural clear was selected for a pixel due to limited observations in some areas. To better serve as a leading indicator in near-real time, a number of enhancements are possible, including the use of monthly satellite observations of bare ground in place of the annual measure employed here, and land use maps to track ephemeral bare ground gain associated with established land uses such as agriculture and forestry.

3.2.2 Growing trends and business cycles of selected economic variables

Economic development is depicted by economic, trade and energy measures considered relating to anthropogenic bare ground gain. The World Bank is one of the leading groups for collecting and analyzing data of global economies at global, regional and national level. Indicators including GDP, merchandise imports and exports, energy use and production (Table 3-4) were downloaded from the World

Bank database at global and regional level from 2000 to 2012 ("World Bank Open Data | Data," n.d.). Annual statistics were recorded for 211 countries and regions, and then aggregated to seven regions grouped by geographic locations identified by the World Bank. We converted values of GDP, merchandise imports and exports, which were measured in current U.S. dollars in original data, to constant U.S. dollars in 2010 by adjusting for inflation.

The Hodrick-Prescott (HP) Filter (Hodrick and Prescott, 1997) in the R statistical package (Balcilar, 2015) was employed to perform economic growth-business cycle decomposition for time series of the five economic variables. The HP filter is arguably the most commonly used mathematical tool in macroeconomics, especially in real business cycle theory, to separate the time-trend from cyclical component of a time series data (Hodrick and Prescott, 1997; Williamson, 2002). It is composed of two components (Figure 3-9). One controls the fitted trend close to the time series, which is measured by the residuals. The other one controls the smoothness of the trend that is measured by the second derivative of the trend. A parameter λ weighs the two components to control the trend between linear and the original time series. The set of λ value depends on data frequency. An optimal trend is the one that gives the minimum sum of the two components. We took natural logarithms of time series variables, removed the trend component, and derived the cyclical component using a λ of 100 for annual data (Backus and Kehoe, 1992).

3.2.3 Panel data analysis of bare ground gain dynamics and economic fluctuations

Panel data analysis (Flanagan et al., 2006) was used in a fixed effect mode to examine the correlation between the cyclical components of each economic variable and the natural logarithms of different combinations of LCLU outcomes of bare ground gain when detangling the unobservable time-invariant heterogeneity associated with each region. The fixed effect model, taking GDP as an example, is

$$\ln GDP_{rt} = a_r + b * \ln BGG_{r,t-\tau} + \varepsilon_{rt}, \quad \tau = -1, 0, 1, 2. \tag{3}$$

where subscripts *r* and *t* denote region and year. In the model, a_r represents the characteristics such as resource endowments, laws and regulatory regimes, or culture that are unique to each region, not change much in a short period of about one decade, but correlated with the predictor variable. The fixed effect model controls for the effect of these characteristics to assess the net effect of changes in bare ground gain areas on the variation in economic variables. We used R "plm" package for estimation (Croissant and Millo, 2008) and performed Hausman test to justify the selection of the fixed effect model.

We only used data in regions of East Asia and the Pacific, Europe and Central Asia, Latin America and the Caribbean and North America for their relatively low uncertainty of annual bare ground gain estimates. As our baseline year is 2000, the full-time frame of bare ground gain estimates is from 2001 to 2012.

Because our definition of bare ground gain requires an absence of vegetation for continuously three years, edge effects may have influenced in our estimates for the last two years, which could cause underestimation of bare ground gain areas in 2011 and 2012. We tested regression models for both full (2001-2012, Table 3-1, 3-5) and

cut-edge (2001-2010, Table 3-6) time series. There was no significant difference in drawing the conclusion. Both results suggested the one-year leading characteristic of anthropogenic bare ground gain to economic variables. Nevertheless, the temporal trends were not hindered by the edge effect as the major changes occurred between 2003 and 2010.

3.3 Results

3.3.1 Global distributions, trends and compositions of bare ground gain

A probability-based, stratified-random sample (Figure 3-6) was selected from mapped bare ground strata from 2000 to 2012. Each sample was visually interpreted using reference imagery, specifically Landsat Enhanced Thematic Mapper Plus (ETM+) imagery with a moderate spatial resolution (~30m) and commercial imagery with very high spatial resolution freely viewable on Google Earth. Each sample location of bare ground gain was assigned to a type of LCLU outcome and to a year of initial vegetation removal (Figure 3-5).

From 2000 to 2012, global bare ground gain averaged 7881 km^2y^{-1}. That is, every year a land area close to the size of the Yellowstone national park semi/permanently lost its vegetation cover. About half of this average rate, 3550 km^2y^{-1}, was in the East Asia and the Pacific region, and the smallest portion, 154 km^2y^{-1}, was in the Middle East and North Africa. The temporal trend of total bare ground gain globally is unimodal (Figure 3-1a), as are those for all regions (Figure 3-1b-e, Figure 3-7), with peaks from 2006 to 2008, except Sub-Saharan Africa which is bimodal. Global year on year bare ground gain increased from 3,118 ± 1,132 km^2 in 2001 to a peak of 11,878 ±

2,014 km^2 in 2006 with a growth rate of 31% per year on average and fell by 60% of the peak to 4,772 ± 1,673 km^2 in 2012. Total bare ground gain in East Asia and the Pacific increased fivefold from 2001-2004, and then slowed between 2005 and 2008. Latin America and the Caribbean was unique in its recovery of a positive trend in bare ground gain after 2010.

The greatest LCLU outcome of bare ground gain in most regions was commercial/residential built-up area (49% in North America, 44% in East Asia and the Pacific, 29% in Latin America and the Caribbean), followed by resource extraction (North America 32%, Europe and Central Asia 26%, Latin America and the Caribbean 23%). East Asia and the Pacific differed, where infrastructure was the largest (39%), followed by commercial/residential built-up area (34%). Different LCLU outcomes of bare ground gain, however, showed different patterns of peak time and change rate (Figure 3-1, Figure 3-8). The trends in the expansion of commercial/residential built-up area varied among the four regions in the years following their 2006 peaks (Figure 3-8). For example, those in North America and Europe and Central Asia gradually declined, that in East Asia and the Pacific temporarily stabilized in 2007 through 2010 and then resumed its decline, and that in Latin America and the Caribbean appeared to begin to recover beginning in 2010 (Figure 3-8). New infrastructure development generally peaked in 2008-2010. A shorter cycle of transitional bare ground gain appeared in each region following the decline of commercial/residential built-up area. Growth in resource extraction resumed about two years after the peak in each region except East Asia and the Pacific and was the source of the recovery in overall bare ground gain in Latin America and the Caribbean.

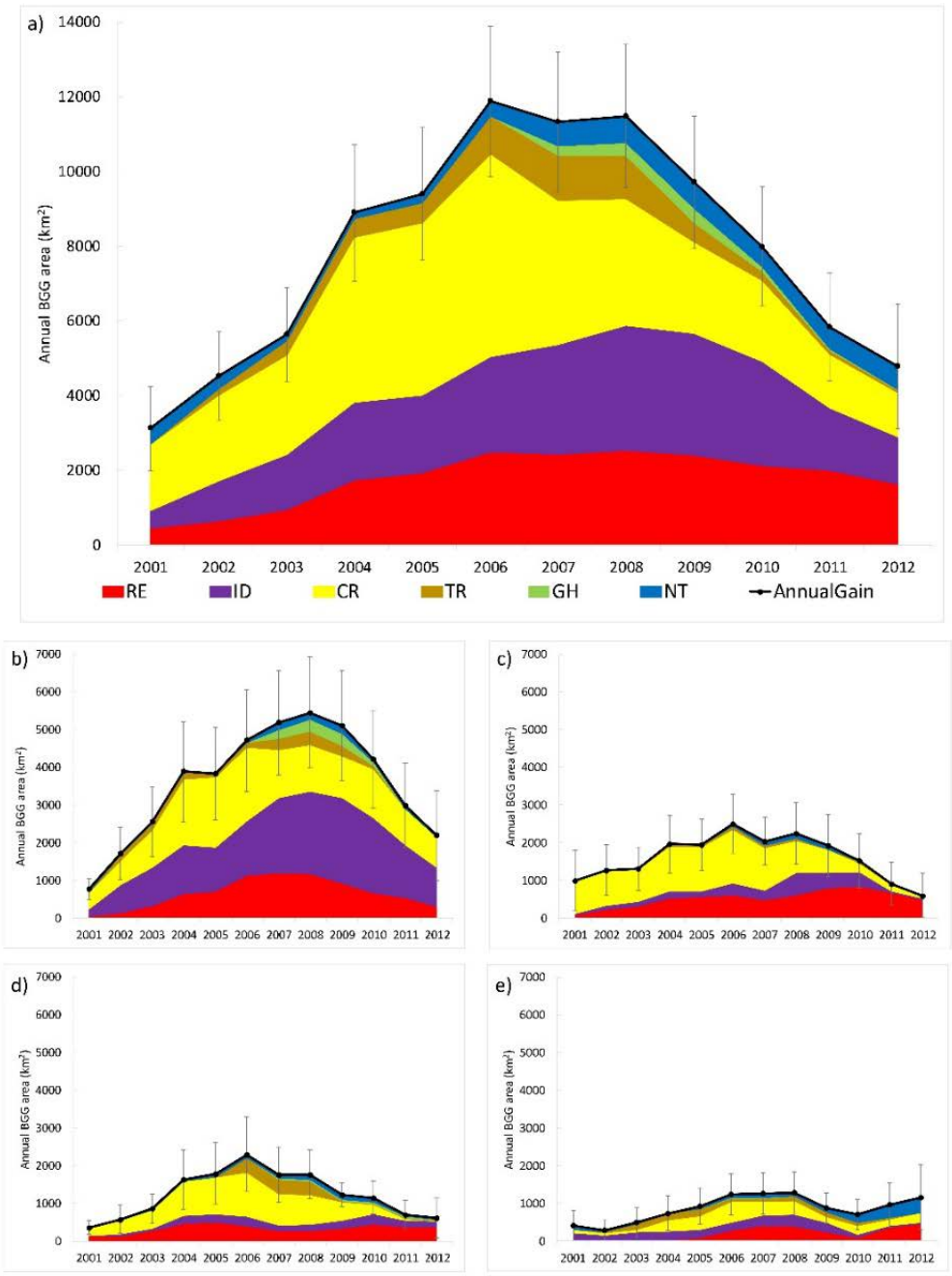

Figure 3-1 Annual estimates of total area (95% CI represented by error bars) and composition of LCLU outcomes of bare ground gain from 2000 to 2012 for a) global and four regions b) East Asia and Pacific, c) North America, d) Europe and Central Asia, and e) Latin American and the Caribbean, separately. RE: resource extraction, ID: infrastructure development, CR: commercial/residential built-up area, TR: transitional gain, NT: natural gain, GH: greenhouses, and thereafter.

3.3.2 Gain in built-up area foreshadowed the Great Recession

The cyclic patterns of global anthropogenic bare ground gain foreshadowed the decade's macroeconomic fluctuations dominated by the 2007-2008 global financial crisis. The rise in anthropogenic bare ground gain, driven mainly by commercial/residential built-up area, transitioned to a decline prior to the 2008 crash (Figure 3-3a). Furthermore, inter-annual anthropogenic bare ground gain and commercial/residential built-up area were both significantly correlated to the de-trended global GDP (Figure 3-3b, c).

To explore how these patterns were related to the economic activities during this study period, we carried out panel data regressions of fluctuations on individual economic variables versus different combinations of LCLU outcomes of anthropogenic bare ground gain, and their leading or lagging terms. GDP was used in the analysis because among the four components of expenditure, investment is most related with infrastructure development and commercial/residential built-up area, whereas consumption and net exports are more associated with all LCLU outcomes of anthropogenic bare ground gain. Merchandise exports and imports were included to further account for domestic land use and displacement (Lambin and Meyfroidt, 2011; Yu et al., 2013). Energy use and production partly accounted for fossil fuel extraction, one major component of bare ground gain from resource extraction. Merchandise imports and exports, and energy use are significantly correlated with GDP (Figure 3-11).

Panel analysis indicates that trends in regional, anthropogenic bare ground gain are significant leading indicators, by one year, of the tested economic variables, especially

GDP (Table 3-1, 3-5, Figure 3-4). Alternating the lag length of bare ground gains, panel regressions show that commercial/residential built-up area leads GDP by one year or two years at the highly significant levels (Figure 3-4). Comparing different compositions of LCLU outcomes of anthropogenic bare ground gain, panel regressions show that commercial/residential built-up area leading GDP yield the highest r^2 values (Figure 3-4). A 10% increase in anthropogenic bare ground gain in an antecedent year is associated with a growth in the following year of 0.6% (±0.2%) for GDP, 1% (±0.3%) for merchandise imports, and 0.9% (±0.3%) for merchandise exports (Table 3-1). For one-year lagged terms (*t*-1), total anthropogenic bare ground gain, as well as gains in commercial/residential built-up area, alone or combined with those in infrastructure development and transitional land, are all significantly correlated with GDP, merchandise imports and exports, and energy use (Table 3-1), showing a predictive capability in economic changes. Compared to resource extraction and infrastructure development, one-year lagged term of commercial/residential built-up area outperforms the coincident term with an increase in r^2 of 0.21 (Table 3-1, 3-5).

Leading indicators performed differently among different regions. For example, commercial/residential built-up area peaked in 2006 in Europe and Central Asia and Latin America and the Caribbean (Figure 3-1d-e, 3-8), two years earlier than the GDP peak in these regions (Figure 3-10). Also, the magnitude of changes in anthropogenic bare ground gain was modest compared to the magnitude of GDP changes. For example, the decrease of newly commercial/residential built-up area in 2008 was weak compared to the plunge in the GDP of Europe and Central Asia in 2009 (Figure 3-12).

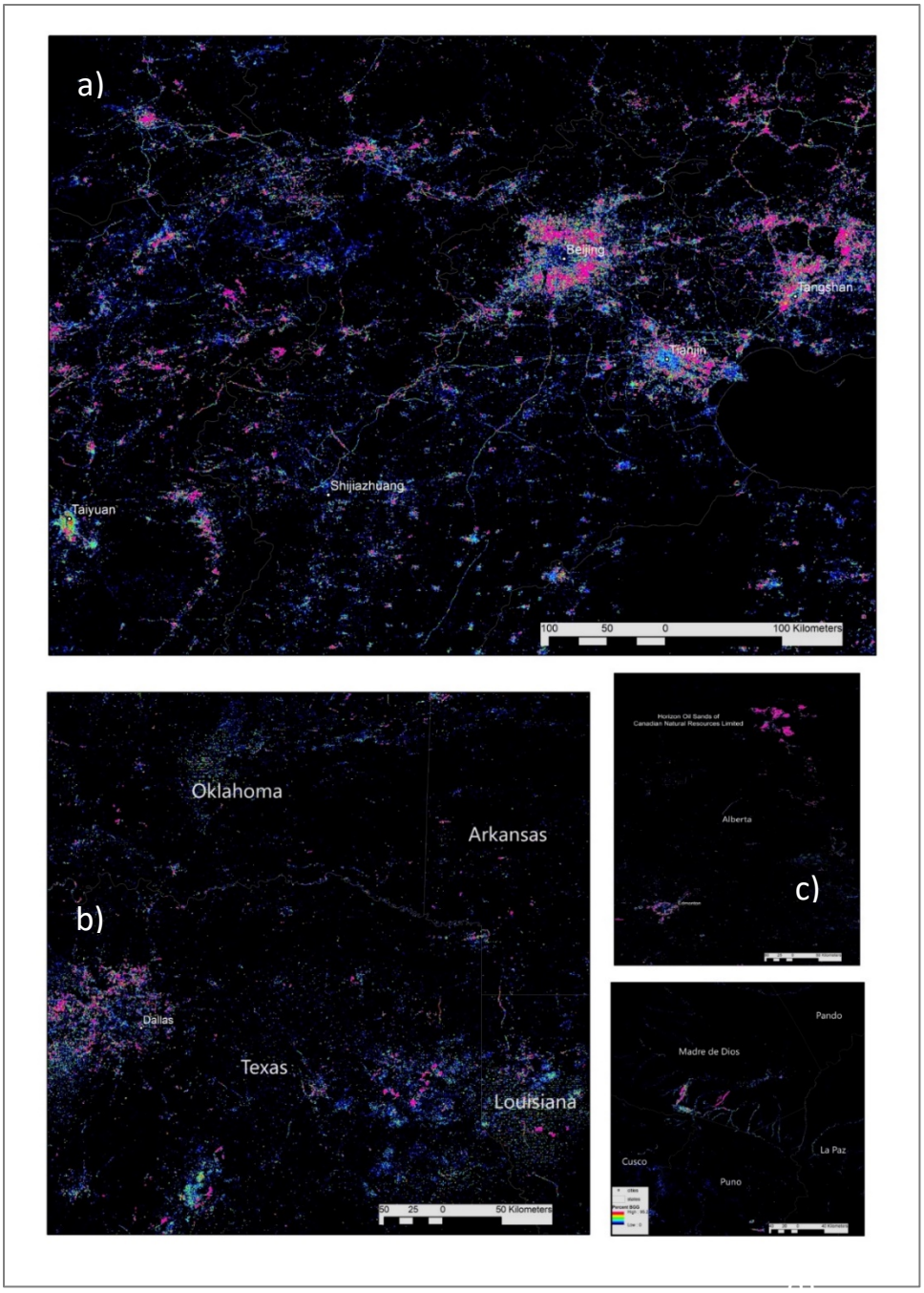

Figure 3-2 Percent bare ground gain aggregated at ~500m spatial resolution from a satellite-based strata at 30m per pixel resolution: a) Urban expansion in Beijing, Tianjin, Tangshan and Taiyuan and transportation development in northern China; b) Urban sprawl in Dallas, Texas and exploration spread for crude oil and natural gas in Texas-Louisiana Salt Basin and Arkoma basin ranging from Oklahoma to Arkansas, U.S.A; c) Oil drilling in Alberta and open pit for sand oil in Fort McMurray, Canada; d) Gold mining in Peruvian Amazon.

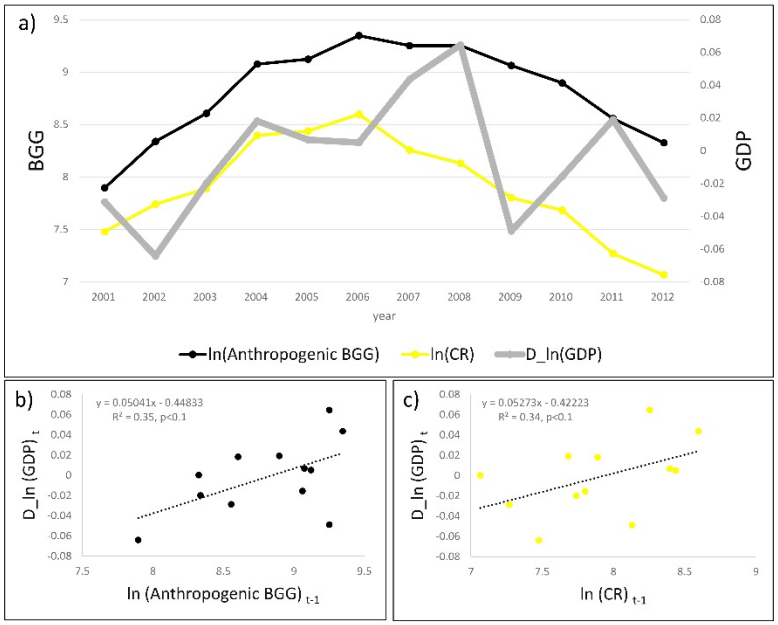

Figure 3-3 Global anthropogenic bare ground gain and expansion of commercial/residential built-up area foreshadowed the cyclic pattern of GDP fluctuations by two years. The inter-annual bare ground gain and commercial/residential built-up area in year t-*1 were both significantly ($p < 0.1$) correlated to the de-trended global GDP in year* t*: a) Trends of the natural logarithms of anthropogenic bare ground gain and commercial/residential built-up area, and the fluctuations of global GDP (de-trended natural logarithms of GDP); b) Linear regression of de-trended GDP on one-year lagged anthropogenic bare ground gain; c) Linear regression of de-trended GDP on one-year lagged commercial/residential built-up area.*

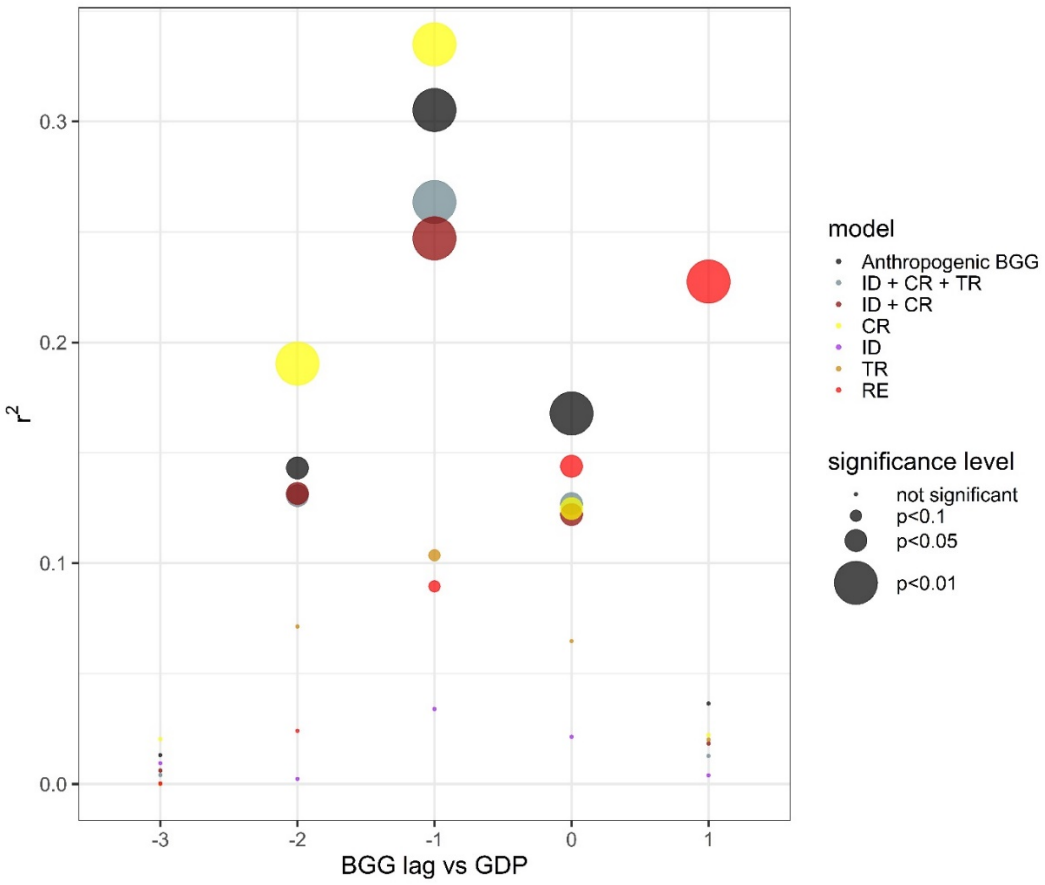

Figure 3-4 Comparison of r^2 (y axis) and significance (point size) between fixed effect regression models of GDP on the sequences of different time lags (x axis, -1 means ABGG in year t *– 1 and GDP in year* t*, 1 means ABGG in year t + 1 and GDP in year* t*) in different compositions of LCLU outcomes of ABGG (point color). Commercial/residential built-up area (CR), ABGG, the sum of infrastructure development, commercial/residential built-up area and transitional bare ground gain (ID + CR + TR), and the sum of infrastructure development and commercial/residential built-up area (ID + CR) led GDP by one year and two years with the significant level above 5%. The two-year lead of CR has an r^2 of 0.18 and the one-year lead of CR has an r^2 of 0.33.*

3.4 Discussion

3.4.1 Link between gain in built-up area and regional economic activities

As with the global trend, anthropogenic bare ground gain and gains from commercial/residential built-up area in North America and Europe and Central Asia, where the economies were first hit by the subprime mortgage crisis in 2007 and substantial European debt crisis, all peaked in 2006, earlier than these financial crises. According to the Standard & Poor/Case-Shiller Composite Home Price Index, a measure of the aggregate market for single family homes in 10 U.S. major cities, the real estate market entered a price boom in late 1990s, and abruptly turned down after mid-2006 (Shiller, 2008). Commercial/residential built-up area is closely related to the housing market, thus the trends in this component of anthropogenic bare ground gain mirrored the market, immediately suggesting a downturn in investment in real estate, which is further reflected in macroeconomic accounts.

The temporal dynamics of commercial/residential built-up area, infrastructure development and transitional bare ground gain were inherently coupled over our study period. For example, the peak in infrastructure gain lagged that of commercial/residential built-up area by two years. This suggests that flexible housing markets are more sensitive to economic changes than infrastructure projects are, the latter typically requiring more planning and equipment (Mok et al., 2015). Gain in transitional land peaked between 2006 and 2008, likely a reflection of ceased construction and other projects during the onset of the financial crisis. Decreases in

every LCLU outcome of anthropogenic bare ground gain occurred after 2008 when the financial crisis triggered wide impacts on all major sectors of economies.

East Asia and the Pacific accounted for 45% of global bare ground gain, 78% of which was in China. China has experienced an excessive rural-urban migration since the economic reform. The urbanization rate increased from 36% in 2000 to 52% in 2012, while the average urban household income grew fourfold (The World Bank, n.d.). To accommodate massive urban in-migration, China carried out urban housing reform, pushing the provision of urban housing from a welfare to market-oriented system (Chen et al., 2011). The demographic, economic and institutional changes resulted in an average gain of 976 km^2y^{-1} in commercial/residential built-up area (Figure 3-2a and yellow samples in Figure 3-6). Infrastructure development expanded even greater at 1233 km^2y^{-1}. China overtook the U.S in 2007 and Germany in 2009 to become the world's largest exporter since its accession to the World Trade Organization (WTO) in 2001. The enormous boom in manufacture plants in tandem with fast growing infrastructure investment, e.g. in transportation (Figure 3-2a), has facilitated the relocation of populations from inland rural villages to coastal cities engaged in the global marketplace (Song et al., 2018; Wang et al., 2012).

The increase in bare ground gain from resource extraction in North America post 2008 coincides with an expansion of shale-gas projects and new crude-oil exploration (red samples in Figure 3-6 and 3-2b-c). Led by new technologies of hydraulic fracturing and horizontal drilling, shale gas extraction has developed quickly in the U.S. and spread to Canada and other continents. The number of horizontal wells in U.S. alone doubled between 2008 and 2012 ("U.S. Energy Information Administration (EIA),"

n.d.). Local resource extraction driven by demand in distance and trade in global markets affected domestic and global investment and outcome in resources sector (Sonter et al., 2014). For example, Australia, where minerals are the largest export, had bare ground gain in resource extraction accounting for 60% of its total bare ground gain. Gold mining in Madre de Dios of Peru (Figure 3-2d), driven by a constant rate (~18%) of increasing gold prices (Asner et al., 2013; Swenson et al., 2011), was a source of the upward trend post-financial crisis in Latin America and the Caribbean.

3.4.2 Implications for near-real time monitoring of global and regional economic health

In the long run, the accumulated change of bare ground from anthropogenic demands is driven by population growth and economic development (Seto et al., 2012; Verburg et al., 2004). Our results also confirmed the coincident positive correlation between anthropogenic bare ground gain and changes in GDP at annual intervals (Table 3-5). Nevertheless, short-term factors that cause fluctuations in GDP, such as market anticipation, monetary system, technology innovation and policy decision, also affect annual changes in the quantity, attributes and spatial allocation of new bare ground. More importantly, the ability of the satellite-detected built-up area changes to signal economic recession with a one-year lead can effectively help policy makers to initiate counter-recession measures in a much more timely manner compared with the current policy-making practice. This ability can also help financial institutions and specialists to make much more informative investment decisions, and help the public to better prepare for economic recessions. Thus, it is important to

implement near-real time monitoring of bare ground gain at global and regional scales.

The ongoing earth observation programs of Landsat and Sentinel 2 satellites enable near-real time monitoring of land change at large scale as exemplified by an alert system of forest disturbance in operation on a weekly basis (Hansen et al., 2016). The surge of CubeSat (Hand, 2015) technology also provides high resolution images that are especially important for the validation and land-use attribution of bare ground gain. The latency of confirming bare ground gain and LCLU change attribution may be facilitated by high resolution observations and contextual inference. Our approach is scalable and bridges the relationship between socio-economics and land-use change at national or local scale, with a potential for operational implementation.

Table 3-1 Fixed effect regressions of economic variables on the 1yr-lagged sequences of different compositions of LCLU outcomes of bare ground gain (2001-2012).

	GDP	**Imports**	**Exports**	**Energy Use**	**Energy Produce**
	lag (1)	lag (1)	lag (1)	lag (1)	lag (1)
Anthropogenic BGG	0.066***	0.083***	0.082***	0.013**	0.010
	(0.016)	(0.029)	(0.027)	(0.006)	(0.006)
N	44	44	44	40	40
R-sq	0.31	0.21	0.19	0.13	0.07
F statistic	17.13	10.36	9.35	5.19	2.81
ID + CR + TR	0.055***	0.071**	0.062**	0.014**	0.010
	(0.015)	(0.027)	(0.025)	(0.006)	(0.007)
N	44	44	44	40	40
R-sq	0.26	0.15	0.14	0.13	0.068
F statistic	13.96	6.96	6.24	5.21	2.55
ID + CR	0.056***	0.072**	0.062**	0.016**	0.010
	(0.016)	(0.028)	(0.026)	(0.006)	(0.007)
N	44	44	44	40	40
R-sq	0.25	0.14	0.13	0.15	0.06
F statistic	12.80	6.58	5.65	6.39	2.13
CR	0.051***	0.066***	0.055***	0.016***	0.009
	(0.011)	(0.021)	(0.020)	(0.005)	(0.006)
N	44	44	44	40	40
R-sq	0.33	0.20	0.16	0.22	0.07
F statistic	19.64	9.56	7.50	9.94	2.71
ID	0.014	0.019	0.021	0.003	0.003
	(0.012)	(0.021)	(0.019)	(0.004)	(0.004)

N	44	44	44	40	40
R-sq	0.03	0.02	0.03	0.01	0.01
F statistic	1.37	0.82	1.20	0.46	0.44
RE	0.020*	0.036*	0.027	0.004	-0.002
	(0.010)	(0.019)	(0.018)	(0.004)	(0.004)
N	42	42	42	38	38
R-sq	0.09	0.085	0.06	0.04	0.01
F statistic	3.64	3.45	2.26	1.37	0.17

Notes: *** Significant at the p<0.01 level. ** Significant at the p<0.05 level. * Significant at the p<0.1 level.

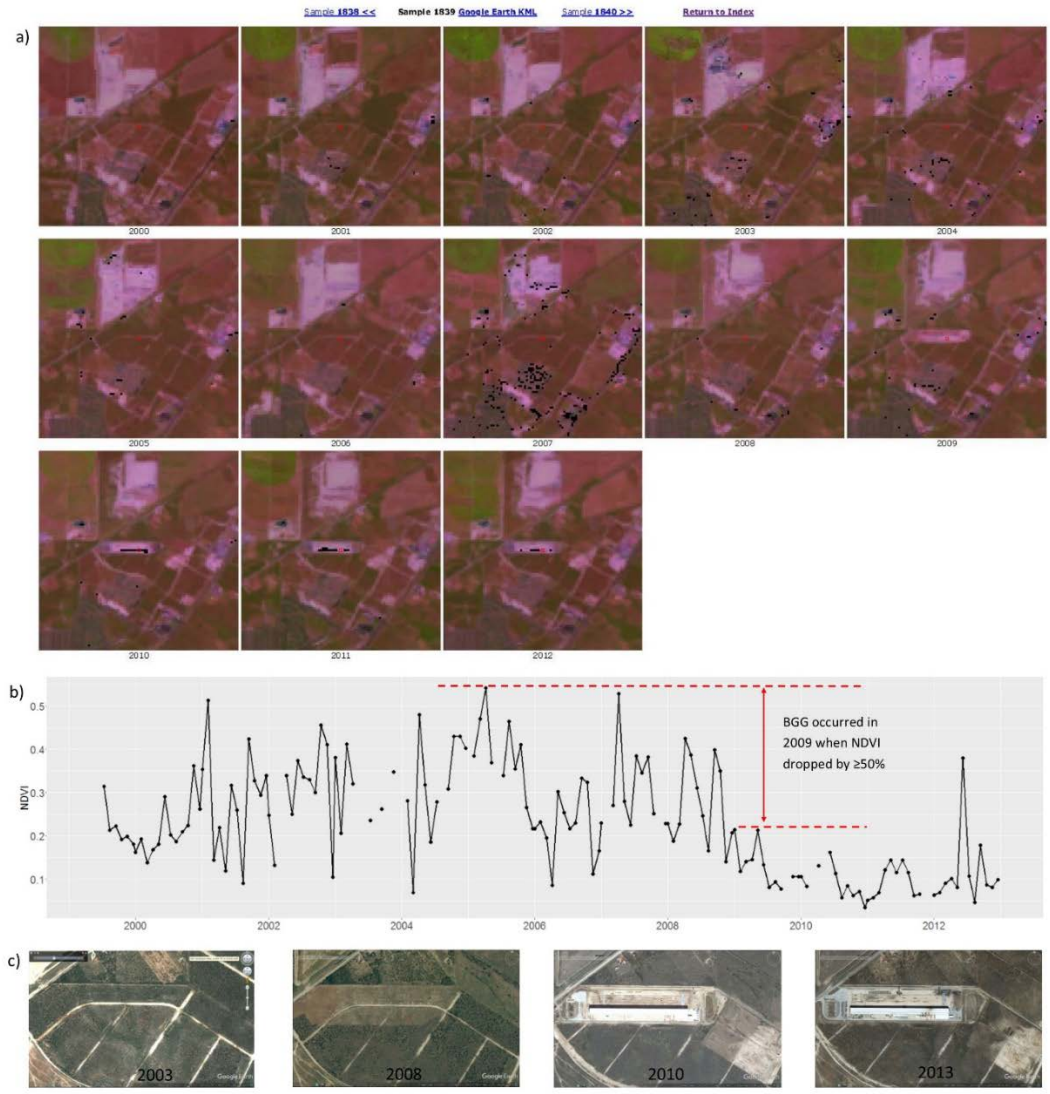

Figure 3-5 Attribution of LCLU outcomes of bare ground gain sample and interpretation of change year: a) Landsat time series of a ~9×9 km block (303×303 Landsat pixels) centered at a gain sample pixel (31.50º N 100.39º W) as shown in red square suggested bare ground gain occurred in 2009; b) NDVI 32-day time series of the sample pixel for 1999-2012 demonstrated vegetation lost by over 50% starting at 2009 and lasting for at least three years; c) Screenshots taken from Google Earth confirmed our interpretation on change year with an attribution of bare ground gain as commercial/residential built-up area. Landsat images are false color composites of Shortwave Infrared (SWIR 1.55-1.75 µm), Near-Infrared (NIR 0.77-0.90 µm) and Red (0.63-0.69 µm) bands. NDVI sequences were extracted from Landsat 7 collection 1 tier 1 32-day NDVI composite available on Google Earth Engine.

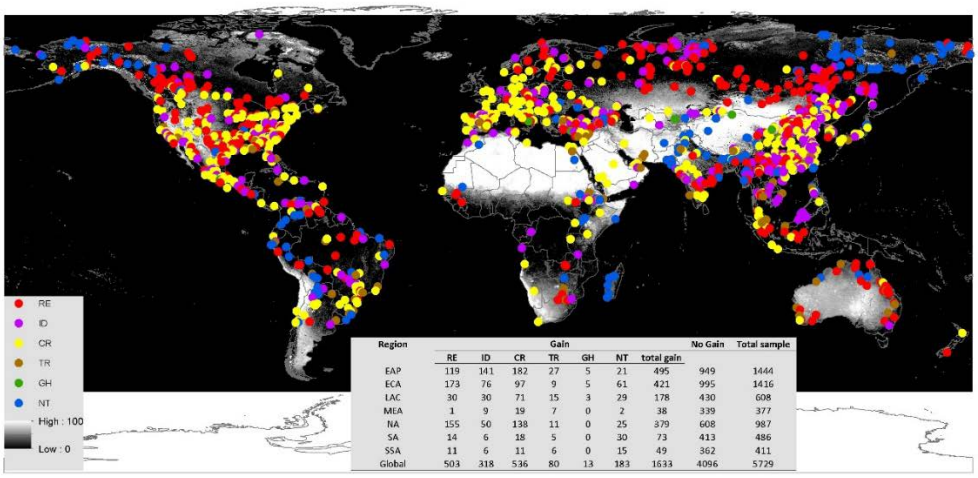

Region	Gain							No Gain	Total sample
	RE	ID	CR	TR	GH	NT	total gain		
EAP	119	141	182	27	5	21	495	949	1444
ECA	173	76	97	9	5	61	421	995	1416
LAC	30	30	71	15	3	29	178	430	608
MEA	1	9	19	7	0	2	38	339	377
NA	155	50	138	11	0	25	379	608	987
SA	14	6	18	5	0	30	73	413	486
SSA	11	6	11	6	0	15	49	362	411
Global	503	318	536	80	13	183	1633	4096	5729

Figure 3-6 Spatial distribution of LCLU outcomes of sample pixels. The inset table summarizes the sample counts by region (2 sample pixels of bare ground gain and 19 of no gain not counted due to out of the continental boundaries). Background layer ranging from 80º N to 60º S except Greenland is percent bare ground cover that is per pixel the median value of percent bare ground cover in the last three years (2010, 2011, and 2012). RE denotes resource extraction; ID denotes infrastructural development; CR denotes commercial/residential built-up area; TR denotes transitional bare ground gain; GH denotes greenhouses; NT denotes natural bare ground gain, thereafter.

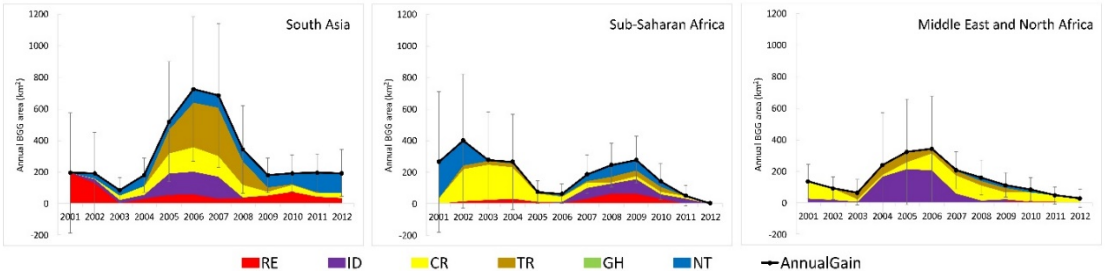

Figure 3-7 Temporal bare ground gain areas in three regions (South Asia, Sub-Saharan Africa, Middle East and North Africa) that were excluded from panel analysis for high uncertainty.

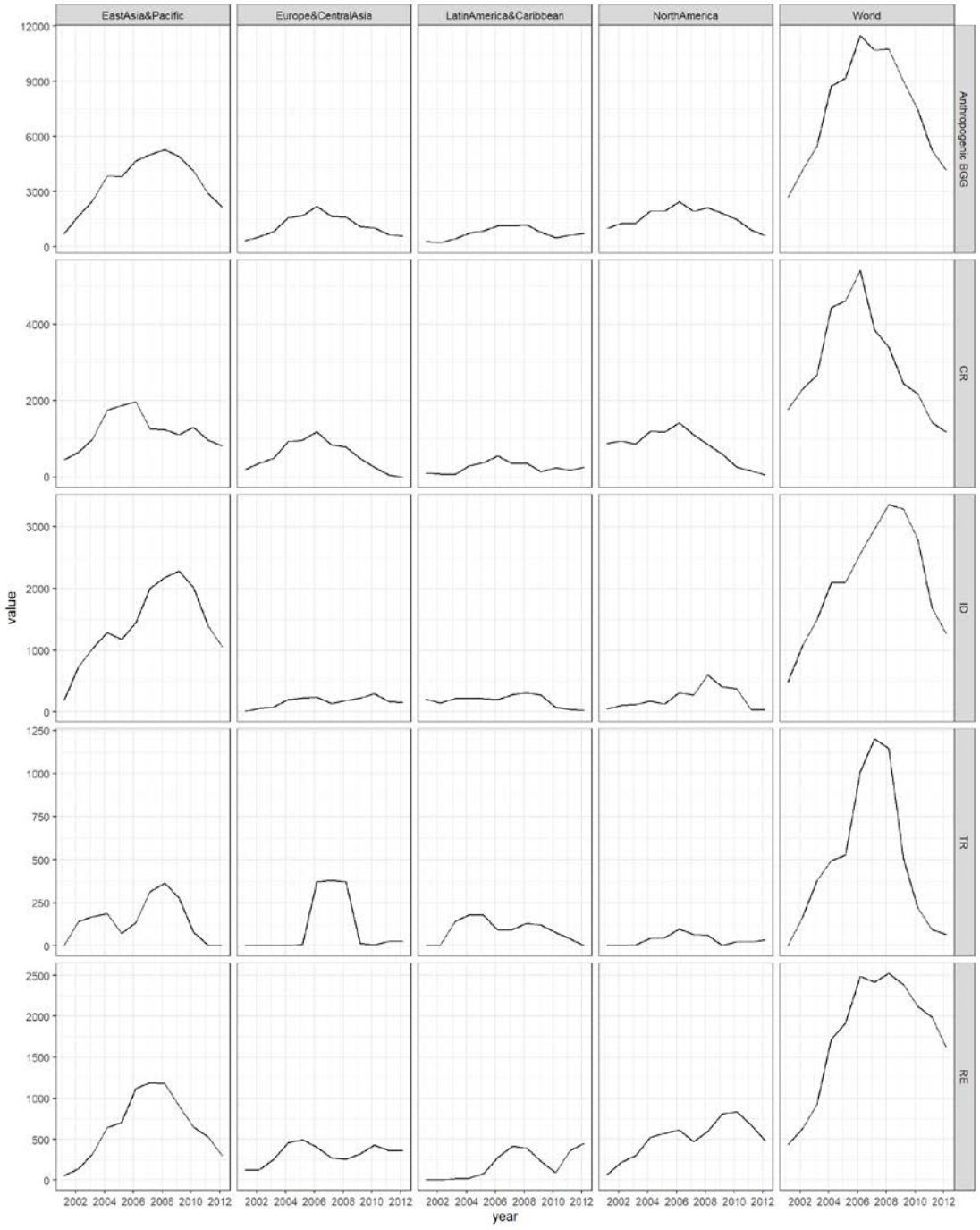

Figure 3-8 Temporal anthropogenic bare ground gain, commercial/residential built-up area, infrastructure development, transitional bare ground gain and resource extraction (unit: km^2) at global and regional level.

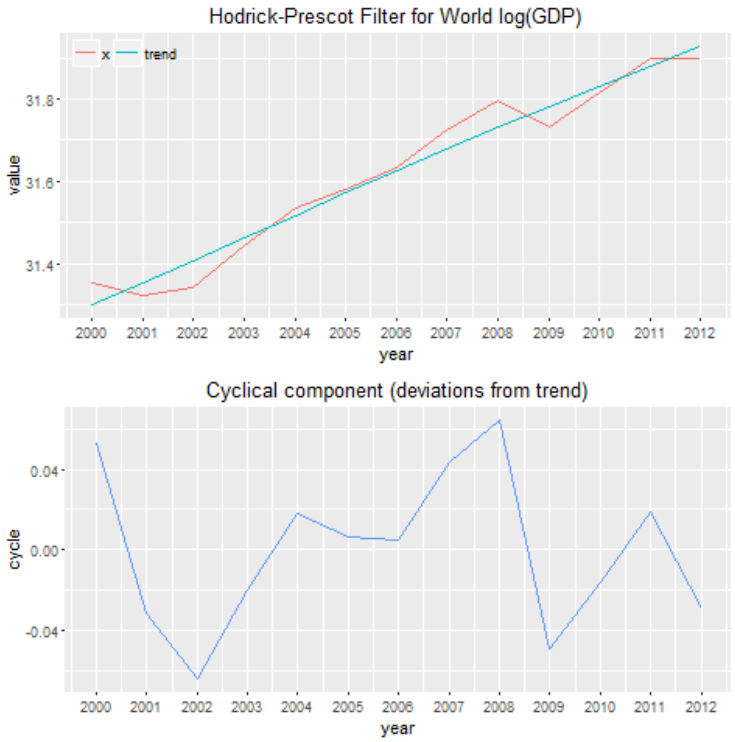

Figure 3-9 Time sequences of natural log GDP (red), growth trend and cyclical component decomposed by Hodrick-Prescot Filter (λ=100).

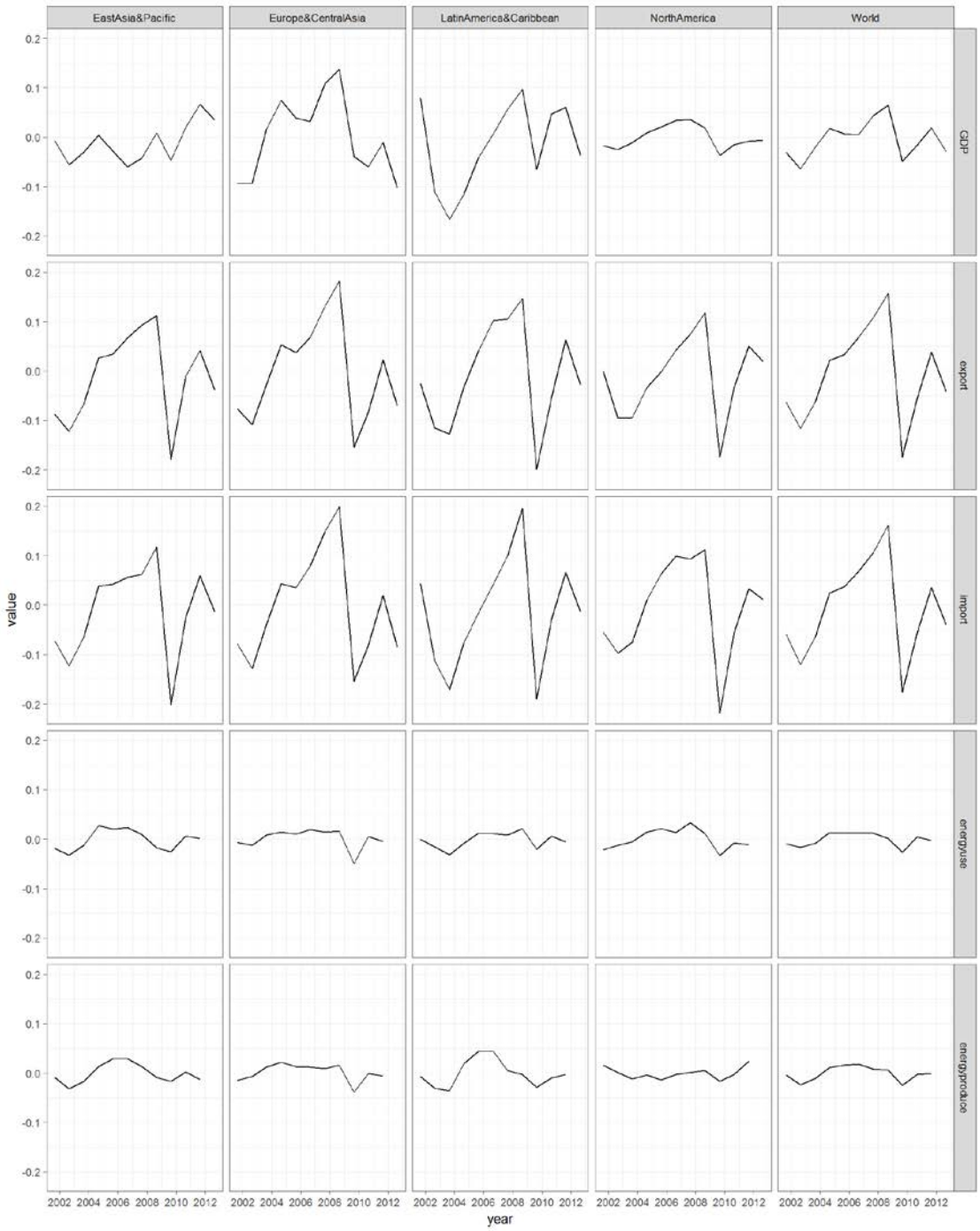

Figure 3-10 De-trended economic variables showing economic fluctuations at global and regional scale in 2001-2012. All economic variables are after natural logarithm and de-trended, and therefore unitless.

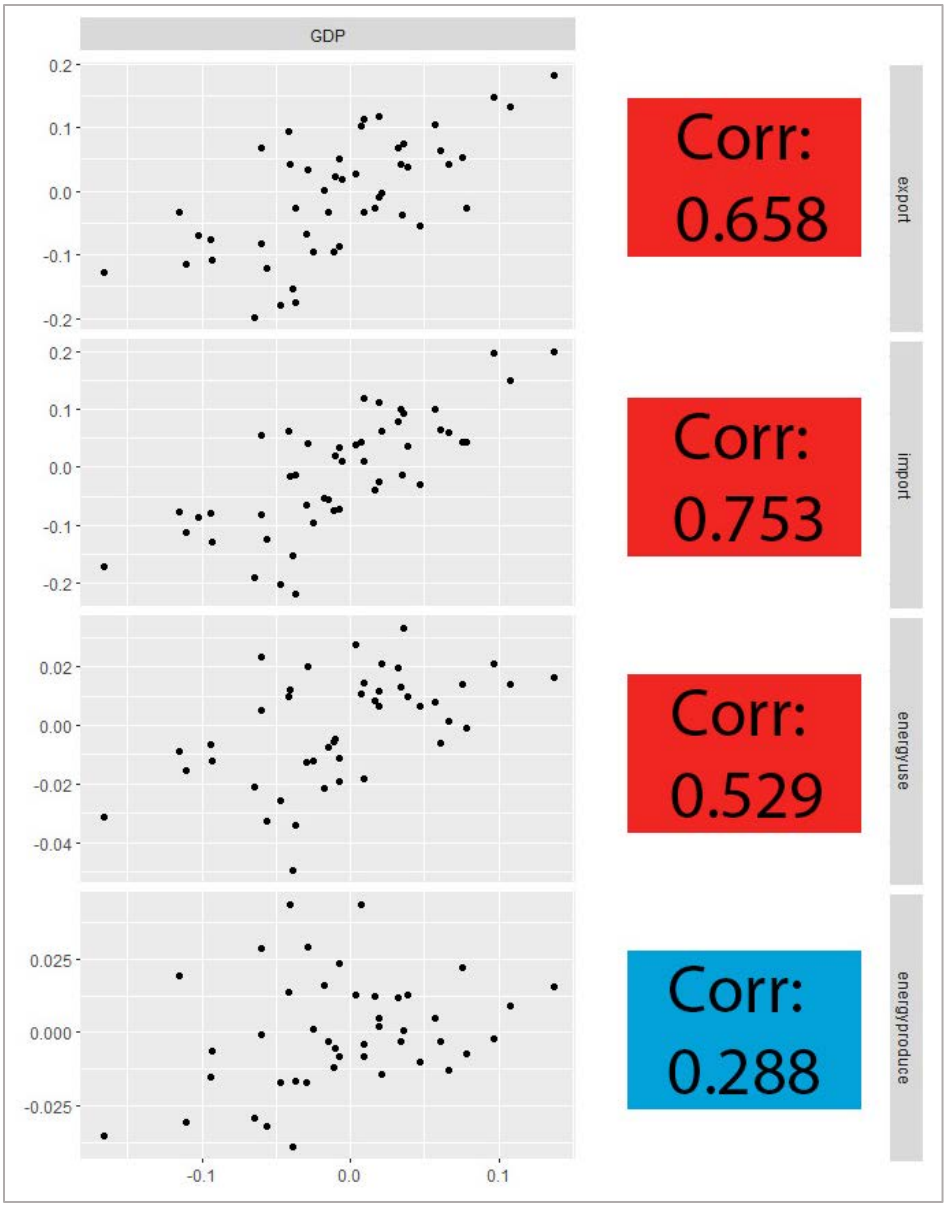

Figure 3-11 Pearson correlation tests of pooled GDP and merchandise exports, merchandise imports, energy use and energy production, respectively. All economic variables are after natural logarithm and de-trended, and therefore unitless. Scatter plots on the left and correlation coefficients on the right with significant levels colored in red ($p<0.001$) and blue ($p<0.1$).

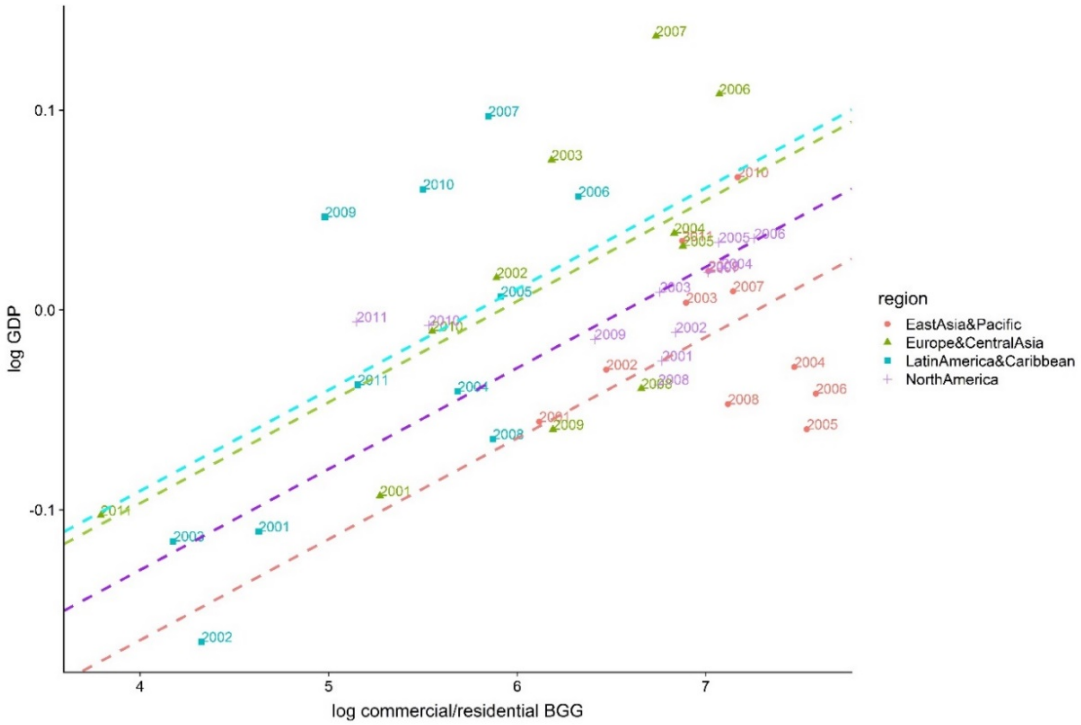

Figure 3-12 De-trended GDP (natural log) versus one-year lagged bare ground gain of commercial/residential built-up area (natural log). The labeled year t besides each point denotes bare ground gain in year t *and GDP in year* t+*1. Panel regressions shown in dash lines.*

Table 3-2 Sample distribution by change time and region.

Year	EAP	ECA	LAC	MEA	NA	SA	SSA	Global
2001	13	5	4	5	10	1	1	39
2002	30	26	11	1	27	0	2	97
2003	43	35	5	0	39	7	7	136
2004	39	47	11	4	42	2	5	150
2005	48	56	24	3	51	12	5	199
2006	65	48	24	6	60	15	2	220
2007	73	57	30	7	56	14	7	244
2008	57	56	31	6	34	5	13	202
2009	49	41	15	3	31	6	3	148
2010	46	26	12	2	16	5	4	111

2011	24	17	4	1	12	3	0	61
2012	8	7	7	0	1	3	0	26

Table 3-3 Temporal bare ground gain and LCLU outcomes (km^2) at global and regional scale.

region	year	Sum	RE	ID	CR	TR	NT	GH
Global	2001	3118	433	486	1768	0	431	0
Global	2002	4522	635	1079	2299	169	340	0
Global	2003	5635	929	1487	2666	378	175	0
Global	2004	8894	1720	2091	4429	494	157	3
Global	2005	9404	1917	2096	4617	526	240	7
Global	2006	11878	2488	2560	5417	1008	398	7
Global	2007	11330	2415	2955	3849	1202	640	268
Global	2008	11485	2525	3357	3396	1147	706	355
Global	2009	9710	2388	3283	2443	508	705	385
Global	2010	7989	2121	2792	2171	222	543	141
Global	2011	5838	1988	1681	1435	96	588	50
Global	2012	4772	1624	1268	1171	65	614	30
EAP	2001	767	53	188	453	0	73	0
EAP	2002	1713	139	730	647	141	56	0
EAP	2003	2548	318	1033	988	169	41	0
EAP	2004	3888	645	1284	1754	185	19	0
EAP	2005	3834	703	1169	1874	73	16	0
EAP	2006	4714	1122	1446	1967	133	46	0
EAP	2007	5182	1193	1997	1268	315	173	236
EAP	2008	5454	1181	2174	1234	362	176	327
EAP	2009	5109	907	2276	1112	279	208	327
EAP	2010	4208	653	2016	1298	81	69	91
EAP	2011	2989	530	1399	968	5	87	0
EAP	2012	2193	294	1052	808	0	38	0
ECA	2001	360	120	10	195	0	36	0
ECA	2002	574	128	59	361	0	26	0
ECA	2003	856	256	78	484	0	38	0
ECA	2004	1626	458	203	928	0	38	0
ECA	2005	1781	494	226	971	10	79	0
ECA	2006	2295	403	243	1178	373	98	0
ECA	2007	1764	271	140	842	381	105	26
ECA	2008	1761	256	185	779	371	144	26
ECA	2009	1225	322	221	487	14	126	55

ECA	2010	1139	426	293	257	5	108	50
ECA	2011	693	365	173	44	26	36	50
ECA	2012	603	363	151	0	30	29	30
LAC	2001	399	0	207	102	0	90	0
LAC	2002	287	0	147	76	4	60	0
LAC	2003	491	22	221	65	140	43	0
LAC	2004	735	27	226	294	179	6	3
LAC	2005	924	79	220	370	178	70	7
LAC	2006	1241	280	203	558	93	100	7
LAC	2007	1266	415	279	346	96	122	7
LAC	2008	1271	390	311	355	133	80	3
LAC	2009	878	229	271	146	121	109	3
LAC	2010	699	90	73	245	79	212	0
LAC	2011	955	363	39	173	39	340	0
LAC	2012	1160	452	30	256	0	422	0
NA	2001	996	65	53	870	0	7	0
NA	2002	1269	218	102	935	0	14	0
NA	2003	1310	303	125	859	6	16	0
NA	2004	1959	527	180	1191	42	18	0
NA	2005	1946	574	129	1176	47	20	0
NA	2006	2496	615	313	1418	98	52	0
NA	2007	2039	470	274	1111	66	118	0
NA	2008	2249	598	597	852	62	141	0
NA	2009	1928	804	405	609	4	106	0
NA	2010	1524	836	378	253	23	34	0
NA	2011	908	674	39	172	23	0	0
NA	2012	595	481	35	44	35	0	0

Table 3-4 List of dependent economic variables.

Explanatory variables	Description from the World Bank
GDP	The sum of gross value added by all resident producers in the economy plus any product taxes and minus any subsidies not included in the value of the products in current U.S. dollars.
Merchandise imports	The c.i.f. (cost, insurance and freight included) value of goods received from the rest of the world valued in current U.S. dollars.
Merchandise exports	The f.o.b (free on board) value of goods provided to the rest of the world valued in current U.S. dollars.
Energy use	Use of primary energy before transformation to other end-use fuels, which is equal to indigenous production plus imports and stock changes, minus exports and fuels supplied to ships and aircraft engaged in international transport, all converted into oil equivalents.
Energy production	Forms of primary energy--petroleum (crude oil, natural gas liquids, and oil from nonconventional sources), natural gas, solid fuels (coal, lignite, and other derived fuels), and combustible renewables and waste--and primary electricity, all converted into oil equivalents.

Table 3-5 Fixed effect regressions of economic variables on the coincident sequences of different compositions of LCLU outcomes of bare ground gain (2001-2012).

	GDP	**Imports**	**Exports**	**Energy Use**	**Energy Produce**
	coincident	coincident	coincident	coincident	coincident
Anthropogenic BGG	0.049***	0.090***	0.089***	0.018***	0.016***
	(0.017)	(0.026)	(0.024)	(0.005)	(0.006)
N	48	48	48	44	44
R-sq	0.17	0.22	0.25	0.24	0.17
F statistic	8.67	11.83	14.33	12.48	8.10
ID + CR + TR	0.033**	0.053**	0.050**	0.016***	0.012**
	(0.013)	(0.022)	(0.020)	(0.005)	(0.005)
N	48	48	48	44	44
R-sq	0.13	0.12	0.13	0.22	0.12
F statistic	6.25	5.96	6.33	11.14	5.13
ID + CR	0.033**	0.048**	0.044**	0.016***	0.012**
	(0.013)	(0.022)	(0.020)	(0.005)	(0.005)
N	48	48	48	44	44
R-sq	0.12	0.10	0.10	0.23	0.12
F statistic	5.97	4.88	4.85	11.72	5.16
CR	0.027**	0.044**	0.040**	0.014***	0.013**
	(0.011)	(0.019)	(0.017)	(0.004)	(0.004)
N	47	47	47	44	44
R-sq	0.12	0.12	0.12	0.29	0.22
F statistic	5.98	5.70	5.56	15.59	11.10

ID	0.011	0.018	0.018	0.005	0.001
	(0.011)	(0.018)	(0.017)	(0.004)	(0.004)
N	48	48	48	44	44
R-sq	0.02	0.02	0.03	0.04	0.00
F statistic	0.94	0.93	1.18	1.61	0.12
RE	0.028**	0.051***	0.043**	0.009**	0.004
	(0.011)	(0.018)	(0.016)	(0.003)	(0.004)
N	46	46	46	42	42
R-sq	0.14	0.17	0.14	0.15	0.04
F statistic	6.89	8.23	6.83	6.75	1.40

Notes: *** Significant at the p<0.01 level. ** Significant at the p<0.05 level. * Significant at the p<0.1 level.

Table 3-6 Fixed effect regressions of economic variables on the coincident sequences or 1yr-lagged sequences of different compositions of LCLU outcomes of bare ground gain (2001-2010).

	GDP		**Merchandise Imports**		**Merchandise Exports**		**Energy Use**		**Energy Production**	
	coincident	lag (1)	coincident	lag (1)	coincident	lag (1)	coincident	lag (1)	coincident	lag (1)
Anthropogenic BGG	0.053***	0.064***	0.108***	0.097***	0.110***	0.088***	0.018***	0.013**	0.018***	0.011*
	(0.018)	(0.016)	(0.030)	(0.032)	(0.026)	(0.030)	(0.006)	(0.006)	(0.006)	(0.006)
N	40	36	40	36	40	36	40	36	40	36
R-sq	0.19	0.34	0.27	0.22	0.33	0.22	0.23	0.13	0.22	0.09
F statistic	8.42	16.00	13.13	8.96	17.57	8.56	10.75	4.48	9.61	3.01
ID + CR + TR	0.057***	0.066***	0.120***	0.104***	0.120***	0.096***	0.019***	0.013*	0.020***	0.013*
	(0.019)	(0.018)	(0.030)	(0.035)	(0.027)	(0.032)	(0.006)	(0.007)	(0.006)	(0.007)

N	40	36	40	36	40	36	40	36	40	36
R-sq	0.21	0.31	0.31	0.22	0.37	0.23	0.24	0.12	0.24	0.11
F statistic	9.27	14.01	15.42	8.86	20.13	9.00	11.24	4.06	11.25	3.70
ID + CR	0.063***	0.070***	0.129***	0.114***	0.128***	0.104***	0.022***	0.016**	0.022***	0.014*
	(0.020)	(0.019)	(0.033)	(0.038)	(0.030)	(0.035)	(0.006)	(0.007)	(0.006)	(0.007)
N	40	36	40	36	40	36	40	36	40	36
R-sq	0.22	0.30	0.30	0.23	0.36	0.23	0.27	0.14	0.27	0.10
F statistic	10.03	13.27	15.36	9.16	19.51	9.07	12.64	5.06	13.08	3.39
CR	0.058***	0.068***	0.114***	0.117***	0.111***	0.105***	0.021***	0.017***	0.023***	0.015**
	(0.016)	(0.016)	(0.026)	(0.031)	(0.023)	(0.028)	(0.005)	(0.006)	(0.004)	(0.006)
N	40	36	40	36	40	36	40	36	40	36
R-sq	0.29	0.38	0.36	0.32	0.41	0.31	0.38	0.22	0.45	0.15
F statistic	14.03	18.69	20.01	14.76	24.21	13.74	21.36	8.50	28.07	5.49
ID	0.020	0.025*	0.037	0.031	0.038*	0.032	0.005	0.004	0.004	0.003
	(0.014)	(0.014)	(0.024)	(0.027)	(0.032)	(0.024)	(0.004)	(0.005)	(0.004)	(0.005)
N	40	36	40	36	40	36	40	36	40	36
R-sq	0.06	0.09	0.06	0.04	0.08	0.05	0.03	0.02	0.02	0.01
F statistic	2.12	3.04	2.42	1.38	3.15	1.75	1.19	0.66	0.63	0.39
RE	0.031***	0.025**	0.053**	0.039*	0.045**	0.029	0.010**	0.005	0.005	-0.002
	(0.011)	(0.010)	(0.020)	(0.022)	(0.019)	(0.020)	(0.004)	(0.004)	(0.004)	(0.004)
N	38	34	38	34	38	34	38	34	38	34
R-sq	0.19	0.17	0.17	0.099	0.15	0.07	0.18	0.05	0.04	0.01
F statistic	7.93	6.02	6.87	3.19	5.79	2.06	7.31	1.54	1.36	0.34

Notes: *** Significant at the p<0.01 level. ** Significant at the p<0.05 level. * Significant at the p<0.1 level.

Chapter 4 Application of deep convolutional neural network in automatic land attribution: An example of CONUS airport detection[3]

4.1 Introduction

Remote sensing facilitates the quantification of land use change, helping us to understand the drivers of global environmental change (Townshend et al., 1991; Turner B. L. et al., 2007). Land cover consists of land surface of different biophysical and geophysical properties in the form of forest, shrub, herbaceous vegetation, bare ground, water (solid or liquid) and others. In Chapter 2, global bare ground was characterized as fractional cover from Landsat imagery. Land-cover changes in the processes and events of internal geology, surface biogeography, long-term climate, short-term meteorology, and human-induced conversion and modification (Curtis et al., 2018; Hosonuma et al., 2012; Tyukavina et al., 2018, 2017). Land use depicts anthropogenic use of land for the production of food, fuel and fiber, and settlements associated with residential and commercial land uses, changing the physical and functional attributes of original land cover (Foley et al., 2005). In Chapter 2 and 3, I estimated natural and land-use areas resulting in bare ground gain by manually interpreting probability samples that were randomly selected from strata constructed

[3] The presented material is being prepared for publication: Ying, Q., Serna, A., Hansen, M.C., Potapov, P.V., Steininger, M. Application of deep convolutional neural network in automatic land attribution: An example of CONUS airport detection.

by Landsat-based maps of bare ground gain maps. This method of land attribution from samples has been used in other land classifications (e.g., Curtis et al., 2018; Song et al., 2017; Zalles et al., 2019), with drawbacks that include intensive labor for sample interpretation and the lack of spatially explicit results. The method developed in Chapters 2 relies on visually interpreted samples in the estimation of areas of bare ground gain and land use outcome. The findings of Chapter 2 were applied in Chapter 3 to assess changes in bare ground and bare ground types over the past 12 years and their statistical relationship to global and continental economic indicators. Some of the trends in bare-ground and types show promise for serving as leading indicators of broad economic cycles. The previous chapters show that even when using state-of-the-art data analysis and mining the entire Landsat archive, an approach based solely on classification would be too unreliable to monitor trends and provide indicators. Likewise, an approach based on non-stratified sampling would require enormous sample sizes and thus would be too laborious and slow to provide timely indicators. The hybrid approach used, with automated classification to create strata and non-automated interpretation of a relatively small sample, is appropriate in this context.

The approach used, however, does rely on human interpretation of a sample, and this would be the main constraint to rapid delivery of annual indicators if this were implemented as an operational system. Given a political desire for real or near-real time indicators, any improvements to the efficiency, timeliness or accuracy of indicators is of interest. I propose three ways in which timeliness could potentially be improved, each via automated classification of the types of bare-ground change, rather than just of total bare-ground change as done in the previous chapters. First, if

sufficiently accurate, automated classification could be used directly for estimation of bare-ground types, replacing estimation from the interpretation of a sample. Second, classification could be used to improve the stratification, by adding strata for different types, and thus theoretically increase sampling efficiency. Third, it could be used to ease the sample-interpretation effort, for example by pre-labelling sample locations or by recommending interpretation only for locations with lower classification probabilities. Among these options, the first implies the greatest demand on classification accuracy, the second the least demand, and the third a moderate demand and some use of the classification probabilities.

When interpreting samples, analysts interpret the spatial context, including shape, texture, pattern, and do not solely rely on the spectral response of the individual pixel being labeled. While bare ground has a rather unambiguous spectral signature, land use types within bare ground, such as resource extraction and commercial and residential settled areas, do not. They are more readily recognized by their spatial attributes. In remote sensing, object-based classifiers and deep-learning algorithms make use of spatial pattern and contextual data of identified objects (Wang et al., 2010; Zhang et al., 2019; Zhu et al., 2012). Such methods are potentially most appropriate for applications such as automated classification of airports.

In this chapter I use airport mapping in the conterminous United States (CONUS) as an application of mapping a bare ground land use as an example of state-of-the-art deep learning for automatic land attribution in scale. Infrastructure development accounted for 21% of bare ground gain in the world and 14% in the US between 2000 and 2012, and airports are an important component of transportation

infrastructure that promotes regional economy that is often the center of development serving as a modern version of a central business district. Attributing land areas used for airports will advance land resource planning, management and evaluation.

Advances in deep learning have been applied in real life improvements, for example, self-driving vehicles, civil surveillance, smart medical systems, financial trades (Falk et al., 2019; LeCun et al., 2015; Najafabadi et al., 2015). Remote sensing communities have been motivated to use deep convolutional neural network (CNN) in land cover and land use change studies in the era of explosive satellite image acquisitions (Ma et al., 2019). One of the advantages of deep convolutional neural networks is automatic feature extraction across scale (P. Li et al., 2018; Tuia et al., 2015), which is an independent work from conventional machine learning algorithms (Aytekin et al., 2013; Tao et al., 2011). Layers of convolutional calculation represent abstracts aggregated from low to high levels, which enables hierarchical learning process of critical signal patterns, such as point, edge, and texture in the spatial dimension and high/low frequency, high/low amplitude in temporal dimension (Najafabadi et al., 2015). Another advantage is improved predictive performance of models with larger training data and increased parameter complexity compared to conventional machine learning algorithms hindered by over-fitting problems. For example, Kussul et al. (2017) classified crop types, forest, grassland, bare land and water cover in the Kyiv region of Ukraine from Landsat 8 and Sentinel-1A imagery using a multilevel deep learning architecture that resulted in a higher overall accuracy compared to random forests (RF) with significant improvements in producer's accuracy for maize and in user's accuracy for grassland and bare land.

Airport land use attribution can be decomposed to two tasks, airport pixel classification that partitions pixels into airport land versus other and airport object detection that identifies pixels belonging to a single airport. The basic idea of object detection is to propose regions of interest (RoI) and predict the most possible location. Many studies proposed frameworks to detect airports in high resolution satellite images using deep convolutional neural networks, but most of them only focused on object-based algorithms, ignoring potential contribution from pixel-based classification algorithm (Chen et al., 2018; Xiao et al., 2017; Xu et al., 2018; Zhang et al., 2017). Additionally, deep learning models were more frequently used in satellite images with spatial resolutions of 10 m or finer. There have been a limited number of studies that focused on actual practical land attribution tasks rather than using standard datasets created for model testing (Ma et al., 2019).

We propose here deep learning protocols that combine a pixel-based convolutional neural network, U-Net, and an object-based network, Faster R-CNN, for operational airport detection at national scale from Landsat images. The pixel-based U-Net is a fast symmetric network developed originally for cell counting and morphology measure in medical images (Falk et al., 2019). Modifications of U-Net were applied to satellite images for road extraction and sea-land classification (R. Li et al., 2018; Zhang et al., 2018). Girshick et al. (2014) created region-based convolutional neural networks (R-CNN) for object detection, which used selective search algorithm to propose object regions and convolutional neural networks to predict locations. Ren et al. (2017) created an improved network, Faster R-CNN, which replaced a time-consuming selective search algorithm with regions proposed and predicted by the

convolutional neural networks. A unique construction of convolutional neural network is called an architecture, which includes convolutional layers, pooling layers, rectified linear units, fully connected layers. We did not change the architecture of the established convolutional neural networks applied in our proposed deep learning system as our objective was to explore the feasibility of applying deep convolutional neural networks to operational, end-to-end airport land attribution at scale and assess the effectiveness of such system performed on medium resolution Landsat images.

The purpose of this chapter is to test the ability of a deep-learning algorithm to accurately classify airports, by examining two approaches. The first applies solely an object detection via convolution neural networks to find objects that contain airports. The second approach applies the same object-based technique, although inputs are the probabilities produced by the U-Net classification. Specifically, we evaluate the accuracy of airport classification by these two deep-learning approaches as a demonstration of direct bare ground land use attribution.

4.2 Data

4.2.1 Landsat data processing and metrics generation

We employed Landsat data to develop deep learning protocols for operational airport detection on medium-resolution optical satellite images. The Landsat series of Earth Observation satellites have been continuously acquiring images of global land for over 40 years, which provides unique multi-spectral imagery archive free of charge for land cover and land use change characterization at fine landscape scale (Hansen and Loveland, 2012; Wulder et al., 2019). Analysis Ready Data (ARD) are

the are imagery that are consistently processed time-series of land surface reflectance and cloud/shadow/snow/water flags (Dwyer et al., 2018; Roy et al., 2010).

The global Landsat ARD produced by the Global Land Analysis and Discovery team (GLAD) provides seamlessly tiled images of consistently normalized land surface reflectance with global coverage at 16-day interval in snow-free times of the year 1997 to present (Potapov et al., 2020). The high Arctic and Antarctic regions are excluded due to low winter sun angles and persistent snow/ice and cloud cover. The geometrically corrected and radiometrically calibrate Landsat images were downloaded from the Landsat Collection 1 data stored in the United States Geological Survey Earth Resources Observation and Science Center (USGS EROS). The radiation measurements were converted to top-of-atmosphere reflectance per spectral band and brightness temperature for thermal band (Chander et al., 2009). Quality assessment was performed per pixel to flag cloud / haze contamination, cloud / topographic shadow, snow / ice and water cover. The clear-sky TOA reflectance was normalized per spectral band to address atmospheric impacts and surface anisotropy due to sensor off-nadir scan with a normalization target derived from growing season Moderate Resolution Imaging Spectroradiometer (MODIS) surface reflectance product (Hansen et al., 2008; Potapov et al., 2011, 2012). The normalized surface reflectance per clear-sky observation was temporally aggregated in every 16-day interval and put in a 1x1 degree tile, converting Landsat scene acquisitions to spatially consistent wall-to-wall composites. Annual phenological multi-temporal metrics were further calculated from 16-day time series for land cover characterization. This ready-to-use GLAD ARD can be applied to various operations

aiming at large-scale land cover and land use change monitoring, thus fits well in the deep learning protocols proposed in the presented study.

The proposed protocols took advantages of two deep CNN algorithms: U-Net is able to take in multiple-band images/time series and perform pixel level classification, and Faster R-CNN is designed to take in at most three bands to carry out object level detection. Therefore, the creation of input images was configured for each algorithm, respectively. We used composites of Red (R), Near Infrared (NIR), Short Wave Infrared 1.547- 1.749 µm (SWIR 1) with the best clear-sky observation in growing seasons of the year 2012 and 2018 from GLAD ARD for Faster R-CNN. To explore the U-Net capability, we used all of the spectral bands and selected multi-temporal statistical metrics (Table 4-1) from GLAD ARD in 2018 that were visually favorable to airport runways, buildings, and background grass (Potapov et al., 2020). We divided original GLAD ARD tiles in a size of 1x1 degree to quarter degree (1000 x 1000 pixels of 0.00025-degree resolution) to meet the image size limitation of Faster R-CNN algorithm. There are 13893 quarter degree tiles in CONUS.

4.2.2 Training data

Training data sets were acquired from two sources: global airport location points from the Global Airport Database (https://www.partow.net/miscellaneous/airportdatabase/index.html#Downloads) and North America airport boundaries and runways included within Esri Data and Maps (https://www.arcgis.com/home/item.html?id=c392e571683d44ac8ff0b718e3a24105). Neither of the datasets is inclusive to all the airports, civil or military, public or

private, in its geographic extent. The Global Airport Database contains geographical points of 4188 airports with attributes of airport name, International Air Transport Association (IATA) code etc., around the world, where 426 airports are located within CONUS (Figure 4-1 a, c). This dataset was used to locate centers of training images cropped from the Landsat composite in 2012. We then drew bounding boxes of all the airports visible from the training images, with the help of an image annotation tool developed for object detection with deep CNN -- LabelImg (https://github.com/tzutalin/labelImg). The bounding boxes stored in xml files along with training images were training data for Faster R-CNN object detection algorithm (Figure 4-1 b). The North America airport dataset has more spatial detail on the shape of runways and the boundaries of airport land use (Figure 4-1 b) and served as training data for Unet pixel classification algorithm. Due to the limit of GPU capacity, only 150 multi-band images were used to train U-Net.

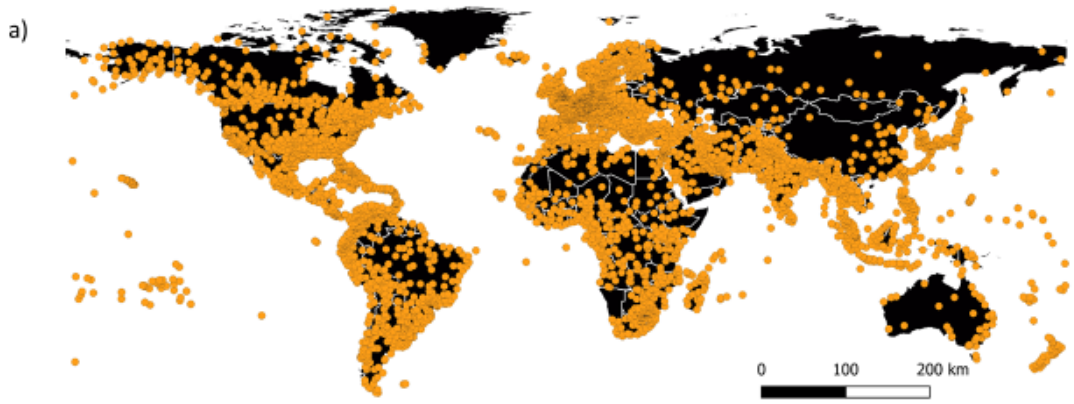

c)

Continent	Airport count
North America	900
South America	521
Europe	1101
Africa	604
Asia	895
Australia and Oceania	167
Total	4188

Figure 4-1 Airport data collected for training data construction: a) Global airport location points from Global Airport Database used to crop training images for Faster R-CNN object detection; b) Bounding box as shown in yellow rectangle, which served as training data for Faster R-CNN, was drawn in the annotation tool – LableImg. An example of Atlanta International Airport from North America Airport dataset shows training data of runways in blue and airport territory boundaries in berry for U-Net per pixel classification; c) Continental airport counts of Global Airport Database.

4.3 Methodology

4.3.1 Deep learning approach for operational airport detection

We propose an evaluation of Landsat-based deep learning approaches to mapping airports that include a stand-alone, object-detection network and a combined object-detection network that employs as an input a per-pixel segmentation network. Land use activities occur in patches of pixels which, for the purposes of this study, we call

objects, and the goal of this study objective is airport object detection. Faster R-CNN was the winner of many evaluated algorithms in object detection competitions of 2015 from intelligent computer vision field (Ren et al., 2015). Advancements of Faster R-CNN include fast model training and prediction with large datasets and accurate object localization. Current Faster R-CNN applications process three-band images, which is common in natural world image scenarios, but rather limited in multi-spectral satellite images data. U-Net, on the contrary, is a deep convolutional neural network that can learn from images consisting of many bands. However, it classifies pixels rather than identifying object instances. We propose an integrated airport detecting system that employed Faster R-CNN (details as described in section 3.1.1) as a centerpiece of object detection and the output from U-Net (section 3.1.2) as the feature input for Faster R-CNN. Specifically, we used U-Net with an input of 27 multitemporal metrics from GLAD Landsat ARD to predict a per-pixel probability map of airport land use, which was then fed to Faster R-CNN for airport object detection. Through integration of two CNNs, we will assess the full use of multitemporal metrics generated from dense satellite time-series and improved detection precision compared to only applying Faster R-CNN.

We implemented the Faster R-CNN only approach (hereafter referred to as "Faster R-CNN"), and the integrated R-CNN + U-Net approach to map airports in CONUS and evaluated the two resulting maps under the same stratified sampling design. Figure 4-2 illustrated the experimental design: The input of the Faster R-CNN only approach was a Landsat SWIR1-NIR-R composite, whereas that for the proposed integration approach was a set of multi-temporal Landsat metrics. Faster R-

CNN outputs, whether performed directly on the Landsat composite image or on the probability layer from U-Net, result in bounding boxes and associated probabilities for detected airport objects (colored rectangular area in outputs as shown in Figure 4-2). We performed accuracy assessments of the two maps using a set of validation sample collected from a stratification defined by the union of the two outputs.

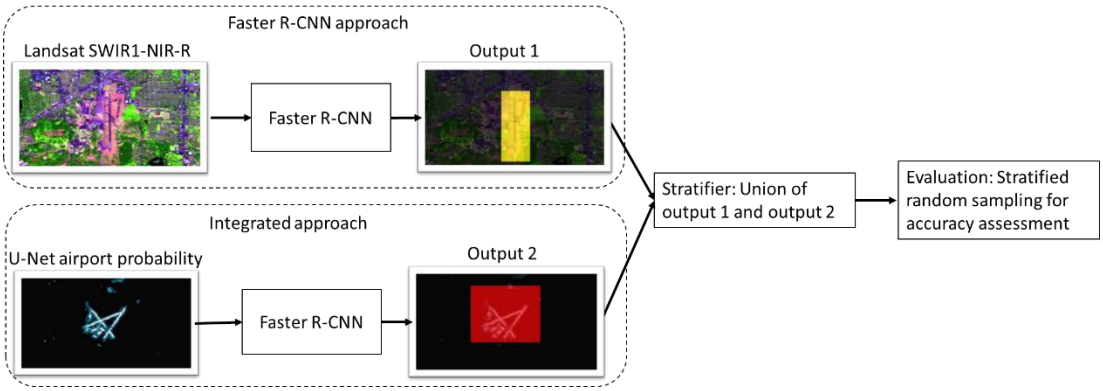

Figure 4-2 Experiments of comparing the proposed integrated approach that combines an object detection network (Faster R-CNN) with a pixel-level sematic segmentation network (U-Net) and the Faster R-CNN approach for operational airport land attribution using Landsat data. Colored rectangles in the outputs are detected airport objects.

4.3.1.1 Object-based Faster R-CNN

We used Faster R-CNN for airport object detection, which is an advanced algorithm in R-CNN family. Faster R-CNN adds a Region Proposal Network (RPN) that can propose regions of interest as target object candidates, referred to as region proposals, from dense features that are computed by a convolutional network, to a RoI pooling layer which is then classified in a fully connected layer (Ren et al., 2017). The design of Faster R-CNN acts like a container, and we can replace the feature extract and learning section with any modern convolutional neural networks.

In this study, we used Residual Networks (ResNet101, He et al., 2016). The fact that RPN shares features that are calculated by the convolutional layers significantly reduces computation cost compared to R-CNN and Fast R-CNN, both of which use selective search algorithms to propose regions (Girshick et al., 2014; Ren et al., 2017). The algorithm outputs detected bounding boxes and associated probability for membership in the object of interest. We set a threshold of 0.7 to balance omissions and commissions. In practice, we selected a popular version of implementation of Mask R-CNN built on Python 3, Keras and TensorFlow (https://github.com/matterport/Mask_RCNN). Keras is a high level, human understandable, neural network library written in Python. It seals common components of neural networks in standalone modules and provides convenient tools for image and text processes, which enables fast construction of a deep neural network (https://keras.io/guides/). Mask R-CNN extends Faster R-CNN by adding a parallel branch that generates instance segmentation mask in addition to the bounding box and a class label (He et al., 2017).

The architecture of Faster R-CNN for airport detection is illustrated in Figure 4-3. The system took in training images and bounding boxes of airports in 100 epochs with 300 training steps and 50 validation steps per epoch. Training data were augmented through rotating images and annotations by 90, 180, and 270 degrees, horizontal and vertical flipping. We started from models learned from the COCO[4]

[4] COCO stands for common objects in context. COCO is a large object detection, segmentation, and captioning dataset with 80 real life object classes, 1.5 million object instances, and over 200K labeled images (http://cocodataset.org/#home).

dataset and used transfer learning to update the model on the fly. The use of pre-trained models likely addresses over-fitting problems that arise when millions of parameters are learned from scratch (Kemker et al., 2018). Convolutional layers were calculated by ResNet101 at window sizes of 4, 8, 16, 32, 64 squared pixels. A sliding window passed through the resulting convolutional feature map and generated anchors at every pixel. An anchor is a parameterized proposal that is centered at the sliding window with a scale and aspect ratio on the convolutional feature map. The original Faster R-CNN paper used three scales of 128, 256 and 512 squared pixels for an anchor in natural images (Ren et al., 2017). Chen et al. (2018) improved detection accuracy by adding a scale of 64 squared pixels for airport detection in high resolution satellite images. We calculated the statistical distribution of the width and length of airport bounding boxes in the training data, resulting in a minimum side of 26 pixels and maximum side of 576 pixels in Landsat images. Thus, we set the anchor with five scales of 32, 64, 128, 256, 512 squared pixels and 3 aspect ratios of 1:2, 1:1 and 2:1. The classification layer output two probability scores of an anchor being classified as airport or background. The regression layer outputs parameters associated with each anchor. Non-maximum suppression filtered out proposals with scores lower than 0.7. Proposals resulting from RPN along with convolutional layers were fed to the RoI pooling layer and then fully connected layers to generate a fixed-dimension feature vector for each proposal. Again, output bounding boxes of the framework were accepted for probabilities greater than 0.7.

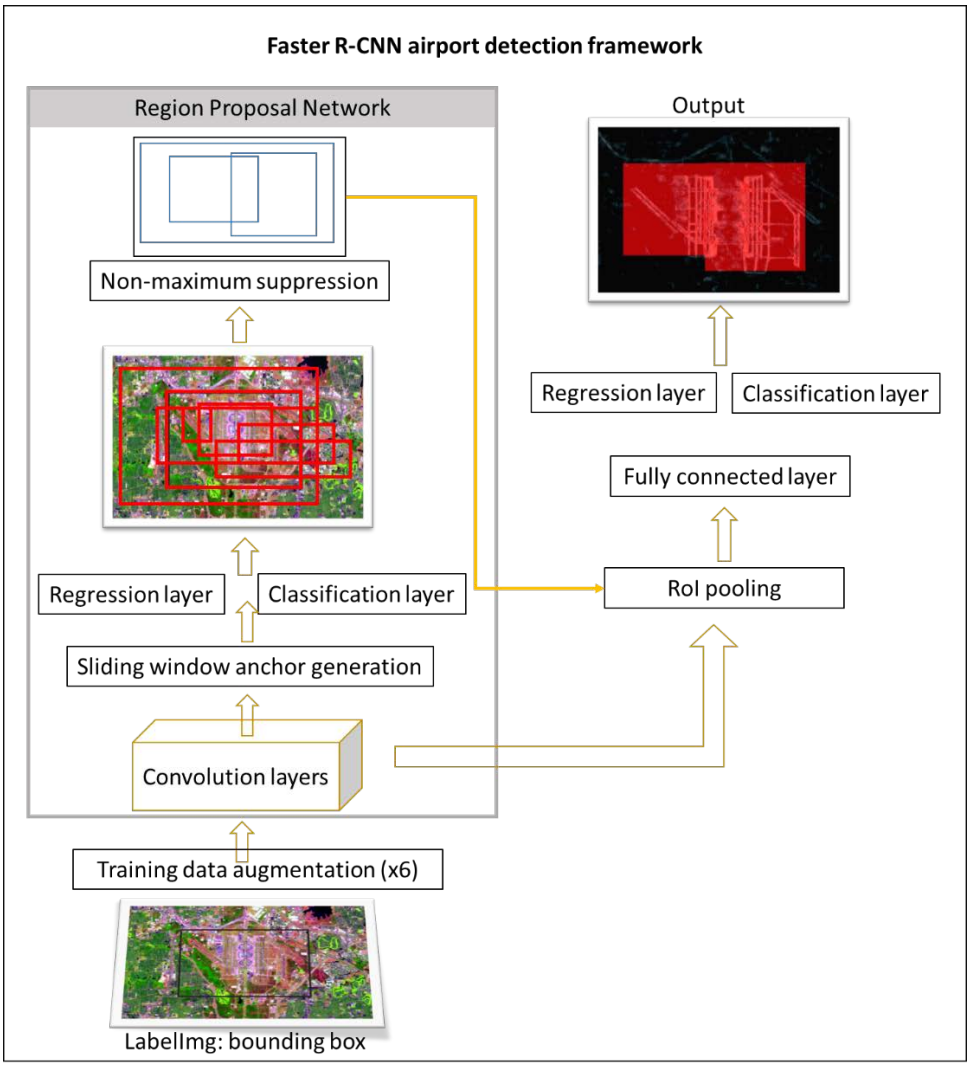

Figure 4-3 Faster R-CNN airport detection framework.

4.3.1.2 Per-pixel contexture-based U-Net

U-Net is an end-to-end fully convolutional neural network used for semantic segmentation at pixel level. It was originally developed for biomedical image segmentation and named after the "U" shape architecture design (Ronneberger et al., 2015). The architecture is symmetric where the left part down samples an input image through five convolutional layers (3x3 window, filter number was 16, 32, 64, 128 and

256 for each layer) to much smaller size to get contextual information, and the right part up samples the output of the left part to original image size through transposed convolutional layers to get localization information. Such a design makes a light and fast network and enables U-Net to handle many more bands than Faster R-CNN. We selected 27 multi-temporal statistical bands from GLAD ARD data in 2018 (Table 4-1), the gradient of which exhibited substantial contrast between airport runways and background vegetation. U-Net can learn from a small training dataset and still achieve robust results. Because U-Net puts every pixel in a class, it requires precise annotation of every airport pixel in the training data. We trained the model with annotated runway features extracted from the North America airport dataset at about 150 tiles. The output was a runway probability map of CONUS that was then fed into Faster R-CNN for another round of airport object detection.

Table 4-1 U-Net input of multi-temporal statistical feature bands from GLAD Landsat ARD dataset.

Metrics list	Statistics
Blue_av2575	Average of 25 and 75 percentile of blue band
Green_av2575	Average of 25 and 75 percentile of green band
Red_av2575	Average of 25 and 75 percentile of red band
NIR_av2575	Average of 25 and 75 percentile of near infrared band
SWIR1_av2575	Average of 25 and 75 percentile of shortwave infrared 1 band
SWIR2_av2575	Average of 25 and 75 percentile of shortwave infrared 2 band
BG_smin	Second to the minimum of the ratio of blue and green band
BG_av2575	Average of 25 and 75 percentile of the ratio of blue and green band
BN_smin	Second to the minimum of the ratio of blue and near infrared band
BN_av2575	Average of 25 and 75 percentile of the ratio of blue and near infrared band
BS1_av2575	Average of 25 and 75 percentile of the ratio of blue and shortwave infrared 1 band
RN_smin	Second to the minimum of the ratio of red and near infrared band
RN_smax	Second to the maximum of the ratio of red and near infrared band
RN_avsmin25	Average of second to the minimum and 25 percentile of the ratio of red and near infrared
RN_av2575	Average of 25 and 75 percentile of the ratio of red and near infrared
RN_av75smax	Average of 75 percentile and second to maximum of the ratio of red and near infrared

RS1_smin	Second to the minimum of the ratio of red and shortwave infrared 1 band
RS1_av2575	Average of 25 and 75 percentile of the ratio of red and shortwave infrared 1 band
RS1_avsmin25	Average of second to the minimum and 25 percentile of the ratio of red and shortwave infrared 1 band
GN_smin	Second to the minimum of the ratio of green and near infrared
GN_smax	Second to the maximum of the ratio of green and near infrared
GN_av2575	Average of 25 and 75 percentile of the ratio of green and near infrared
TCG_smin	Second to the minimum of tasseled cap greenness
TCG_min	Minimum of the tasseled cap greenness
TCW_smin	Second to the minimum of tasseled cap wetness
TCW_smax	Second to the maximum of tasseled cap wetness
red_smax_LST	Red band value corresponding to the second to the maximum land surface brightness temperature

4.3.2 Validation

Detected airports in CONUS were validated at the object level. A probability sample was selected within strata constructed by detected airport maps. Figure 4-4 illustrates the stratification design for sampling. In the aforementioned quarter degree tile system, a tile was equally divided to 0.025 x 0.025degree grids. A grid, which contains 100 x 100 pixels, is a sampling and validation unit. The resulting 1,389,300 grids were stratified by the union of airport boxes mapped by the two approaches. A grid was put in airport stratum (stratum 2) when it intersected with a mapped box, as indicated by a red dot in the center, otherwise in non-airport stratum represented by a yellow dot (stratum 1).

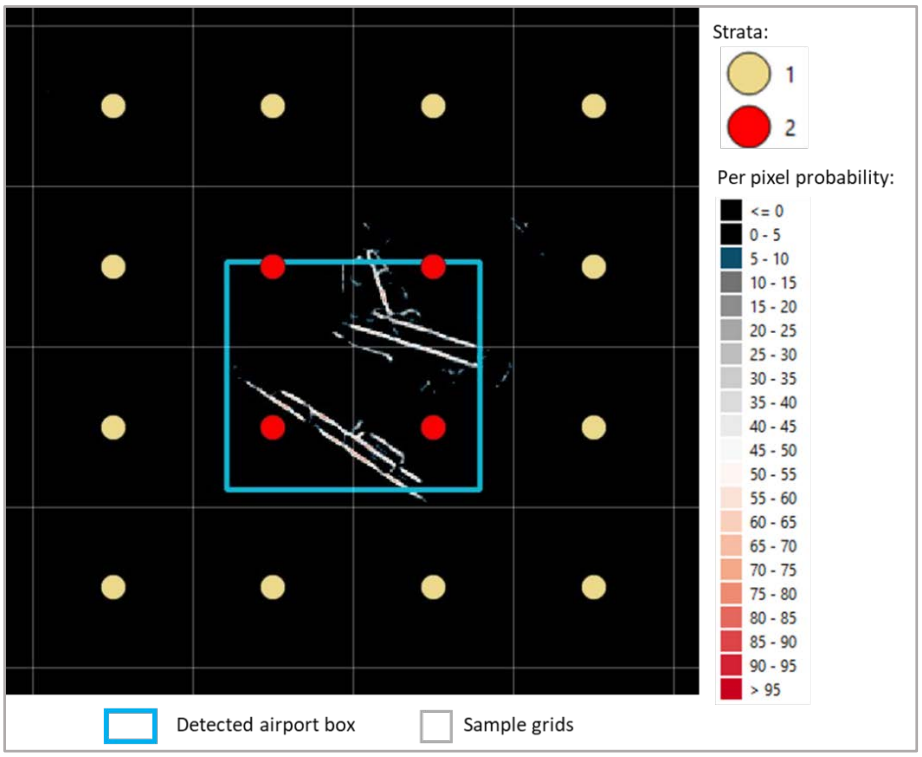

Figure 4-4 Stratification design for sampling: CONUS contains 1, 389, 300 sampling grids. The sampling grids with a centered yellow dot are in non-airport stratum (stratum 1), and those with a red dot in airport stratum (stratum 2). The blue box is

detected airport area. Background image shows per pixel airport probability predicted by U-Net.

The non-airport stratum had 1,376,288 grids, airport stratum 13,012 grids. One hundred sample grids in the airport stratum and fifty in non-airport stratum were randomly selected. Reference data were collected by interpreting sample unit with Landsat imagery and high-resolution images on Google Earth. A grid was interpreted as airport if itself or its connected grids in the airport stratum contained airport structures on the ground. Airport related structures are built-up areas that function for airport service, for example, paved runways, taxi ways, tarmac, terminals, air traffic control tower, and other associated infrastructure.

We employed equations in Chapter 2 for accuracy assessment. Two airport maps produced by the two approaches as shown in Figure 4-2 were evaluated, including the map detected merely by Faster R-CNN (Figure 4-2 output 1), the map detected by the proposed integrated approach of Faster R-CNN and U-Net (Figure 4-2 output 2).

4.4 Results

4.4.1 CONUS airports detected from Landsat imagery

The proposed integrated approach detected 1068 airports in CONUS from Landsat imagery (Figure 4-5a). The size of mapped airports varied with an average width and length of 2,875 and 2,225 meters (Table 4-2). The system was able to detect both large hub airports with multiple runways and small airports with only one runway. The proposed system was robust to different background as shown in Figure 4-5b-e with examples of correctly detected airports. The John F. Kennedy

International Airport (JFK, Figure 4-5b) sits on a waterfront surrounded by dense urban areas to the north and water to the south. The Hartfield Jackson Atlanta International Airport (ATL, Figure 4-5c) is located in a vegetated suburb of Atlanta and surrounded by highways. The Davis – Monthan Air Force Base (Figure 4-5d) is in an arid region, and many air jet parking areas are not paved. Long Beach Airport (Figure 4-5e) in California is a small primary airport sitting within a dense urban region. Linear features of airports were captured by U-Net. With a threshold of 5%, the system eliminated most artifacts from roads and riverbanks in the probability map generated by U-Net. The histogram of detected airport numbers by probability groups (Figure 4-6) shows a distribution of relatively low mid-range probabilities.

From the 100 samples in the airport stratum, 32 sample were interpreted as true airports (Table 4-3), which comprised 6% of large / medium hub airports, 84% of small / non-hub airports, 4% of other public airports, and 6% of military air force bases. We categorized airports according to the United States Federal Aviation Administration (FAA) classification system, which accounted for the number of runways, annual passenger enplanements, and usage (https://www.faa.gov/airports/planning_capacity/passenger_allcargo_stats/categories/). Large / medium hub airports represent international or national primary airports that have more than two runways and boarding passengers larger than 3.5 million in a year. Small / non-hub airports are regional or municipal primary airports that have one to two runways with boarding passengers between 10,000 and 3.5 million. Other public airports contain only one runway for nonprimary commercial service or cargo service. Air Force Bases (AFB) are for military use.

Table 4-2 Statistical size of detected airports. Height is defined as the shortest side of a detected rectangular box, width is the longest side.

Statistics	Length (m)	Width (m)
Minimum	575	1,300
Maximum	7,475	8,950
Average	2,225	2,875
Stand deviation	725	950

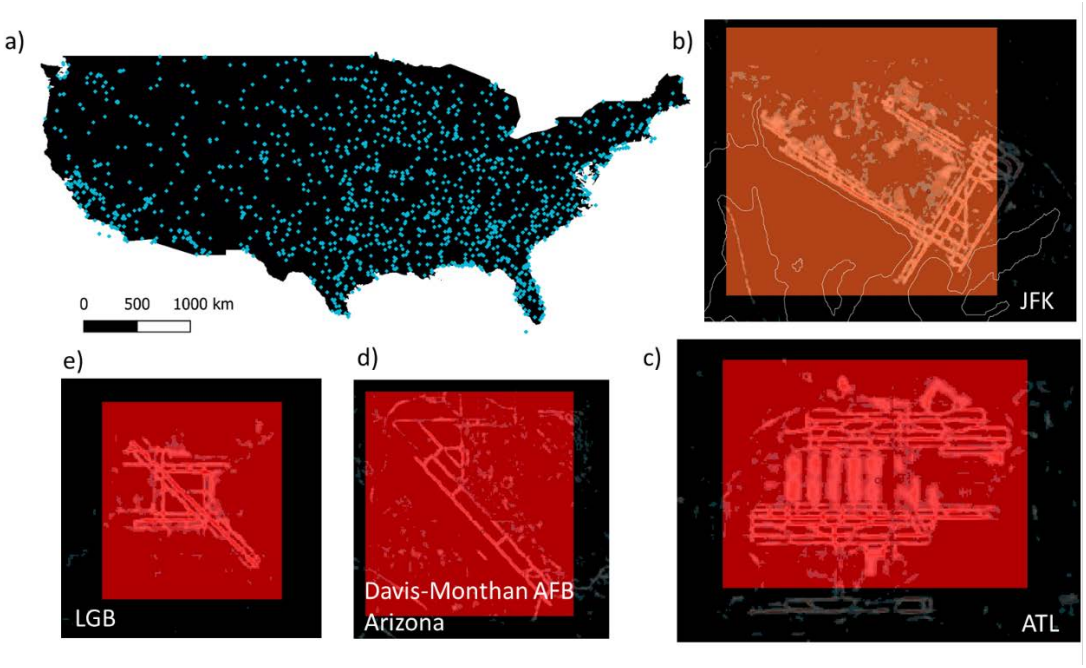

Figure 4-5 CONUS airports detected from Landsat imagery: a) Spatial distribution of 1367 mapped airports; b) Large hub John F. Kennedy International Airport in New York City; c) Large hub Hartfield Jackson Atlanta International Airport in Atlanta; d) Davis – Monthan Air Force Base in Arizona; e) Small primary airport Long Beach Airport in California. Background in b) - e) is airport probability predicted by U-Net. Bounding boxes detected by proposed system are shown in half transparent red.

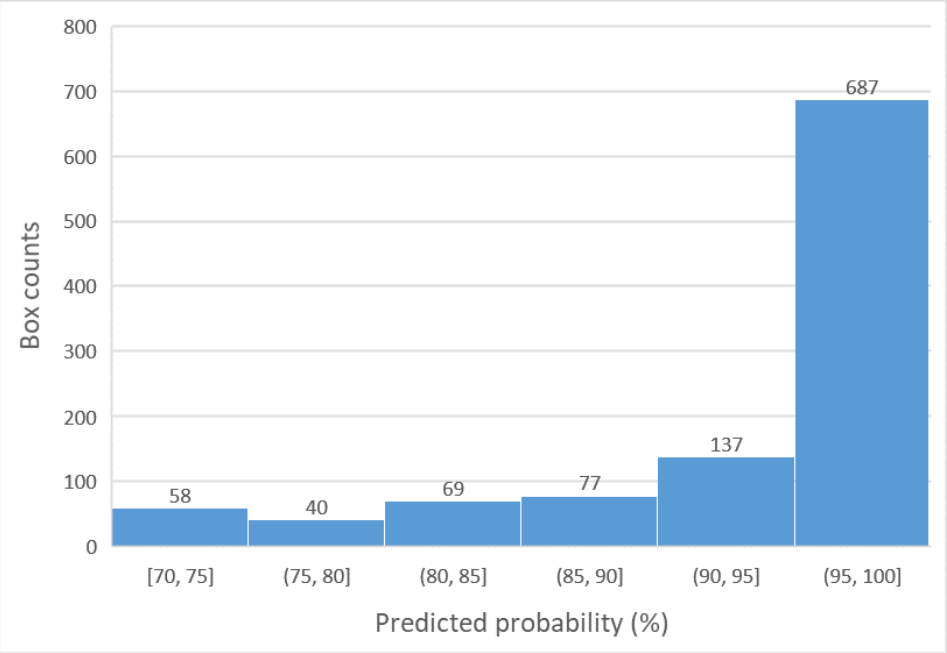

Figure 4-6 Histogram of detected airport numbers by groups of probability of a detected box being an airport predicted by the proposed system.

4.4.2 Accuracy assessment

The confusion matrix was summarized by strata (Table 4-3), for accuracy assessment of the airport maps resulted from two approaches following good practice protocols. The proposed integrated approach significantly improved user's accuracy (UA) and producer's accuracy (PA) by 60% and 19%, respectively, compared to Faster R-CNN alone (Table 4-4). The integrated approach omitted 7 out of 32 airport sample in the airport stratum (stratum 2), whereas the Faster R-CNN approach omitted 13. In the non-airport stratum (stratum 1), no sample was interpreted as airport. However, we did observe omissions comparing detected maps with training data in CONUS, which indicated overestimation of producer's accuracy for all detected maps. It is difficult to target omissions when the objects of interest occupy a tiny fraction of study area and

the map used for stratification is conservative. We attributed training airport points with information of ownership and usage (public, private or military), passenger number travelled, freight weight delivered, and departure/arrival flight numbers in the year 2019, which was downloaded from U.S. Department of Transportation (https://data-usdot.opendata.arcgis.com/datasets/airports). Our training data within CONUS represented all the airports in active public usage with passengers travelled larger than zero or freight delivered. Using active airport locations from the U.S. Department of Transportation aviation data is a possible improvement on stratification to target omissions. It is not suggested to use all the airport positions from the aviation data for stratification because 77% of the locations were labeled private airports which had a runway not detectable on Landsat, or no paved runway, or had changed to other land uses.

Table 4-3 The confusion matrix by strata of a) Faster R-CNN and b) our proposed integrated approach.

Faster R-CNN				Faster R-CNN + U-Net			
strata	**map**	**reference**		strata	**map**	**reference**	
		airport	non-airport			airport	non-airport
stratum 1	airport	0	0	stratum 1	airport	0	0
	non-airport	0	50		non-airport	0	50
stratum 2	airport	19	63	stratum 2	airport	25	5
	non-airport	13	5		non-airport	7	63

Table 4-4 Accuracy assessment of airport maps showing user's accuracy (UA), producer's accuracy (PA), and overall accuracy (OA) with standard error in parentheses.

	Approach	UA	PA	OA
Object level	Faster R-CNN	23.17 (4.66)	59.38 (8.69)	99.29 (0.04)
	Faster R-CNN + U-Net	83.33 (6.81)	78.13 (7.32)	99.89 (0.03)

Omitted airports tended to cross or be close to tile edges (Figure 4-7). The per-pixel contexture-based U-Net detected more broken runway segments in airports across tile boundaries (Figure 4-7a) than those not split by tile boundaries (Figure 4-7b). The object-based Faster R-CNN might have put higher weights in larger window set features for anchor proposals of airports with two intersected runways than those with only one runway (Figure 4-7b). One improvement to address issues with tile edges would be creating tiles overlap in between, for example, a 1000-pixel tile overlapping 250 pixels with neighbor tiles one each side. Additional spatial geometry analysis will need for integrating airports detected twice in overlapping areas. Other omissions included some small airports with one or two runways that were not well maintained. A few airports abandoned the old runway and built a new one nearby. The contrast of reflectance between runway and background grass changed with runway quality, which would affect edge feature extraction in detection algorithms, causing omissions in results.

Common commissions in both maps were attributed to parallel or intersected roads or railways, irrigation ditches, and deposited sand banks in rivers. Roads and ditches are common land features that confuse with small airfields attributed to elongated linear shape from runways (Chen et al., 2018). Detailed runway position markings, which constitute salient texture features of airports in high resolution images (Aytekin et al., 2013), are not visible in medium spatial resolution images, which also impeded the algorithms distinguishing runways from other linear features. Irrigation ditches are narrow, creating mixed pixels that are hard to distinguish even in water products generated from full Landsat time-series (Pickens et al., 2020).

Features extracted from U-Net presented patch shapes of commissions from deposited sand points, which may be caused by contours created by the gradient of soil moisture from bare land to water. The Faster R-CNN approach committed 58 more errors out of 68 non-airport sampled grids than the proposed integrated approach, which largely distributed in western mountains and the Great Plains with dominant covers of shrub, grass and cropland (Figure 4-8).

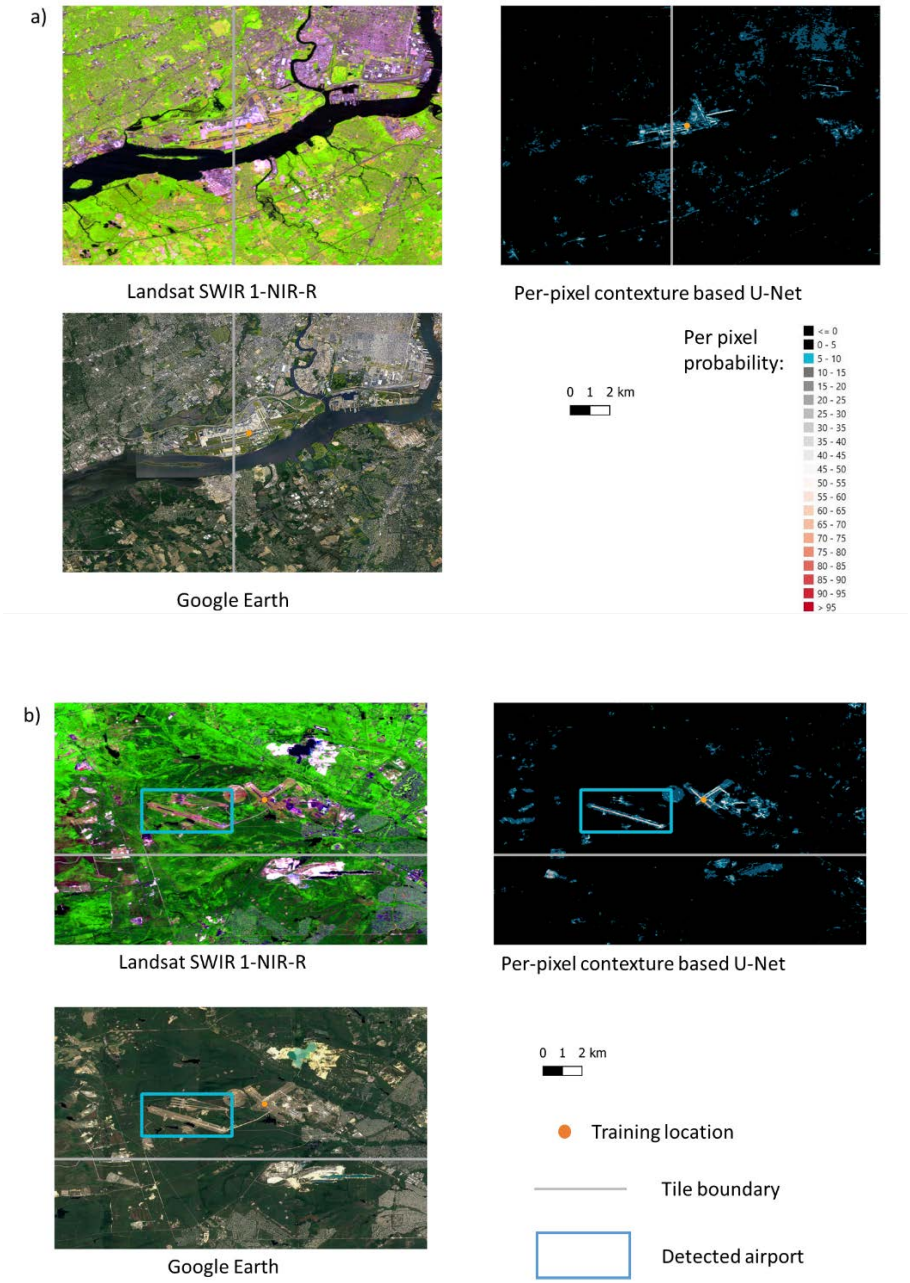

Figure 4-7 Examples of omission errors: Omitted airport a) crosses and b) near tile boundaries. An airport with one runway in inset b) was detected, whereas the right one with two intersected runways was not.

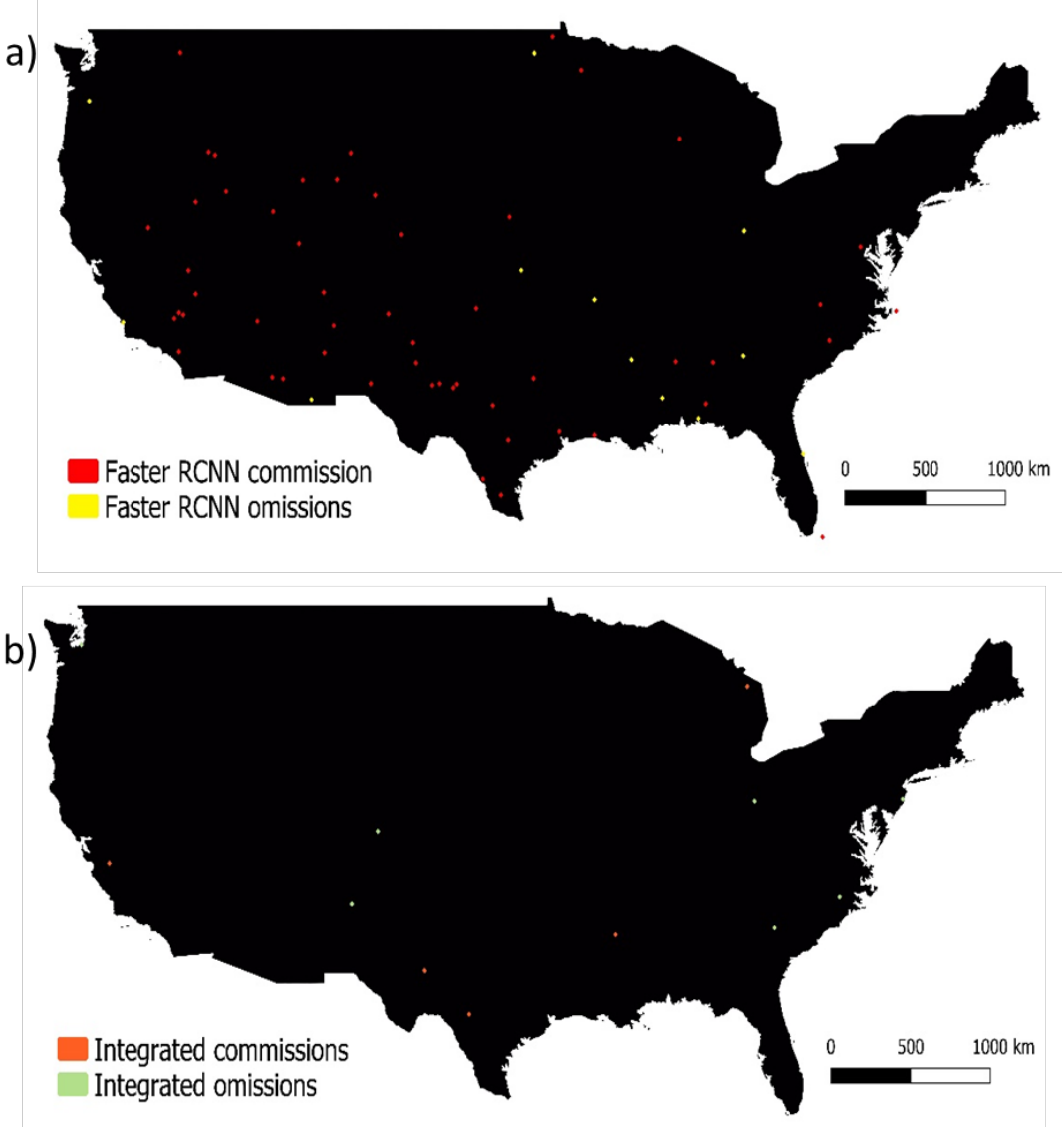

Figure 4-8 Commission and omission errors of a) Faster R-CNN and b) our proposed integrated approach.

4.5 Discussion and conclusion

This study applied an operational deep learning approach to automatically attribute airport land use in CONUS from medium resolution Landsat images. It differs from existing studies in three ways: 1) most published studies with accuracy

reports used high-resolution (<10m) satellite images, 2) their algorithms were tested on collected images contained to small land area rather than at a national scale, and 3) they reported object-based airport regions without pixel-level airport land attribution. We compared our study at the object level with those that also compared to original Faster R-CNN algorithm in their applications. Table 4-5 shows the performance of object-based Faster R-CNN applied to referenced studies. The user's and producer's accuracies of object-based Faster R-CNN in a national scale operational application (this study) were lowest compared to experiments with high-resolution imagery over small test datasets. This may be attributed to the coarser spatial resolutions of Landsat images and more omissions at tile edge associated with operational input design, but also to the national scale of implementation. Further research could re-create tiles with overlap, which may increase producer's accuracy of object-based Faster R-CNN (Chen et al., 2018).

Factors affecting the performance of Faster R-CNN include algorithm implementation, parameter setting, image resolution, training data size, annotation quality, and whether transfer learning was deployed. Chen et al. (2018) demonstrated that adding the scale and aspect ratios of anchor increased the user's accuracy of original Faster R-CNN algorithm. Based on the scale statistics of annotation boxes in training data, I added two scales for anchor proposals to Faster R-CNN. The effectiveness of the two added scales could be further tested in future experiments using annotated test data. Table 4-6 compared airport detection results from different airport detection systems presented in those studies. Compared to other studies, our proposed approach achieved the largest increase in airport-detection accuracy

compared to the original algorithm of region proposal-based CNN, and demonstrated the greatest potential for operational applications of deep learning algorithms with medium resolution images. Future work should focus on improving the infrastructure of Faster R-CNN to eliminate commission errors from roads and river banks.

Table 4-5 Evaluation of Faster R-CNN in different studies. Test airport number denoted the number of airports annotated in test dataset in existing studies. From the map product perspective, we did not have an exclusively annotated airport dataset for testing. Our reference was 32 true airport sample grids out of 150 probability sample randomly selected from map-based strata.

PA	UA	Image Resolution	Test airport #	Reference
68%	30%	8m	<170	Zhang et al., 2017
88%	84%	<10m	100	Xu et al., 2018
84%	78%	8m	149	Chen et al., 2018
59%	23%	25m	-	This study

Table 4-6 Comparison of airport detection results from improved RCNN approaches proposed in different studies.

Method	PA	UA	Reference
Line segment region proposal CNN	89%	47%	Zhang et al., 2017
Improved Faster R-CNN	92%	93%	Xu et al., 2018
Improved Faster R-CNN	84%	84%	Chen et al., 2018
Integrated Faster R-CNN and U-Net	78%	83%	This study

It may be feasible to derive land use products from Landsat imagery using deep learning algorithms. However, the contribution of multispectral bands to discerning classes are not explicitly measured in deep convolutional neural networks. For

applications of airport or road detection, a higher spatial resolution is as important as spectral bands. Applying this system with 10-meter resolution Sentinel-2 images can be done to quantify the effect of image spatial resolution on airport land use attribution.

Automatic land attribution provides spatial characterizations of land use for scientists and managers to quantify direct drivers of land cover change, to assess human impacts on ecosystems, and to evaluate economic activities. Bare ground gain is an intensive land cover changes that is 95% from human activities. The highly fragmented, small-patch nature of residential, commercial, and infrastructure development calls for algorithms that use spatial context, such as deep convolutional neural networks. Taking CONUS airports as an example, we applied a deep learning approach that combined pixel-based U-Net and object-based Faster R-CNN to assess the feasibility of automatic land attribution for large scale operations using medium resolution satellite data. Our approach significantly improved user's and producer's accuracies of original Faster R-CNN. The relatively lower producer's accuracy of our results compared to those of previous studies suggests room for improvement, however, those studies were local while ours is a national, wall-to-wall study. An overlapped tile design, improvements to the architecture of Faster R-CNN, and use of Sentinel-2 imagery offer potential improvements to our system that are primary candidates for further research.

Chapter 5 Conclusion

5.1 Summary of findings, significance and limitations

The goals of this dissertation were to advance our understanding of the magnitudes, dynamics and drivers of global bare ground gain and to discover the implications of such land cover change for global economic development monitoring through satellite observation. To achieve the research goals, I addressed three questions (see Chapter 1.2) in Chapter 2 – 4. I developed an approach to map wall-to-wall bare ground gain from Landsat imagery and then used the maps to construct strata for collecting probability samples from which I estimated unbiased areas of global, continental and national bare ground gain, with quantified uncertainties and disaggregated annual estimates by land use outcome. This was the first effort to our knowledge in existing literatures that uncovered the spatial patterns and temporal rates of global bare ground gain between 2000 and 2012 from Landsat data. Comparing temporal dynamics of different drivers of bare ground gain with economic fluctuations in business cycles measured by detrended economic variables, I investigated the relationship between bare ground gain and macro-economic change in the study period through the use of econometric models. I discovered that annual change rates of anthropogenic bare ground gain driven by the expansion of built-up area was a leading indicator for global and continental economic change in the study period dominated by the 2007-2008 global financial crisis (Ying et al., 2019). Moving forward from intensive manual interpretation of land use attributes of probability sample, I sought to test automated mapping methods for operational land use

attribution. I developed a system integrating pixel and object based deep learning algorithms to automatically characterize airports, one of the anthropogenic land uses of bare ground, for the continental United States.

5.1.1 Understanding global bare ground gain between 2000 and 2012 and discovering its implications for global economic change

Between 2000 and 2012, global bare ground area increased 93,896 km^2 (±9317 km^2 for 95% confidence interval), of which 95% was attributed to anthropogenic land uses, including 39% commercial and residential built-up, 23% resource extraction, 21% infrastructure development, 11% transitional land, and 1% greenhouses. The area gained in bare ground cover was differentially distributed, with 45% in East Asia and the Pacific and 20% in North America. South Asia and Sub-Saharan Africa, where population increase accounted for 55% of global population growth in the same period, had only 7% of global gain in bare ground area. The fact that per capita bare ground gain area in North America was 24 times higher than that in South Asia indicated different socioeconomic development rates among regions. Among the top ten countries with the largest estimates of bare ground gain area, China experienced the largest increase in bare ground area, mostly driven by commercial and residential built-up and infrastructure development. Such growth was made possible by mineral resources imported from countries such as Australia and Russia, where resource extraction was the primary driver of bare ground expansion. In return, China became the world's largest exporter of manufactured products globally. This global and domestic process of resource and product relocation facilitated Chinese urbanization,

which had shaped the scale and distribution of anthropogenic bare ground gain in China. The U.S. and Brazil were second and third on the list, largely attributed to the increase in commercial and residential built-up area. The Middle East and North Africa exhibited the highest share of commercial and residential built-up and infrastructure development combined because of urban expansion in the oil rich Gulf States.

The annual growth in bare ground area globally averaged 7881 km^2y^{-1} in the study period. Global year on year bare ground gain increased from 3,118 ± 1,132 km^2 in 2001 to a peak of 11,878 ± 2,014 km^2 in 2006 with a growth rate of 31% per year on average and fell by 60% of the peak to 4,772 ± 1,673 km^2 in 2012. The temporal trend of total bare ground gain manifested unimodal in the globe and all continental regions except Sub-Saharan Africa, with peaks from 2006 to 2008, reflecting a business cycle of growth and decline. The unimodal patterns presented in global and regional bare ground gain were driven by commercial/residential built-up, infrastructure development and transitional bare land, but peak time and change rate were different between the drivers. The expansion of commercial/residential built-up land peaked in 2006, followed by new infrastructure development with a lag of 2 to 4 years in peak time, and by transitional bare land with a shorter cycle. The spatio-temporal patterns of new commercial/residential built-up indicated the spread of global financial crises initiated from the subprime mortgage crisis in the U.S. in 2007 to substantial European debt crisis, and ultimately affecting many economic sectors globally. The trends of areas gained in infrastructure development and transitional bare land were coupled with that in commercial/residential built-up, suggesting

slower reacts of infrastructure projects rather real-estate projects to economic changes and resulted increase in transitional bare land likely due to ceased construction projects. The trends of resource extraction expansion were different from those of the three aforementioned drivers among regions due to new technologies applied to shale gas extraction in North America and other continents, price-driven gold mining in Latin America and the Caribbean, and probably structural change in energy use in some countries.

The dynamics of bare ground gain quantified in this dissertation were significant in scale (consistent and thus comparable globally for over a decade), efficiency (achievable in a timely manner with parallel computing and manageable professional efforts) with implications for a broad set of environmental studies related to the drivers of permanent vegetation loss. For example, population growth with suburban expansion was associated with increasing carbon dioxide emissions in Salt Lake metropolitan area, whereas CO_2 emissions remained stable with population growth in the established commercial and residential urban cores (Mitchell et al., 2018). The expansion of settlements and infrastructure where fossil fuel combustion provides energy were associated with new areas of resource extraction where oil, gas and coal were extracted (Le Quéré et al., 2015). With urban population being projected to account for over 64% of the world population by 2050, the estimates from this dissertation may represent a new and valuable input to modeling studies. Land use trajectories expand the human footprint and impact global carbon budgets, public health, and sustainable development in a human dominated era (Hurtt et al., 2011; IPCC, 2015).

Anthropogenic bare ground gain driven mainly by commercial/residential built-up was a significant leading indicator, by one year, of economic variables such as GDP, merchandise imports or exports, and energy use. A 10% increase in anthropogenic bare ground gain in an antecedent year is associated with a growth in the following year of 0.6% (±0.2%) for GDP, 1% (±0.3%) for merchandise imports, and 0.9% (±0.3%) for merchandise exports. Panel regression of GDP on the one-year lagged expansion of commercial/residential built-up yielded the highest coefficient of determination among all the tested time sequences of bare ground change variables. This evidence of a predictive capability in economic changes, especially in such tremendous changes as the economic boom and bust after the 2007-2008 financial crisis, is a potentially significant advance. Satellite detected gain in built-up area provided an inexpensive, consistent, and near-real time indicator of global and regional macroeconomic change, which could help policy makers, financial institutions and the public to better gauge the health of the economy and prepare for potential recessions. Moreover, uncovering the linkage between the change rates in bare ground and socioeconomic development at large scales provided insights for modeling and predicting changes in wealth and population distribution, inequity of accessing to resources, and economic vulnerability in regions and people under globalization (Weiss et al., 2018).

5.1.2 Synthesis of approaches to characterize bare land cover and land use

The overarching approach I utilized to characterize bare land cover and land use in Chapter 2 and 3 was the map-stratified sampling recommended by good practice.

Strengths of this approach include the use of unbiased estimators with quantified uncertainties, value-added attribution and timing of land cover and land use change derived from sample reference data, and high sample efficiency for a small land change class like bare ground gain compared to simple random or systematic sampling. Map-stratified sampling complements maps in terms of reporting statistically rigorous area estimates when compared to map pixel counts, particularly if the map has low accuracy. The direct change map of bare ground was very conservative, and the area counted from the map was smaller than the sample-based area. The post-characterization comparison map of bare ground yielded a closer number to the sample-based estimated area, but its spatial accuracy was lower than that of the direct change map. Though a relatively more accurate map may not result in a total area closer to the ground truth, the spatial distribution it captures can serve as a stratification that results in low uncertainty of sample-based estimates. Weaknesses of the approach include: 1) Loss of spatial explicitness: Areas estimated from map-stratified sampling are contained in geographical regions for which sufficient samples exist. With a relatively small size of sample, I was able to estimate global bare ground gain within roughly 10% uncertainty. Uncertainties grew as the scale of reporting regions went down, for example, average uncertainty reached 35% for continental estimates and over 46% for national estimates. To produce more confident estimates within smaller geographical region, a larger sample size specifically designed and selected for that region is needed; 2) Less elasticity of the sample for extended time period: The allocation of sampling units completely depends on the map used for stratification. When a new land cover change map in a

longer time period is created, i.e. the whole Landsat acquisition history, it will be hard to reuse current sample. For regions where obtaining references of sample is expensive from higher resolution or field data, how to construct strata to reuse existing samples for an extended study period will need more investigation.

Several findings on sampling design were made in this dissertation, including: 1) Map-based stratification can particularly promote sample efficiency for small classes because the map can facilitate the allocation of sample to efficiently target pixels of the class. To produce a global estimate of bare ground gain with a similar uncertainty as in Chapter 2, the sample size of simple random would be need to be more than 11 times larger. Compared to the intensive expert labor and additional data needed to obtain reference data of such sample size, map-stratified sampling provided an effective and practical approach for countries to consistently monitoring and reporting bare ground cover change. 2) Our approach to have strata that targeted both commission and omission errors resulted in robust estimates. In Chapter 2, directly and indirectly mapped bare ground gain successfully targeted commission and omission errors, respectively. However, the addition of a 90m buffer of mapped gain pixels also facilitated estimation of map omission errors. Fully 72% of omission errors were found within two pixels of a directly or indirectly mapped gain pixel. It is worth noting that the buffer stratum was 18 times larger than either of the mapped bare ground strata and contained mostly non-change pixels. The sample size allocated in buffer stratum in Chapter 2 was three times of those in mapped gain strata. Seeking an optimal allocation of samples per stratum based on current results is a worthy future task. 3) I did not find any commission errors in the non-change stratum, which

might be limited by the sample size in this stratum. The sample size in the large non-change stratum resulted from a synthesis of domain knowledge, expert experience with the map, and resources available to get reference data. Further evaluation of the optimal sample size in such a large stratum is needed.

Bare ground gain represents a very small fraction of the overall global land cover and land use extent and change, making it a difficult theme to quantify. Mapping bare ground gain from Landsat imagery is challenging due to its heterogeneous and often fine-scale nature. Mixed pixels presented substantial challenges not only to classification algorithms, but also to sample interpretation, which was also found in smallholder forest clearing compared to industrial forest loss (Tyukavina et al., 2015). The fact that 76% of commission errors and 54% of omissions were within a 1-pixel distance of real change from directly mapped bare ground gain verified the challenges that mixed pixels posed to the classification algorithm in Chapter 2.

The map accuracy in the polar climate domain was lowest due to the short growing season and low NDVI of woody vegetation and polar tundra. Unpaved roads penetrating to tropical wildness or frontier areas drove the omissions in tropical region. Those linear features were usually half or two thirds narrower than a Landsat pixel, and the forest degradation or crop expansion they resulted in were not in the scope of bare ground gain category, which created mixed pixel problems resulting in omissions at Landsat resolution scale. Arid and semi-arid landscapes, where antecedent bare ground cover was already extensive, were a major source of map errors in tropical, subtropical and temperate regions. Separate models specifically

built for arid and semi-arid regions should be evaluated in future work. New metrics derived from Landsat analysis ready data, which can better capture vegetation phenology with denser 16-day time series, might help to address such problems in the direct change detection algorithm as presented in Chapter 2. Directly mapped bare ground gain had much better accuracies than indirectly mapped gain, confirming that change detection methods that target change as a class, rather than post-characterization comparison, should be adopted in automatic mapping of land cover change. Accurately mapping of bare ground gain in large scale operations still requires attention from the research community.

Automatic land use attribution of bare ground cover merely from optical satellite images pushed the challenges to machine learning algorithms from per pixel spectral analysis to per object contextual understanding. Conventional machine learning algorithms, such as the classification tree model that was employed in Chapter 2, do not have the capability to construct advanced contextual features. Feature construction was a separate task as demonstrated in Chapter 2.3.1.1.1. Although texture features can be extracted before machine learning algorithms (Esch et al., 2017), the scale of the window size used to calculate the texture features was limited. In Chapter 4, I demonstrated the potential of applying deep learning algorithms that can generate multi-scale contextual features and learn from big training data without over fitting, in operational land use attribution. The proposed system that integrated a per pixel contexture-based U-Net and an object-based Faster R-CNN obtained better performance than the object-based Faster R-CNN alone in attributing airport land use from medium resolution satellite data. However, overlapped tile design, architecture

improvement of deep convolutional neural networks, and incorporation of higher resolution imagery are all possible avenues to improving accuracies of attributed land use products.

5.2 Future research directions

With the approach established in Chapter 2, it is feasible to obtain the dynamics of bare ground gain in the whole Landsat observation history, characterizing over forty years' worth of trajectories of permanent/semi-permanent vegetation loss globally. Chapter 3 demonstrated a decadal expansion of bare ground cover provided not only a crucial variable of global environment change, but also a leading indicator of economic development change. However, the predicting capability of bare ground gain on the economic growth and decline should be further tested in a longer time frame when the intensity and duration of economic booms and recessions varied in different business cycles. For instance, there were four recessions in the U.S. in the past forty years (1980-1982, 1990-1991, 2001, 2008-2009 according to the National Bureau of Economic Research, https://www.nber.org/cycles/), each of which was triggered with unique economic reasons and presented different durations and impacts on society. A new downturn in the economy recently is instead associated with the coronavirus pandemic. With forty years' bare ground gain quantified from Landsat imagery, questions could be addressed in the context of globalization and climate change, such as how much economic fluctuations was signaled by satellite detected bare ground gain, how socio-economic development and policies drove the dynamics of a human-dominated theme of land cover change, and what the impacts of these

changes were on local economic health and macro-economic trends. Timely estimates at global, continental, national and even regional scales are necessary for policy makers and managers to understand and assess the efficacy of policies, and to take actions for sustainable development goals (SDGs) of no poverty, reduced inequality, and sustainable cities and communities (Griggs et al., 2013; Weiss et al., 2018).

Continued efforts are required to produce accurate maps of land cover and land use change not only for offering exhaustive spatial details, but also for efficient map-stratified sampling and accurate area estimation. Unlike commodity crop expansion in South America or industrial forest clearing in Indonesia, patches of bare ground gain are usually small and scattered along environmental gradients, making it a theme that may be more accurately mapped with higher spatial resolution images like Sentinel-2. Although there is room to improve the performance of conventional machine learning algorithms, applying state-of-the-art deep learning algorithms in operational land cover and land use change mapping holds great potential, especially for land cover or land use themes or attributes that present exclusive and repeating contextual patterns. Deep learning algorithms used in image classification, segmentation and object detection are evolving very fast in the field of computer vision. Creating approaches that can adapt deep learning algorithms to multispectral and multisource satellite images is important for operational map production. Building large and standard datasets of different land cover and land use themes for training and testing models, as those created in computer vision field (Deng et al., 2009), will facilitate the application of deep learning algorithms in automated remote sensing products.

Baseline maps of attributed anthropogenic uses of bare land, such as commercial and residential built-up, infrastructure, resource extraction etc., are needed, based on which changes are updated regularly from remote sensing images similar to a forest disturbance alert system (Hansen et al., 2016). Existing products largely focused on impervious surface or urban built-up (Esch et al., 2017; Gong et al., 2020; Liu et al., 2018; Wang et al., 2017; Yang et al., 2018). However, additional land use attributions are demanded in inventories of greenhouse gases (GHG) emissions and climate change mitigation studies (IPCC, 2015). New satellite data sources, such as TanDEM-X originally designed to generate accurate digital elevation models (DEM) or the Global Ecosystem Dynamics Investigation (GEDI) for measuring ecosystem structure, can also be used to map built-up structure or help land use attribution (Dubayah et al., 2020; Esch et al., 2017; Krieger et al., 2007). Crowd-sourced geographic information from Open Street Map or Google roads greatly enriched land use attributes in human settlement areas, which can help build and test remote sensing models of mapping baseline land cover and land use (Haklay and Weber, 2008; Laurance et al., 2014). In summary, considerable and varied avenues are available to further explore the theme of bare ground gain and its utility as an indicator of human economic endeavor and development.

Appendices

Accuracy assessment formulas

The sampling design was stratified random sampling with the sampling unit defined as a Landsat pixel. A simple random sample was selected in each stratum h. The inclusion probability for pixel u in stratum h is $\pi_u = n_h/N_h$ with a stratum population size (N_h) and stratum sample size (n_h). The number of pixels in the population (i.e., region of interest) is *N*. Stehman (2014) derived the stratified estimates of accuracy using indicator functions (Cochran, 1977) y_u and x_u, where these observations obtained for pixel u have just two possible values, 0 or 1. For estimating user's accuracy of bare ground gain, define $y_u = 1$ if sample pixel u is correctly classified as bare ground gain, otherwise$y_u = 0$, and define $x_u = 1$ if sample pixel u is classified as bare ground gain, otherwise $x_u = 0$. For the producer's accuracy of bare ground gain, define $y_u = 1$ if sample pixel u is correctly classified as bare ground gain, otherwise $y_u = 0$, and define $x_u = 1$ if sample pixel u has reference class of bare ground gain, otherwise $x_u = 0$. The estimator of user's accuracy and producer's accuracy is then expressed as a ratio estimator:

$$\hat{R} = \frac{\sum_{h=1}^{25} N_h \bar{y}_h}{\sum_{h=1}^{25} N_h \bar{x}_h} \quad \text{(A1)}$$

where h is the stratum index, $\bar{y}_h = \sum_{u \in h} y_u/n_h$ is the sample mean of the y_u values in stratum h, and $\bar{x}_h$ is the sample mean of the x_u values of stratum h. The variance estimator for $\hat{R}$ is:

$$\hat{V}(\hat{R}) = \frac{1}{\hat{X}^2} \sum_{h=1}^{25} {N_h}^2 (1 - n_h/N_h)\left(s_{yh}^2 + \hat{R}^2 s_{xh}^2 - 2\hat{R} s_{xyh}\right)/n_h \quad \text{(A2)}$$

where $\hat{X} = \sum_{h=1}^{25} N_h \bar{x}_h$, s_{yh}^2 is the sample variance of the y_u values in stratum h, s_{xh}^2 is the sample variance of the x_u values within stratum h, and s_{xyh} is the sample covariance between x_u and y_u of stratum h (see Eqs. (A3) - (A5) below):

$$s_{yh}^2 = \sum_{u \in h} (y_u - \bar{y}_h)^2 / (n_h - 1) \quad \text{(A3)}$$

$$s_{xh}^2 = \sum_{u \in h} (x_u - \bar{x}_h)^2 / (n_h - 1) \quad \text{(A4)}$$

$$s_{xyh} = \sum_{u \in h} (y_u - \bar{y}_h)(x_u - \bar{x}_h) / (n_h - 1) \quad \text{(A5)}$$

To estimate overall accuracy, define $y_u = 1$ if pixel u is classified correctly and $y_u = 0$ if pixel u is classified incorrectly. The estimator for overall accuracy is then expressed as:

$$\hat{O} = \sum_{h=1}^{25} N_h \, \bar{y}_h / N \quad \text{(A6)}$$

The variance estimator for $\hat{O}$ is:

$$\hat{V}(\hat{O}) = \frac{1}{N^2} \sum_{h=1}^{25} {N_h}^2 \, (1 - n_h/N_h) \, s_{yh}^2 / n_h \quad \text{(A7)}$$

where s_{yh}^2 is computed as shown by Eq. (A3).

Bibliography

Agency, E.E., 2018. Copernicus Land Monitoring Service – High Resolution Layer Imperviousness.

Alberti, M., 2005. The effects of urban patterns on ecosystem function. Int. Reg. Sci. Rev. 28, 168–192. https://doi.org/10.1177/0160017605275160

Anderson, J.R., 1976. A Land Use and Land Cover Classification System for use with Remote Sensor Data. US Government Printing Office.

Angel, S., Parent, J., Civco, D.L., Blei, A., Potere, D., 2011. The dimensions of global urban expansion: Estimates and projections for all countries, 2000–2050. Prog. Plann. 75, 53–107. https://doi.org/10.1016/J.PROGRESS.2011.04.001

Arnold Jr, C.L., Gibbons, C.J., 1996. Impervious surface coverage: the emergence of a key environmental indicator. J. Am. Plan. Assoc. 62, 243–258.

Asner, G.P., Llactayo, W., Tupayachi, R., Luna, E.R., 2013. Elevated rates of gold mining in the Amazon revealed through high-resolution monitoring. Proc. Natl. Acad. Sci. 110, 18454–18459. https://doi.org/10.1073/pnas.1318271110

Atkinson, P.M., Jeganathan, C., Dash, J., Atzberger, C., 2012. Inter-comparison of four models for smoothing satellite sensor time-series data to estimate vegetation phenology. Remote Sens. Environ. 123, 400–417. https://doi.org/10.1016/j.rse.2012.04.001

Aytekin, Ö., Zongur, U., Halici, U., 2013. Texture-Based Airport Runway Detection. IEEE Geosci. Remote Sens. Lett. 10, 471–475. https://doi.org/10.1109/LGRS.2012.2210189

Backus, D.K., Kehoe, P.J., 1992. International Evidence on the Historical Properties of Business Cycles. Am. Econ. Rev. 82, 864–888.

Balcilar, M., 2015. Miscellaneous Time Series Filters.

Bandholz, H., Funke, M., 2003. In search of leading indicators of economic activity in Germany. J. Forecast. 22, 277–297. https://doi.org/10.1002/for.862

Barbier, E.B., 2000. Links between economic liberalization and rural resource degradation in the developing regions. Agric. Econ. 23, 299–310.

Belgiu, M., Drăgu, L., 2016. Random forest in remote sensing: A review of applications and future directions. ISPRS J. Photogramm. Remote Sens. https://doi.org/10.1016/j.isprsjprs.2016.01.011

Bennett, M.M., Smith, L.C., 2017. Advances in using multitemporal night-time lights satellite imagery to detect, estimate, and monitor socioeconomic dynamics. Remote Sens. Environ. 192, 176–197. https://doi.org/10.1016/J.RSE.2017.01.005

Blumenstock, J., Cadamuro, G., On, R., 2015. Predicting poverty and wealth from mobile phone metadata. Science (80-.). 350, 1073–1076. https://doi.org/10.1126/science.aac4420

Bonan, G.B., Pollard, D., Thompson, S.L., 1992. Effects of boreal Forest Vegetation on Global Climate. Nature 359, 716–718. https://doi.org/10.1038/359716a0

Breiman, L., 1996. Bagging predictors. Mach. Learn. 24, 123–140.

Breiman, L., Friedman, J., Stone, C.J., Olshen, R.A., 1984. Classification and Regression Trees. CRC press.

Bridge, G., 2004. Contested terrain: mining and the environment. Annu. Rev.

Environ. Resour. 29, 205–259.

Broich, M., Stehman, S. V, Hansen, M.C., Potapov, P., Shimabukuro, Y.E., 2009. A comparison of sampling designs for estimating deforestation from Landsat imagery: a case study of the Brazilian Legal Amazon. Remote Sens. Environ. 113, 2448–2454.

Chander, G., Markham, B.L., Helder, D.L., 2009. Summary of current radiometric calibration coefficients for Landsat MSS, TM, ETM+, and EO-1 ALI sensors. Remote Sens. Environ. 113, 893–903. https://doi.org/10.1016/j.rse.2009.01.007

Chen, F., Ren, R., Van de Voorde, T., Xu, W., Zhou, G., Zhou, Y., 2018. Fast automatic airport detection in remote sensing images using convolutional neural networks. Remote Sens. 10, 443.

Chen, J., Guo, F., Wu, Y., 2011. One decade of urban housing reform in China: Urban housing price dynamics and the role of migration and urbanization, 1995–2005. Habitat Int. 35, 1–8. https://doi.org/10.1016/J.HABITATINT.2010.02.003

Chen, X., Nordhaus, W.D., 2011. Using luminosity data as a proxy for economic statistics. Proc. Natl. Acad. Sci. 108, 8589–8594. https://doi.org/10.1073/pnas.1017031108

Cochran, W.G., 1977. Sampling Techniques, third ed. John Wiley& Sons, New York.

Commission, U.N.S., 2009. System of National Accounts 2008. Eur. Communities, Int. Monet. Fund, Organ. Econ. Co-operation Dev. United Nations World Bank, New York.

Conti, S., Meli, P., Minelli, G., Solimini, R., Toccaceli, V., Vichi, M., Beltrano, C., Perini, L., 2005. Epidemiologic study of mortality during the Summer 2003 heat

wave in Italy. Environ. Res. 98, 390–399. https://doi.org/https://doi.org/10.1016/j.envres.2004.10.009

Coppin, P., Jonckheere, I., Nackaerts, K., Muys, B., Lambin, E., 2004. Digital change detection methods in ecosystem monitoring: a review. Int. J. Remote Sens. 25, 1565–1596. https://doi.org/10.1080/0143116031000101675

Croissant, Y., Millo, G., 2008. Panel Data Econometrics in R : The plm Package. J. Stat. Softw. 27, 1–43. https://doi.org/10.18637/jss.v027.i02

Curtis, P.G., Slay, C.M., Harris, N.L., Tyukavina, A., Hansen, M.C., 2018. Classifying drivers of global forest loss. Science (80-.). 361, 1108–1111. https://doi.org/10.1126/science.aau3445

DeFries, R.S., Rudel, T., Uriarte, M., Hansen, M., 2010. Deforestation driven by urban population growth and agricultural trade in the twenty-first century. Nat. Geosci. 3, 178–181. https://doi.org/10.1038/ngeo756

Deng, J., Dong, W., Socher, R., Li, L.-J., Li, K., Fei-Fei, L., 2009. Imagenet: A large-scale hierarchical image database, in: 2009 IEEE Conference on Computer Vision and Pattern Recognition. Ieee, pp. 248–255.

Dhakal, S., 2010. GHG emissions from urbanization and opportunities for urban carbon mitigation. Curr. Opin. Environ. Sustain. 2, 277–283. https://doi.org/https://doi.org/10.1016/j.cosust.2010.05.007

Dubayah, R., Blair, J.B., Goetz, S., Fatoyinbo, L., Hansen, M., Healey, S., Hofton, M., Hurtt, G., Kellner, J., Luthcke, S., Armston, J., Tang, H., Duncanson, L., Hancock, S., Jantz, P., Marselis, S., Patterson, P.L., Qi, W., Silva, C., 2020. The Global Ecosystem Dynamics Investigation: High-resolution laser ranging of the

Earth’s forests and topography. Sci. Remote Sens. 1, 100002. https://doi.org/https://doi.org/10.1016/j.srs.2020.100002

Dwyer, J.L., Roy, D.P., Sauer, B., Jenkerson, C.B., Zhang, H.K., Lymburner, L., 2018. Analysis ready data: Enabling analysis of the landsat archive. Remote Sens. 10, 1363. https://doi.org/10.3390/rs10091363

Eagle, N., Macy, M., Claxton, R., 2010. Network diversity and economic development. Science (80-.). 328, 1029–1031. https://doi.org/10.1126/science.1186605

Ellis, E.C., Ramankutty, N., 2008. Putting people in the map: anthropogenic biomes of the world. Front. Ecol. Environ. 6, 439–447. https://doi.org/10.1890/070062

Elvidge, C.D., Baugh, K.E., Kihn, E.A., Kroehl, H.W., Davis, E.R., Davis, C.W., 1997. Relation between satellite observed visible-near infrared emissions, population, economic activity and electric power consumption. Int. J. Remote Sens. 18, 1373–1379. https://doi.org/10.1080/014311697218485

Esch, T., Heldens, W., Hirner, A., Keil, M., Marconcini, M., Roth, A., Zeidler, J., Dech, S., Strano, E., 2017. Breaking new ground in mapping human settlements from space – The Global Urban Footprint. ISPRS J. Photogramm. Remote Sens. 134, 30–42. https://doi.org/10.1016/j.isprsjprs.2017.10.012

Falk, T., Mai, D., Bensch, R., Çiçek, Ö., Abdulkadir, A., Marrakchi, Y., Böhm, A., Deubner, J., Jäckel, Z., Seiwald, K., 2019. U-Net: deep learning for cell counting, detection, and morphometry. Nat. Methods 16, 67–70.

Feng, M., Sexton, J.O., Huang, C., Anand, A., Channan, S., Song, X.-P., Song, D.-X., Kim, D.-H., Noojipady, P., Townshend, J.R., 2016. Earth Science Data Records

of Global Forest Cover and Change: Assessment of Accuracy in 1990, 2000, and 2005 epochs. Remote Sens. Environ. 184, In press. https://doi.org/10.1016/j.rse.2016.06.012

Flanagan, W., McIntosh, C.N., Le Petit, C., Berthelot, J.-M., 2006. Deriving utility scores for co-morbid conditions: a test of the multiplicative model for combining individual condition scores. Popul. Health Metr. 4, 13. https://doi.org/10.1186/1478-7954-4-13

Foley, J.A., DeFries, R., Asner, G.P., Barford, C., Bonan, G., Carpenter, S.R., Chapin, F.S., Coe, M.T., Daily, G.C., Gibbs, H.K., Helkowski, J.H., Holloway, T., Howard, E.A., Kucharik, C.J., Monfreda, C., Patz, J.A., Prentice, I.C., Ramankutty, N., Snyder, P.K., 2005. Global consequences of land use. Science (80-.). 309, 570–574. https://doi.org/10.1126/science.1111772

Founda, D., Santamouris, M., 2017. Synergies between Urban Heat Island and Heat Waves in Athens (Greece), during an extremely hot summer (2012). Sci. Rep. 7, 10973. https://doi.org/10.1038/s41598-017-11407-6

Friedl, M.A., Brodley, C.E., 1997. Decision tree classification of land cover from remotely sensed data. Remote Sens. Environ. 61, 399–409. https://doi.org/10.1016/S0034-4257(97)00049-7

Friedl, M.A., McIver, D.K., Hodges, J.C.F., Zhang, X.Y., Muchoney, D., Strahler, A.H., Woodcock, C.E., Gopal, S., Schneider, A., Cooper, A., Baccini, A., Gao, F., Schaaf, C., 2002. Global land cover mapping from MODIS: algorithms and early results. Remote Sens. Environ. 83, 287–302.

Friedl, M.A., Sulla-Menashe, D., Tan, B., Schneider, A., Ramankutty, N., Sibley, A.,

Huang, X., 2010. MODIS Collection 5 global land cover: Algorithm refinements and characterization of new datasets. Remote Sens. Environ. 114, 168–182. https://doi.org/10.1016/j.rse.2009.08.016

Fritz, S., McCallum, I., Schill, C., Perger, C., Grillmayer, R., Achard, F., Kraxner, F., Obersteiner, M., 2009. Geo-Wiki.Org: the use of crowdsourcing to improve global land cover. Remote Sens. 1, 345–354. https://doi.org/10.3390/rs1030345

Frolking, S., Milliman, T., Seto, K.C., Friedl, M.A., 2013. A global fingerprint of macro-scale changes in urban structure from 1999 to 2009. Environ. Res. Lett. 8, 024004. https://doi.org/10.1088/1748-9326/8/2/024004

Fu, C., Song, X.-P., Stewart, K., 2019. Integrating Activity-Based Geographic Information and Long-Term Remote Sensing to Characterize Urban Land Use Change. Remote Sens. 11, 2965. https://doi.org/10.3390/rs11242965

Geist, H.J., Lambin, E.F., 2002. Proximate causes and underlying driving forces of tropical deforestation. Bioscience 52, 143–150. https://doi.org/10.1641/0006-3568(2002)052[0143:pcaudf]2.0.co;2

Girshick, R., Donahue, J., Darrell, T., Malik, J., 2014. Rich feature hierarchies for accurate object detection and semantic segmentation, in: Proceedings of the IEEE Conference on Computer Vision and Pattern Recognition. pp. 580–587.

Gómez, C., White, J.C., Wulder, M.A., 2016. Optical remotely sensed time series data for land cover classification: A review. ISPRS J. Photogramm. Remote Sens. https://doi.org/10.1016/j.isprsjprs.2016.03.008

Gong, P., Li, X., Wang, J., Bai, Y., Chen, B., Hu, T., Liu, X., Xu, B., Yang, J., Zhang, W., Zhou, Y., 2020. Annual maps of global artificial impervious area (GAIA)

between 1985 and 2018. Remote Sens. Environ. 236, 111510. https://doi.org/10.1016/j.rse.2019.111510

Gong, P., Wang, J., Yu, Le, Zhao, Yongchao, Zhao, Yuanyuan, Liang, L., Niu, Z., Huang, X., Fu, H., Liu, S., Li, C., Li, X., Fu, W., Liu, C., Xu, Y., Wang, X., Cheng, Q., Hu, L., Yao, W., Zhang, Han, Zhu, P., Zhao, Z., Zhang, Haiying, Zheng, Y., Ji, L., Zhang, Y., Chen, H., Yan, A., Guo, J., Yu, Liang, Wang, L., Liu, X., Shi, T., Zhu, M., Chen, Y., Yang, G., Tang, P., Xu, B., Giri, C., Clinton, N., Zhu, Z., Chen, Jin, Chen, Jun, 2013. Finer resolution observation and monitoring of global land cover: first mapping results with Landsat TM and ETM+ data. Int. J. Remote Sens. 34, 2607–2654. https://doi.org/10.1080/01431161.2012.748992

Gorelick, N., Hancher, M., Dixon, M., Ilyushchenko, S., Thau, D., Moore, R., 2017. Google Earth Engine: Planetary-scale geospatial analysis for everyone. Remote Sens. Environ. 202, 18–27. https://doi.org/10.1016/J.RSE.2017.06.031

Griggs, D., Stafford-Smith, M., Gaffney, O., Rockström, J., Öhman, M.C., Shyamsundar, P., Steffen, W., Glaser, G., Kanie, N., Noble, I., 2013. Sustainable development goals for people and planet. Nature 495, 305–307. https://doi.org/10.1038/495305a

Grimm, N.B., Grimm, N.B., Faeth, S.H., Golubiewski, N.E., Redman, C.L., Wu, J., Bai, X., Briggs, J.M., Grimm, N.B., Faeth, S.H., Golubiewski, N.E., Redman, C.L., Wu, J., Bai, X., Briggs, J.M., 2008. Global change and the ecology of cities. Science 319, 756–760. https://doi.org/10.1126/science.1150195

Haklay, M., Weber, P., 2008. OpenStreetMap: User-generated street maps. IEEE

Pervasive Comput. 7, 12–18.

Hand, E., 2015. Startup liftoff. Science 348, 172–7. https://doi.org/10.1126/science.348.6231.172

Hansen, M.C., 2012. Classification trees and mixed pixel training data. Remote Sens. L. Use L. Cover Princ. Appl. 127–136.

Hansen, M.C., DeFries, R.S., Townshend, J.R.G., Carroll, M., Dimiceli, C., Sohlberg, R.A., 2003. Global percent tree cover at a spatial resolution of 500 meters: First results of the MODIS vegetation continuous fields algorithm. Earth Interact. 7, 1–15.

Hansen, M.C., Defries, R.S., Townshend, J.R.G., Sohlberg, R., 2000. Global land cover classification at 1km spatial resolution using a classification tree approach. Int. J. Remote Sens. 21, 1331–1364. https://doi.org/10.1080/014311600210209

Hansen, M.C., Egorov, A., Potapov, P. V, Stehman, S. V, Tyukavina, A., Turubanova, S.A., Roy, D.P., Goetz, S.J., Loveland, T.R., Ju, J., Kommareddy, A., Kovalskyy, V., Forsyth, C., Bents, T., 2014. Monitoring conterminous United States (CONUS) land cover change with Web-Enabled Landsat Data (WELD). Remote Sens. Environ. 140, 466–484. https://doi.org/10.1016/j.rse.2013.08.014

Hansen, M.C., Egorov, A., Roy, D.P., Potapov, P., Ju, J.C., Turubanova, S., Kommareddy, I., Loveland, T.R., 2011. Continuous fields of land cover for the conterminous United States using Landsat data: first results from the Web-Enabled Landsat Data (WELD) project. Remote Sens. Lett. 2, 279–288. https://doi.org/10.1080/01431161.2010.519002

Hansen, M.C., Krylov, A., Tyukavina, A., Potapov, P. V, Turubanova, S., Zutta, B., Ifo, S., Margono, B., Stolle, F., Moore, R., 2016. Humid tropical forest disturbance alerts using Landsat data. Environ. Res. Lett. 11, 034008. https://doi.org/10.1088/1748-9326/11/3/034008

Hansen, M.C., Loveland, T.R., 2012. A review of large area monitoring of land cover change using Landsat data. Remote Sens. Environ. 122, 66–74. https://doi.org/http://dx.doi.org/10.1016/j.rse.2011.08.024

Hansen, M. C., Potapov, P. V., Moore, R., Hancher, M., Turubanova, S.A., Tyukavina, A., Thau, D., Stehman, S. V., Goetz, S.J., Loveland, T.R., Kommareddy, A., Egorov, A., Chini, L., Justice, C.O., Townshend, J.R.G., 2013. High-Resolution Global Maps of 21st-Century Forest Cover Change. Science (80-.). 342, 850–853. https://doi.org/10.1126/science.1244693

Hansen, M C, Potapov, P. V, Moore, R., Hancher, M., Turubanova, S.A., Tyukavina, A., Thau, D., Stehman, S. V, Goetz, S.J., Loveland, T.R., Kommareddy, A., Egorov, A., Chini, L., Justice, C.O., Townshend, J.R.G., 2013. High-resolution global maps of 21st-century forest cover change. Science (80-.). 342, 850–853.

Hansen, M.C., Roy, D.P., Lindquist, E., Adusei, B., Justice, C.O., Altstatt, A., 2008. A method for integrating MODIS and Landsat data for systematic monitoring of forest cover and change in the Congo Basin. Remote Sens. Environ. 112, 2495–2513. https://doi.org/10.1016/j.rse.2007.11.012

Hansen, M.C., Stehman, S. V, Potapov, P. V, 2010. Quantification of global gross forest cover loss. Proc. Natl. Acad. Sci. 107, 8650–8655. https://doi.org/10.1073/pnas.0912668107

He, C., Liu, Z., Gou, S., Zhang, Q., Zhang, J., Xu, L., 2019. Detecting global urban expansion over the last three decades using a fully convolutional network. Environ. Res. Lett. 14. https://doi.org/10.1088/1748-9326/aaf936

He, K., Gkioxari, G., Dollár, P., Girshick, R., 2017. Mask r-cnn, in: Proceedings of the IEEE International Conference on Computer Vision. pp. 2961–2969.

He, K., Zhang, X., Ren, S., Sun, J., 2016. Deep residual learning for image recognition, in: Proceedings of the IEEE Conference on Computer Vision and Pattern Recognition. pp. 770–778.

Helber, P., Bischke, B., Dengel, A., Borth, D., 2019. Eurosat: A novel dataset and deep learning benchmark for land use and land cover classification. IEEE J. Sel. Top. Appl. Earth Obs. Remote Sens. 12, 2217–2226. https://doi.org/10.1109/JSTARS.2019.2918242

Henderson, J.V., Storeygard, A., Weil, D.N., 2012. Measuring Economic Growth from Outer Space. Am. Econ. Rev. 102, 994–1028. https://doi.org/10.1257/aer.102.2.994

Hodrick, R.J., Prescott, E.C., 1997. Postwar U . S . Business Cycles : An Empirical Investigation. J. Money, Credit Bank. 29, 1–16.

Homer, C., Huang, C.Q., Yang, L.M., Wylie, B., Coan, M., 2004. Development of a 2001 National Land-Cover Database for the United States. Photogramm. Eng. Remote Sensing 70, 829–840.

Hosonuma, N., Herold, M., De Sy, V., De Fries, R.S., Brockhaus, M., Verchot, L., Angelsen, A., Romijn, E., 2012. An assessment of deforestation and forest degradation drivers in developing countries. Environ. Res. Lett. 7, 44009.

Huang, M.Y., Rojas, R.R., Convery, P.D., 2018. News Sentiment as Leading Indicators for Recessions.

Hurtt, G.C., Chini, L.P., Frolking, S., Betts, R.A., Feddema, J., Fischer, G., Fisk, J.P., Hibbard, K., Houghton, R.A., Janetos, A., Jones, C.D., Kindermann, G., Kinoshita, T., Goldewijk, K.K., Riahi, K., Shevliakova, E., Smith, S., Stehfest, E., Thomson, A., Thornton, P., van Vuuren, D.P., Wang, Y.P., 2011. Harmonization of land-use scenarios for the period 1500-2100: 600 years of global gridded annual land-use transitions, wood harvest, and resulting secondary lands. Clim. Change 109, 117–161. https://doi.org/10.1007/s10584-011-0153-2

Ibisch, P.L., Hoffmann, M.T., Kreft, S., Pe'er, G., Kati, V., Biber-Freudenberger, L., DellaSala, D.A., Vale, M.M., Hobson, P.R., Selva, N., 2016. A global map of roadless areas and their conservation status. Science (80-.). 354, 1423 LP – 1427. https://doi.org/10.1126/science.aaf7166

IPCC, 2015. Climate Change 2014: Mitigation of Climate Change. Cambridge University Press, Cambridge, United Kingdom and New York, NY, USA.

Jean, N., Burke, M., Xie, M., Davis, W.M., Lobell, D.B., Ermon, S., 2016. Combining satellite imagery and machine learning to predict poverty. Science (80-.). 353, 790–794. https://doi.org/10.1126/science.aaf7894

Jin, S., Yang, L., Danielson, P., Homer, C., Fry, J., Xian, G., 2013. A comprehensive change detection method for updating the National Land Cover Database to circa 2011. Remote Sens. Environ. 132, 159–175.

Kalnay, E., Cai, M., 2003. Impact of urbanization and land-use change on climate.

Nature 423, 528–531. https://doi.org/10.1038/nature01675

Kemker, R., Salvaggio, C., Kanan, C., 2018. Algorithms for semantic segmentation of multispectral remote sensing imagery using deep learning. ISPRS J. Photogramm. Remote Sens. 145, 60–77. https://doi.org/https://doi.org/10.1016/j.isprsjprs.2018.04.014

Kennedy, C., Pincetl, S., Bunje, P., 2011. The study of urban metabolism and its applications to urban planning and design. Environ. Pollut. 159, 1965–1973. https://doi.org/https://doi.org/10.1016/j.envpol.2010.10.022

Khorram, S., 1999. Accuracy Assessment of Remote Sensing-derived Change Detection. American Society for Photogrammetry and Remote Sensing, Bethesda, Md.

Kovalskyy, V., Roy, D.P., 2013. The global availability of Landsat 5 TM and Landsat 7 ETM + land surface observations and implications for global 30 m Landsat data product generation. Remote Sens. Environ. 130, 280–293. https://doi.org/10.1016/j.rse.2012.12.003

Krieger, G., Moreira, A., Fiedler, H., Hajnsek, I., Werner, M., Younis, M., Zink, M., 2007. TanDEM-X: A satellite formation for high-resolution SAR interferometry. IEEE Trans. Geosci. Remote Sens. 45, 3317–3341.

Kussul, N., Lavreniuk, M., Skakun, S., Shelestov, A., 2017. Deep Learning Classification of Land Cover and Crop Types Using Remote Sensing Data. IEEE Geosci. Remote Sens. Lett. 14, 778–782. https://doi.org/10.1109/LGRS.2017.2681128

Lambin, E.F., Geist, H.J., Lepers, E., 2003. Dynamics of land-use and land-cover

change in tropical regions. Annu. Rev. Environ. Resour. 28, 205–241. https://doi.org/10.1146/annurev.energy.28.050302.105459

Lambin, E.F., Meyfroidt, P., 2011. Global land use change, economic globalization, and the looming land scarcity. Proc. Natl. Acad. Sci. 108, 3465–3472. https://doi.org/10.1073/pnas.1100480108

Laurance, W.F., Clements, G.R., Sloan, S., O'Connell, C.S., Mueller, N.D., Goosem, M., Venter, O., Edwards, D.P., Phalan, B., Balmford, A., Van Der Ree, R., Arrea, I.B., 2014. A global strategy for road building. Nature 513, 229–232. https://doi.org/10.1038/nature13717

Le Quéré, C., Moriarty, R., Andrew, R.M., Canadell, J.G., Sitch, S., Korsbakken, J.I., Friedlingstein, P., Peters, G.P., Andres, R.J., Boden, T.A., 2015. Global carbon budget 2015. Earth Syst. Sci. Data 7, 349–396.

LeCun, Y., Bengio, Y., Hinton, G., 2015. Deep learning. Nature 521, 436–444.

Li, L., Goodchild, M.F., Xu, B., 2013. Spatial, temporal, and socioeconomic patterns in the use of Twitter and Flickr. Cartogr. Geogr. Inf. Sci. 40, 61–77. https://doi.org/10.1080/15230406.2013.777139

Li, P., Ren, P., Zhang, X., Wang, Q., Zhu, X., Wang, L., 2018. Region-wise deep feature representation for remote sensing images. Remote Sens. 10, 871.

Li, R., Liu, W., Yang, L., Sun, S., Hu, W., Zhang, F., Li, W., 2018. DeepUNet: A Deep Fully Convolutional Network for Pixel-Level Sea-Land Segmentation. IEEE J. Sel. Top. Appl. Earth Obs. Remote Sens. 11, 3954–3962. https://doi.org/10.1109/JSTARS.2018.2833382

Liu, F., Wang, S., Xu, Y., Ying, Q., Yang, F., Qin, Y., 2020. Accuracy assessment of

Global Human Settlement Layer (GHSL) built-up products over China. PLoS One 15, e0233164.

Liu, X., Hu, G., Chen, Y., Li, X., Xu, X., Li, S., Pei, F., Wang, S., 2018. High-resolution multi-temporal mapping of global urban land using Landsat images based on the Google Earth Engine Platform. Remote Sens. Environ. 209, 227–239. https://doi.org/https://doi.org/10.1016/j.rse.2018.02.055

Liu, X., Lathrop, J.G., 2002. Urban change detection based on an artificial neural network. Int. J. Remote Sens. 23, 2513–2518. https://doi.org/10.1080/01431160110097240

Liu, Y., Liu, X., Gao, S., Gong, L., Kang, C., Zhi, Y., Chi, G., Shi, L., 2015. Social Sensing: A New Approach to Understanding Our Socioeconomic Environments. Ann. Assoc. Am. Geogr. 105, 512–530. https://doi.org/10.1080/00045608.2015.1018773

Loveland, T.R., Reed, B.C., Brown, J.F., Ohlen, D.O., Zhu, Z., Yang, L., Merchant, J.W., 2000. Development of a global land cover characteristics database and IGBP DISCover from 1 km AVHRR data. Int. J. Remote Sens. 21, 1303–1330. https://doi.org/10.1080/014311600210191

Lu, D., Weng, Q., 2006. Use of impervious surface in urban land-use classification. Remote Sens. Environ. 102, 146–160.

Ma, L., Liu, Y., Zhang, X., Ye, Y., Yin, G., Johnson, B.A., 2019. Deep learning in remote sensing applications: A meta-analysis and review. ISPRS J. Photogramm. Remote Sens. 152, 166–177. https://doi.org/https://doi.org/10.1016/j.isprsjprs.2019.04.015

Marcotullio, P.J., Sarzynski, A., Albrecht, J., Schulz, N., Garcia, J., 2013. The geography of global urban greenhouse gas emissions: an exploratory analysis. Clim. Change 121, 621–634. https://doi.org/10.1007/s10584-013-0977-z

McDonald, B.C., de Gouw, J.A., Gilman, J.B., Jathar, S.H., Akherati, A., Cappa, C.D., Jimenez, J.L., Lee-Taylor, J., Hayes, P.L., McKeen, S.A., Cui, Y.Y., Kim, S.-W., Gentner, D.R., Isaacman-VanWertz, G., Goldstein, A.H., Harley, R.A., Frost, G.J., Roberts, J.M., Ryerson, T.B., Trainer, M., 2018. Volatile chemical products emerging as largest petrochemical source of urban organic emissions. Science (80-.). 359, 760 LP – 764. https://doi.org/10.1126/science.aaq0524

Mellander, C., Lobo, J., Stolarick, K., Matheson, Z., 2015. Night-Time Light Data: A Good Proxy Measure for Economic Activity? PLoS One 10, e0139779. https://doi.org/10.1371/journal.pone.0139779

Mitchell, L.E., Lin, J.C., Bowling, D.R., Pataki, D.E., Strong, C., Schauer, A.J., Bares, R., Bush, S.E., Stephens, B.B., Mendoza, D., Mallia, D., Holland, L., Gurney, K.R., Ehleringer, J.R., 2018. Long-term urban carbon dioxide observations reveal spatial and temporal dynamics related to urban characteristics and growth. Proc. Natl. Acad. Sci. 115, 2912 LP – 2917. https://doi.org/10.1073/pnas.1702393115

Mok, K.Y., Shen, G.Q., Yang, J., 2015. Stakeholder management studies in mega construction projects: A review and future directions. Int. J. Proj. Manag. 33, 446–457. https://doi.org/10.1016/J.IJPROMAN.2014.08.007

Moran, M.S., Rahman, A.F., Washburne, J.C., Goodrich, D.C., Weltz, M.A., Kustas, W.P., 1996. Combining the Penman-Monteith equation with measurements of

surface temperature and reflectance to estimate evaporation rates of semiarid grassland. Agric. For. Meteorol. 80, 87–109. https://doi.org/10.1016/0168-1923(95)02292-9

Mountrakis, G., Im, J., Ogole, C., 2011. Support vector machines in remote sensing: A review. ISPRS J. Photogramm. Remote Sens. https://doi.org/10.1016/j.isprsjprs.2010.11.001

Najafabadi, M.M., Villanustre, F., Khoshgoftaar, T.M., Seliya, N., Wald, R., Muharemagic, E., 2015. Deep learning applications and challenges in big data analytics. J. Big Data 2, 1.

O'Neill, B.C., Ren, X., Jiang, L., Dalton, M., 2012. The effect of urbanization on energy use in India and China in the iPETS model. Energy Econ. 34, S339–S345. https://doi.org/10.1016/j.eneco.2012.04.004

Olofsson, P., Foody, G.M., Herold, M., Stehman, S. V, Woodcock, C.E., Wulder, M.A., 2014. Good practices for estimating area and assessing accuracy of land change. Remote Sens. Environ. 148, 42–57. https://doi.org/10.1016/j.rse.2014.02.015

Olofsson, P., Foody, G.M., Stehman, S. V, Woodcock, C.E., 2013. Making better use of accuracy data in land change studies: Estimating accuracy and area and quantifying uncertainty using stratified estimation. Remote Sens. Environ. 129, 122–131. https://doi.org/http://dx.doi.org/10.1016/j.rse.2012.10.031

Orphanides, A., 2003. Monetary policy evaluation with noisy information. J. Monet. Econ. 50, 605–631. https://doi.org/10.1016/S0304-3932(03)00027-8

Pal, M., 2005. Random forest classifier for remote sensing classification. Int. J.

Remote Sens. 26, 217–222. https://doi.org/10.1080/01431160412331269698

Pekel, J.F., Cottam, A., Gorelick, N., Belward, A.S., 2016. High-resolution mapping of global surface water and its long-term changes. Nature 540, 418–422. https://doi.org/10.1038/nature20584

Peng, S., Piao, S., Ciais, P., Friedlingstein, P., Ottle, C., Breon, F.-M., Nan, H., Zhou, L., Myneni, R.B., 2012. Surface Urban Heat Island Across 419 Global Big Cities. Environ. Sci. Technol. 46, 696–703. https://doi.org/10.1021/es2030438

Pickens, A.H., Hansen, M.C., Hancher, M., Stehman, S. V, Tyukavina, A., Potapov, P., Marroquin, B., Sherani, Z., 2020. Mapping and sampling to characterize global inland water dynamics from 1999 to 2018 with full Landsat time-series. Remote Sens. Environ. 243, 111792. https://doi.org/https://doi.org/10.1016/j.rse.2020.111792

Piketty, T., Saez, E., Zucman, G., 2018. Distributional national accounts: Methods and estimates for the United States. Q. J. Econ. https://doi.org/10.1093/qje/qjx043

Potapov, P., Hansen, M.C., Kommareddy, I., Kommareddy, A., Turubanova, S., Pickens, A., Adusei, B., Tyukavina, A., Ying, Q., 2020. Landsat analysis ready data for global land cover and land cover change mapping. Remote Sens. 12, 426. https://doi.org/10.3390/rs12030426

Potapov, P., Turubanova, S., Hansen, M.C., 2011. Regional-scale boreal forest cover and change mapping using Landsat data composites for European Russia. Remote Sens. Environ. 115, 548–561. https://doi.org/10.1016/j.rse.2010.10.001

Potapov, P. V., Turubanova, S.A., Tyukavina, A., Krylov, A.M., McCarty, J.L.,

Radeloff, V.C., Hansen, M.C., 2015. Eastern Europe's forest cover dynamics from 1985 to 2012 quantified from the full Landsat archive. Remote Sens. Environ. 159, 28–43. https://doi.org/10.1016/j.rse.2014.11.027

Potapov, P. V, Turubanova, S.A., Hansen, M.C., Adusei, B., Broich, M., Altstatt, A., Mane, L., Justice, C.O., 2012. Quantifying forest cover loss in Democratic Republic of the Congo, 2000-2010, with Landsat ETM plus data. Remote Sens. Environ. 122, 106–116. https://doi.org/10.1016/j.rse.2011.08.027

Potere, D., 2008. Horizontal positional accuracy of Google Earth's high-resolution imagery archive. Sensors 8, 7973–7981. https://doi.org/10.3390/s8127973

Pu, R., Gong, P., Michishita, R., Sasagawa, T., 2008. Spectral mixture analysis for mapping abundance of urban surface components from the Terra/ASTER data. Remote Sens. Environ. 112, 939–954. https://doi.org/10.1016/j.rse.2007.07.005

Ren, S., He, K., Girshick, R., Sun, J., 2017. Faster R-CNN: Towards Real-Time Object Detection with Region Proposal Networks. IEEE Trans. Pattern Anal. Mach. Intell. 39, 1137–1149. https://doi.org/10.1109/TPAMI.2016.2577031

Ren, S., He, K., Girshick, R., Sun, J., 2015. Faster r-cnn: Towards real-time object detection with region proposal networks, in: Advances in Neural Information Processing Systems. pp. 91–99.

Rogan, J., Franklin, J., Stow, D., Miller, J., Woodcock, C., Roberts, D., 2008. Mapping land-cover modifications over large areas: A comparison of machine learning algorithms. Remote Sens. Environ. 112, 2272–2283. https://doi.org/10.1016/j.rse.2007.10.004

Ronneberger, O., Fischer, P., Brox, T., 2015. U-net: Convolutional networks for

biomedical image segmentation, in: International Conference on Medical Image Computing and Computer-Assisted Intervention. Springer, pp. 234–241.

Roy, D.P., Ju, J., Kline, K., Scaramuzza, P.L., Kovalskyy, V., Hansen, M., Loveland, T.R., Vermote, E., Zhang, C., 2010. Web-enabled Landsat Data (WELD): Landsat ETM+ composited mosaics of the conterminous United States. Remote Sens. Environ. 114, 35–49. https://doi.org/10.1016/j.rse.2009.08.011

Säumel, I., Kowarik, I., 2010. Urban rivers as dispersal corridors for primarily wind-dispersed invasive tree species. Landsc. Urban Plan. 94, 244–249. https://doi.org/https://doi.org/10.1016/j.landurbplan.2009.10.009

Schneider, A., 2012. Monitoring land cover change in urban and pen-urban areas using dense time stacks of Landsat satellite data and a data mining approach. Remote Sens. Environ. 124, 689–704. https://doi.org/10.1016/j.rse.2012.06.006

Schneider, A., Friedl, M.A., Potere, D., 2010. Mapping global urban areas using MODIS 500-m data: New methods and datasets based on ‘urban ecoregions.’ Remote Sens. Environ. 114, 1733–1746. https://doi.org/10.1016/j.rse.2010.03.003

Schneider, A., Friedl, M.A., Potere, D., 2009. A new map of global urban extent from MODIS satellite data. Environ. Res. Lett. 4. https://doi.org/10.1088/1748-9326/4/4/044003

Seinfeld, J.H., 1989. Urban Air Pollution: State of the Science. Science (80-.). 243, 745 LP – 752. https://doi.org/10.1126/science.243.4892.745

Serra, P., Pons, X., Sauri, D., 2003. Post-classification change detection with data from different sensors: some accuracy considerations. Int. J. Remote Sens. 24,

3311–3340.

Seto, K.C., Guneralp, B., Hutyra, L.R., 2012. Global forecasts of urban expansion to 2030 and direct impacts on biodiversity and carbon pools. Proc. Natl. Acad. Sci. 109, 16083–16088. https://doi.org/10.1073/pnas.1211658109

Seto, K.C., Kaufmann, R.K., 2003. Modeling the drivers of urban land use change in the Pearl River Delta, China: Integrating remote sensing with socioeconomic data. Land Econ. 79, 106–121. https://doi.org/10.2307/3147108

Sexton, J.O., Song, X.-P., Huang, C., Channan, S., Baker, M.E., Townshend, J.R., 2013. Urban growth of the Washington, DC-Baltimore, MD metropolitan region from 1984 to 2010 by annual, Landsat-based estimates of impervious cover. Remote Sens. Environ. 129, 42–53. https://doi.org/10.1016/j.rse.2012.10.025

Shao, Y., Lunetta, R.S., 2012. Comparison of support vector machine, neural network, and CART algorithms for the land-cover classification using limited training data points. ISPRS J. Photogramm. Remote Sens. 70, 78–87. https://doi.org/10.1016/j.isprsjprs.2012.04.001

Shiller, R.J., 2008. Historic Turning Points in Real Estate. East. Econ. J. 34, 1–13. https://doi.org/10.1057/palgrave.eej.9050001

Shukla, J., Nobre, C., Sellers, P., 1990. Amazon deforestation and climate change. Science (80-.). 247, 1322–1325. https://doi.org/10.1126/science.247.4948.1322

Simons, H., Soto, X., Zhu, Z., Singh, K.D., Bellan, M.-F., Iremonger, S., Hirvonen, H., Smith, B., Watson, V., Tosi, J., 2001. Global Ecological Zoning for the Global Forest Resources Assessment 2000-Final Report.

Singh, A., 1989. Review Article Digital change detection techniques using remotely-

sensed data. Int. J. Remote Sens. 10, 989–1003. https://doi.org/10.1080/01431168908903939

Sleeter, B.M., Sohl, T.L., Loveland, T.R., Auch, R.F., Acevedo, W., Drummond, M.A., Sayler, K.L., Stehman, S. V., 2013. Land-cover change in the conterminous United States from 1973 to 2000. Glob. Environ. Chang. 23, 733–748. https://doi.org/10.1016/j.gloenvcha.2013.03.006

Small, C., 2005. A global analysis of urban reflectance. Int. J. Remote Sens. 26, 661–681. https://doi.org/10.1080/01431160310001654950

Small, C., Pozzi, F., Elvidge, C.D., 2005. Spatial analysis of global urban extent from DMSP-OLS night lights. Remote Sens. Environ. 96, 277–291. https://doi.org/10.1016/j.rse.2005.02.002

Song, X.-P., Hansen, M.C., Stehman, S. V., Potapov, P. V., Tyukavina, A., Vermote, E.F., Townshend, J.R., 2018. Global land change from 1982 to 2016. Nature 560, 639–643. https://doi.org/10.1038/s41586-018-0411-9

Song, X.-P., Potapov, P. V., Krylov, A., King, L., Di Bella, C.M., Hudson, A., Khan, A., Adusei, B., Stehman, S. V., Hansen, M.C., 2017. National-scale soybean mapping and area estimation in the United States using medium resolution satellite imagery and field survey. Remote Sens. Environ. 190, 383–395. https://doi.org/10.1016/j.rse.2017.01.008

Song, X.-P., Sexton, J.O., Huang, C., Channan, S., Townshend, J.R., 2016. Characterizing the magnitude, timing and duration of urban growth from time series of Landsat-based estimates of impervious cover. Remote Sens. Environ. 175, 1–13. https://doi.org/10.1016/j.rse.2015.12.027

Sonter, L.J., Moran, C.J., Barrett, D.J., Soares-Filho, B.S., 2014. Processes of land use change in mining regions. J. Clean. Prod. 84, 494–501. https://doi.org/10.1016/j.jclepro.2014.03.084

Stehman, S. V., 2013. Estimating area from an accuracy assessment error matrix. Remote Sens. Environ. 132, 202–211. https://doi.org/10.1016/j.rse.2013.01.016

Stehman, S. V., 2009. Sampling designs for accuracy assessment of land cover. Int. J. Remote Sens. 30, 5243–5272. https://doi.org/10.1080/01431160903131000

Stehman, S. V., 2000. Practical implications of design-based sampling inference for thematic map accuracy assessment. Remote Sens. Environ. 72, 35–45. https://doi.org/10.1016/S0034-4257(99)00090-5

Stehman, S. V, 2014. Estimating area and map accuracy for stratified random sampling when the strata are different from the map classes. Int. J. Remote Sens. 35, 4923–4939. https://doi.org/10.1080/01431161.2014.930207

Swenson, J.J., Carter, C.E., Domec, J.-C., Delgado, C.I., 2011. Gold Mining in the Peruvian Amazon: Global Prices, Deforestation, and Mercury Imports. PLoS One 6, e18875. https://doi.org/10.1371/journal.pone.0018875

Tao, C., Tan, Y., Cai, H., Tian, J., 2011. Airport Detection From Large IKONOS Images Using Clustered SIFT Keypoints and Region Information. IEEE Geosci. Remote Sens. Lett. 8, 128–132. https://doi.org/10.1109/LGRS.2010.2051792

The World Bank, n.d. Urban population (% of total) | Data [WWW Document]. URL https://data.worldbank.org/indicator/SP.URB.TOTL.IN.ZS (accessed 1.25.19).

Townshend, J., Justice, C., Li, W., Gurney, C., McManus, J., 1991. Global land cover classification by remote sensing: present capabilities and future possibilities.

Remote Sens. Environ. 35, 243–255. https://doi.org/10.1016/0034-4257(91)90016-Y

Tuia, D., Flamary, R., Courty, N., 2015. Multiclass feature learning for hyperspectral image classification: Sparse and hierarchical solutions. ISPRS J. Photogramm. Remote Sens. 105, 272–285.

Turner B. L., I.I., Lambin, E.F., Reenberg, A., 2007. The emergence of land change science for global environmental change and sustainability. Proc. Natl. Acad. Sci. U. S. A. 104, 20666–20671. https://doi.org/10.1073/pnas.0704119104

Tyukavina, A., Baccini, A., Hansen, M.C., Potapov, P. V, Stehman, S. V, Houghton, R.A., Krylov, A.M., Turubanova, S., Goetz, S.J., 2015. Aboveground carbon loss in natural and managed tropical forests from 2000 to 2012. Environ. Res. Lett. 10, 074002. https://doi.org/10.1088/1748-9326/10/7/074002

Tyukavina, A., Hansen, M.C., Potapov, P., Parker, D., Okpa, C., Stehman, S. V., Kommareddy, I., Turubanova, S., 2018. Congo Basin forest loss dominated by increasing smallholder clearing. Sci. Adv. 4, eaat2993. https://doi.org/10.1126/sciadv.aat2993

Tyukavina, A., Hansen, M.C., Potapov, P. V., Stehman, S. V., Smith-Rodriguez, K., Okpa, C., Aguilar, R., 2017. Types and rates of forest disturbance in Brazilian Legal Amazon, 2000–2013. Sci. Adv. 3.

Tyukavina, A., Stehman, S. V, Potapov, P. V, Turubanova, S.A., Baccini, A., Goetz, S.J., Laporte, N.T., Houghton, R.A., Hansen, M.C., 2013. National-scale estimation of gross forest aboveground carbon loss: a case study of the Democratic Republic of the Congo. Environ. Res. Lett. 8, 1–14.

https://doi.org/10.1088/1748-9326/8/4/044039

U.S. Energy Information Administration (EIA) [WWW Document], n.d. URL https://www.eia.gov/petroleum/wells/ (accessed 8.29.18).

Verburg, P.H., Schot, P.P., Dijst, M.J., Veldkamp, A., 2004. Land use change modelling: current practice and research priorities. GeoJournal 61, 309–324. https://doi.org/10.1007/s10708-004-4946-y

Vitousek, P.M., Mooney, H.A., Lubchenco, J., Melillo, J.M., 1997. Human domination of Earth's ecosystems. Science (80-.). 277, 494–499. https://doi.org/10.1126/science.277.5325.494

Wang, B., Huang, J., Yang, X., Zhang, B., Liu, M., 2010. Estimation of biomass, net primary production and net ecosystem production of China's forests based on the 1999-2003 National Forest Inventory. Scand. J. For. Res. 25. https://doi.org/10.1080/02827581.2010.524891

Wang, L., Duan, W., Yu, B., Ying, Q., Yang, H., Lei, Y., 2019. Exploring the Response Mechanism of Remote Sensing Images in Monitoring Fixed Assets Investment Project in Terms of Building Detection. IEEE Access 7, 167919–167929.

Wang, L., Gong, P., Ying, Q., Yang, Z., Cheng, X., Ran, Q., 2010. Settlement extraction in the North China Plain using Landsat and Beijing-1 multispectral data with an improved watershed segmentation algorithm. Int. J. Remote Sens. 31, 1411–1426. https://doi.org/10.1080/01431160903475332

Wang, L., Li, C., Ying, Q., Cheng, X., Wang, X., Li, X., Hu, L., Liang, L., Yu, L., Huang, H., Gong, P., 2012. China's urban expansion from 1990 to 2010

determined with satellite remote sensing. Chinese Sci. Bull. 57, 2802–2812. https://doi.org/10.1007/s11434-012-5235-7

Wang, P., Huang, C., Brown de Colstoun, E., 2017. Mapping 2000–2010 Impervious Surface Change in India Using Global Land Survey Landsat Data. Remote Sens. 9, 366. https://doi.org/10.3390/rs9040366

Wang, Y., Li, L., Kubota, J., Han, R., Zhu, X., Lu, G., 2016. Does urbanization lead to more carbon emission? Evidence from a panel of BRICS countries. Appl. Energy 168, 375–380. https://doi.org/https://doi.org/10.1016/j.apenergy.2016.01.105

Wang, Z., Schaaf, C.B., Sun, Q., Shuai, Y., Román, M.O., 2018. Capturing rapid land surface dynamics with Collection V006 MODIS BRDF/NBAR/Albedo (MCD43) products. Remote Sens. Environ. 207, 50–64. https://doi.org/10.1016/j.rse.2018.02.001

Weber, K.T., Alados, C.L., Guillermo Bueno, C., Gokhale, B., Komac, B., Pueyo, Y., 2009. Modeling Bare Ground With Classification Trees in Northern Spain. Rangel. Ecol. Manag. 62, 452–459.

Weiss, D.J., Nelson, A., Gibson, H.S., Temperley, W., Peedell, S., Lieber, A., Hancher, M., Poyart, E., Belchior, S., Fullman, N., Mappin, B., Dalrymple, U., Rozier, J., Lucas, T.C.D., Howes, R.E., Tusting, L.S., Kang, S.Y., Cameron, E., Bisanzio, D., Battle, K.E., Bhatt, S., Gething, P.W., 2018. A global map of travel time to cities to assess inequalities in accessibility in 2015. Nature 553, 333–336. https://doi.org/10.1038/nature25181

Williamson, S.D., 2002. Macroeconomics. Pearson.

Woodcock, C.E., Allen, R., Anderson, M., Belward, A., Bindschadler, R., Cohen, W., Gao, F., Goward, S.N., Helder, D., Helmer, E., Nemani, R., Oreopoulos, L., Schott, J., Thenkabail, P.S., Vermote, E.F., Vogelmann, J., Wulder, M.A., Wynne, R., Landsat Sci, T., 2008. Free access to Landsat imagery. Science (80-.). 320, 1011.

Woodcock, C.E., Loveland, T.R., Herold, M., Bauer, M.E., 2019. Transitioning from change detection to monitoring with remote sensing: A paradigm shift. Remote Sens. Environ. 111558. https://doi.org/10.1016/j.rse.2019.111558

World Bank, n.d. World Bank Country and Lending Groups [WWW Document]. URL https://datahelpdesk.worldbank.org/knowledgebase/articles/906519-world-bank-country-and-lending-groups (accessed 10.7.16a).

World Bank, n.d. World Development Indicators-GDP growth [WWW Document]. URL http://data.worldbank.org/indicator/NY.GDP.MKTP.KD.ZG (accessed 10.7.16b).

World Bank Open Data | Data [WWW Document], n.d. URL https://data.worldbank.org/ (accessed 9.10.19).

Wulder, M.A., Loveland, T.R., Roy, D.P., Crawford, C.J., Masek, J.G., Woodcock, C.E., Allen, R.G., Anderson, M.C., Belward, A.S., Cohen, W.B., Dwyer, J., Erb, A., Gao, F., Griffiths, P., Helder, D., Hermosilla, T., Hipple, J.D., Hostert, P., Hughes, M.J., Huntington, J., Johnson, D.M., Kennedy, R., Kilic, A., Li, Z., Lymburner, L., McCorkel, J., Pahlevan, N., Scambos, T.A., Schaaf, C., Schott, J.R., Sheng, Y., Storey, J., Vermote, E., Vogelmann, J., White, J.C., Wynne, R.H., Zhu, Z., 2019. Current status of Landsat program, science, and

applications. Remote Sens. Environ. 225, 127–147. https://doi.org/10.1016/j.rse.2019.02.015

Xian, G., Homer, C., 2010. Updating the 2001 National Land Cover Database Impervious Surface Products to 2006 using Landsat Imagery Change Detection Methods. Remote Sens. Environ. 114, 1676–1686. https://doi.org/10.1016/j.rse.2010.02.018

Xian, G., Homer, C., Dewitz, J., Fry, J., Hossain, N., Wickham, J., 2011. The change of impervious surface area between 2001 and 2006 in the conterminous United States. Photogramm. Eng. Remote Sensing2 77, 759–762.

Xiao, Z., Gong, Y., Long, Y., Li, D., Wang, X., Liu, H., 2017. Airport detection based on a multiscale fusion feature for optical remote sensing images. IEEE Geosci. Remote Sens. Lett. 14, 1469–1473.

Xie, R., Fang, J., Liu, C., 2017. The effects of transportation infrastructure on urban carbon emissions. Appl. Energy 196, 199–207. https://doi.org/https://doi.org/10.1016/j.apenergy.2017.01.020

Xu, Y., Zhu, M., Li, S., Feng, H., Ma, S., Che, J., 2018. End-to-end airport detection in remote sensing images combining cascade region proposal networks and multi-threshold detection networks. Remote Sens. 10, 1516.

Yang, L., Huang, C., Homer, C.G., Wylie, B.K., Coan, M.J., 2003. An approach for mapping large-area impervious surfaces: synergistic use of Landsat-7 ETM+ and high spatial resolution imagery. Can. J. Remote Sens. 29, 230–240. https://doi.org/10.5589/m02-098

Yang, L., Jin, S., Danielson, P., Homer, C., Gass, L., Bender, S.M., Case, A.,

Costello, C., Dewitz, J., Fry, J., Funk, M., Granneman, B., Liknes, G.C., Rigge, M., Xian, G., 2018. A new generation of the United States National Land Cover Database: Requirements, research priorities, design, and implementation strategies. ISPRS J. Photogramm. Remote Sens. 146, 108–123. https://doi.org/10.1016/J.ISPRSJPRS.2018.09.006

Ying, Q., Hansen, M.C., Potapov, P. V., Tyukavina, A., Wang, L., Stehman, S. V., Moore, R., Hancher, M., 2017. Global bare ground gain from 2000 to 2012 using Landsat imagery. Remote Sens. Environ. 194, 161–176. https://doi.org/10.1016/j.rse.2017.03.022

Ying, Q., Hansen, M.C., Sun, L., Wang, L., Steininger, M., 2019. Satellite-detected gain in built-up area as a leading economic indicator. Environ. Res. Lett. 14, 114015.

Yu, Y., Feng, K., Hubacek, K., 2013. Tele-connecting local consumption to global land use. Glob. Environ. Chang. 23, 1178–1186. https://doi.org/10.1016/j.gloenvcha.2013.04.006

Zalles, V., Hansen, M.C., Potapov, P. V, Stehman, S. V, Tyukavina, A., Pickens, A., Song, X.-P., Adusei, B., Okpa, C., Aguilar, R., John, N., Chavez, S., 2019. Near doubling of Brazil's intensive row crop area since 2000. Proc. Natl. Acad. Sci. 116, 428–435. https://doi.org/10.1073/pnas.1810301115

Zha, Y., Gao, J., Ni, S., 2003. Use of normalized difference built-up index in automatically mapping urban areas from TM imagery. Int. J. Remote Sens. 24, 583–594. https://doi.org/10.1080/01431160210144570

Zhan, X., Sohlberg, R.A., Townshend, J.R.G., DiMiceli, C., Carroll, M.L., Eastman,

J.C., Hansen, M.C., DeFries, R.S., 2002. Detection of land cover changes using MODIS 250 m data. Remote Sens. Environ. 83, 336–350. https://doi.org/10.1016/s0034-4257(02)00081-0

Zhang, C., Sargent, I., Pan, X., Li, H., Gardiner, A., Hare, J., Atkinson, P.M., 2019. Joint Deep Learning for land cover and land use classification. Remote Sens. Environ. 221, 173–187. https://doi.org/https://doi.org/10.1016/j.rse.2018.11.014

Zhang, P., Niu, X., Dou, Y., Xia, F., 2017. Airport detection on optical satellite images using deep convolutional neural networks. IEEE Geosci. Remote Sens. Lett. 14, 1183–1187.

Zhang, Q., Seto, K.C., 2011. Mapping urbanization dynamics at regional and global scales using multi-temporal DMSP/OLS nighttime light data. Remote Sens. Environ. 115, 2320–2329. https://doi.org/10.1016/j.rse.2011.04.032

Zhang, Z., Liu, Q., Wang, Y., 2018. Road Extraction by Deep Residual U-Net. IEEE Geosci. Remote Sens. Lett. 15, 749–753. https://doi.org/10.1109/LGRS.2018.2802944

Zhao, L., Oppenheimer, M., Zhu, Q., Baldwin, J.W., Ebi, K.L., Bou-Zeid, E., Guan, K., Liu, X., 2018. Interactions between urban heat islands and heat waves. Environ. Res. Lett. 13, 34003. https://doi.org/10.1088/1748-9326/aa9f73

Zhu, Z., Woodcock, C.E., Rogan, J., Kellndorfer, J., 2012. Assessment of spectral, polarimetric, temporal, and spatial dimensions for urban and peri-urban land cover classification using Landsat and SAR data. Remote Sens. Environ. 117, 72–82. https://doi.org/10.1016/j.rse.2011.07.020